Magnetic and Magneto-Optic Investigations of Thin Films of Oxides

by

Hasan Balghaith Albargi

Thesis

Submitted to the University of Sheffield for the degree of

Doctor of Philosophy

Department of Physics and Astronomy

February 2018

In the Name of Allah, the Most Beneficent, the Most Merciful

To my mother, the dearest *Ayeshah Alalawi*

and to my father, *Balghaith Albargi*

To my grandmother, *Fatimah*

To my wife, *Laila*

and to the endorsement of our life *Ahmad*, *Abdullah* and *Deem*

I dedicate this humble work

PREFACE

This thesis has been submitted to the University of Sheffield as a partial fulfilment for the degree of Doctor of Philosophy. The research undertaken at the Department of Physics and Astronomy during the period from 2012 to 2017, under the supervision of Professor Gillian Gehring and Professor Mark Fox. The work described is the original and represents the result of my own research as well as our research collaborators from different parts of the world.

The $GdMnO_3$ samples were grown in the National University of Science and Technology "MISiS", Moscow, Russia. The ZnMgO samples where grown and structurally studied at the KTH Royal Institute of Technology in Stockholm, Sweden by Professor K. V. Rao and his research group. Samples of Fe-doped In_2O_3 grown at base pressure from FeO, Fe_3O_4, and Fe_2O_3 precursors were deposited by Dr. Feng-Xian Jiang from Shanxi Normal University, Linfen, China. The XRD measurements of these samples were also taken there.

EXAFS measurements were taken by Dr. Steve Heald from Advanced Photon Source, Argonne National Laboratory, Argonne, IL, USA.

All the magnetic, optical and magneto-optical measurements were carried out by myself at the University of Sheffield.

Some parts of this thesis have been already published in a number of scientific journals. I hereby certify that this work has not been submitted to any other university or institution for any degree.

H. B. Albargi
Hicks Building, Sheffield
February 2018

ACKNOWLEDGEMENTS

First and foremost, I would like to express my sincere gratitude to my first supervisor **Professor Gillian Gehring**. It was an honour and a great pleasure to do my PhD under her supervision. Her continuous guidance and support throughout all stages of my study are incredibly invaluable, I truly owe her a great debt. My thanks also to my second supervisor Professor Mark Fox for all his beneficial comments and suggestions.

Thanks to all current and previous members of the Magnetic Oxides Group; Dr. Minju Ying, Dr. Qi Feng, Dr. Xiaoli Li, Dr. Wala Dizayee, Ahmad Saeedi, Fatma Gerriu, Aliaa Zaki, and William Fall for the nice time and support. I am grateful for all help and valuable suggestions from Dr. Harry Blythe. I would also like to exploit this opportunity to thank Dr. Mohammad Alqahtani for his assistance and encouragement.

I would also like to thank the Department of Physics and Astronomy for providing an excellent research environment. My thanks goes to the academic staff, administrative and technical staff for all the support and encouragement that I received during my master and PhD degrees.

I am thankful for all the financial support that I was granted from the government of Saudi Arabia and Najran University represented by the Cultural Bureau in London. Special thanks for Professors Ali Alhajri and Mohammad Alassiri for their support and encouragement.

Finally, I would like to say thank you to all my family and in particular all the members of Alalawi family, for their endless love and encouragement, and for always making me happy. Especially thanks to you, Mum, for your life-long support, in fact, none of this would have been possible without you.

ABSTRACT

This thesis reports different types of oxide materials due to their important role in the field of spintronic applications. These materials include multiferroic oxides, transition metal (TM)-doped oxides and d^0 magnetic materials.

The multiferroic $GdMnO_3$ (GMO) films were found to be highly dependent on strain. The structural, magnetic, optical and magneto-optical properties of epitaxial GMO thin films grown on LSAT, $(LaAlO_3)_{0.3}$ $(Sr_2AlTaO_6)_{0.7}$, (100) and (111) substrates were investigated. At low temperature (5 K), the magnetic data show that the easy direction of the film is in-plane for LSAT (100) and the presented canted moment is significantly smaller than that found in bulk but larger than that found for GMO on $SrTiO_3$ (STO) (100). Magnetic circular dichroism (MCD) spectra were found to exhibit two different features: charge transfer transition between Mn *d* states at ~ 2 eV; and band edge transition from the oxygen *p* band to the *d* states at ~ 3 eV.

Mg-doped ZnO (ZnMgO) thin films were studied optically and magnetically to investigate the effect of deposition time (thickness), oxygen pressure, substrate type and deposition method on the band gap, E_g, and magnetisation of ZnMgO films, and any possible correlation between the band gap and magnetism. The magnetic properties were found to be more thickness dependent; the optical properties were strongly affected by oxygen pressure. Different types of substrates, such as glass, quartz and sapphire, affected the optical and magnetic properties of the ZnMgO films. The films deposited on sapphire were found to give the highest E_g, and enhanced magnetisation saturation, M_s, compared to the films deposited on glass and quartz substrates. The optical and magnetic measurements showed a correlation between the band gap value and the magnetic properties.

The structural, magnetic, optical and magneto-optical properties of Fe-doped In_2O_3 thin films were studied using different techniques: X-ray Diffraction (XRD); Energy Dispersive Spectrometer (EDS); X-ray Absorption Near Edge Structure (XANES); and Extended X-ray Absorption Fine Structure (EXAFS); superconducting Quantum Interference Device (SQUID) magnetometer; absorption spectroscopy; and MCD spectroscopy.

The preparation of Fe-doped In_2O_3 from FeO, Fe_3O_4 and Fe_2O_3 precursors revealed that the properties of such material are oxygen pressure dependent and, most importantly, that the magnetic properties are controllable through target preparation. The existence of defects, such as metallic Fe clusters and FeO secondary phase, was discussed and it was found that such defects have a large effect on the magnetic properties of Fe-doped In_2O_3 thin films.

Mn-doped In_2O_3 films were prepared for comparison with the Fe- doped In_2O_3 films and found to be less sensitive to growth conditions such as oxygen pressure. This has been confirmed by the XANES and EXAFS data, revealing no traces of any secondary phases or other impurities as found in the Fe- doped In_2O_3 films.

PUBLICATIONS

1. Sreekanth K. Mahadeva, Zhi-Yong Quan, J. C. Fan, **Hasan B Albargi**, Gillian A Gehring, Anastasia Riazanova, L. Belova and K. V. Rao. *Room Temperature Ferromagnetism and Band Gap Investigations in Mg Doped ZnO RF/DC Sputtered Films*. Materials Research Society Proceedings, 1494, pp 115-120. doi:10.1557/opl.2013.260, (2013).

2. Sreekanth K. Mahadeva, Zhi-Yong Quan, Jin-Cheng Fan, **Hasan B. Albargi**, Gillian A Gehring, Anastasia V. Riazanova, Lyubov M. Belova and K. V. Rao. *Room Temperature Ferromagnetism and Band Gap Engineering in Mg Doped ZnO RF/DC Sputtered Films*. Materials Research Society Proceedings, 1577, mrss13-1577-xx03-28 doi:10.1557/opl.2013.509, (2013).

3. Zhi-Yong Quan, Xian-Peng Zhang, Wei Liu, **Hasan B. Albargi**, Gillian. A. Gehring and Xiao-Hong Xu, *Structural and magnetotransport properties of ultrathin Co/ZnO and Co/ZnAlO films*, Journal of Applied Physics, vol. 115, p. 233908, (2014).

4. M. S. Alshammari, M. S. Alqahtani, **Hasan B. Albargi**, S. A. Alfihed, Y. A. Alshetwi, A. A. Alghihab, A. M. Alsamrah, N. M. Alshammari, M. A. Aldosari, A. Alyamani, A. M. H. R. Hakimi, S. M. Heald, H. J. Blythe, M. G. Blamire, A. M. Fox and G. A. Gehring, *Magnetic properties of In_2O_3 containing Fe_3O_4 nanoparticles*, Physical Review B **90** (14), 144433 (2014).

5. **Hasan B. Albargi**, M.S. Alqahtani, H.J Blythe, A.M. Fox, N. Andreev, V. Chichkov, and G.A. Gehring, *Magnetic and Magneto-optical properties of films of multiferroic $GdMnO_3$ grown on LSAT (100) and (111)*, Thin Solid Films **645** (Supplement C), 326-333 (2018).

CONFERENCES AND WORKSHOPS

1. IOP postgraduate magnetism techniques workshop, University of York, York, UK (Apr 2012).

2. The 6th Saudi Scientific International Conference, Brunel University, London, UK (Oct 2012), **Poster** "*Controlling study of the influence of target preparation on the quality of Fe-doped In_2O_3 thin films grown by PLD*".

3. Workshop of "Future of research excellence and promising centres in Saudi universities", Najran University, Najran, Saudi Arabia (Jan 2013), **Oral and Poster** "*Study of the magnetic and optical properties of thin films grown by PLD*".

4. Magnetism 2014, The University of Manchester, Manchester, UK (Apr 2014),
   Poster I: "Optical and magnetic properties of $Zn_{1-x}Mg_xO$ thin films grown by PLD"
   Poster II: "Study of the magnetic and optical properties of Fe-doped In_2O_3 thin films grown by PLD".

5. Magnetism 2015, University of Leeds, Leeds, UK (Mar 2015), **Poster** "Magnetic and Magneto-optical properties of films of multiferroic $GdMnO_3$ grown LSAT (100) and (111)".

6. 20th International Conference Magnetism (ICM), Palau de Congressos de Catalunya, Barcelona, Spain (July 2015), **Poster** "Magnetic and Magneto-optical properties of films of multiferroic $GdMnO_3$ grown LSAT (100) and (111)".

CONTENTS

LIST OF FIGURES

LIST OF TABLES

LIST OF ABBREVIATIONS, SYMBOLS AND PHYSICAL CONSTANTS

ABBREVIATIONS

AFM	Atomic force microscopy
AFM	Antiferromagnetic
CAFM	Canted antiferromagnetism
CB	Conduction Band
CVD	Chemical Vapour Deposition
DC	Direct Current
Dektak	Profilometer for thin film thickness measurements
DMS	Dilute magnetic semiconductors
EDS	Energy Dispersive Spectrometer
EXAFS	Extended X-ray Absorption Fine Structure
FE	Ferroelectric transition
FM	Ferromagnetic
FR	Faraday rotation
FIB	Focused Ion Beam
GB	Grain boundaries
GMO	$GdMnO_3$ gadolinium manganite
ICAFM	Incommensurate antiferromagnetism
KTH	Royal Institute of Technology
LAO	$LaAlO_3$ substrate
LSAT	$(LaAlO_3)_{0.3}$ $(Sr_2AlTaO_6)_{0.7}$ substrate
LMIS	Liquid-Metal Ion Source
MBE	Molecular Beam Epitaxy
MCD	Magnetic Circular Dichroism
MISiS	The National University of Science and Technology
MTI	Materials Technology International Corporation
PEM	Photoelastic modulator
PLD	Pulsed Laser Deposition
PM	Paramagnetic

PMT	Photomultiplier tube detector
RE	Rare-earth manganites
RF	Radio Frequency
RKKY	Ruderman-Kittel-Kasuya-Yosida interaction
RT	Room temperature
RTFM	Room temperature ferromagnetism
SEM	Scanning Electron Microscopy
SQUID	Superconducting Quantum Interference Device
STO	$SrTiO_3$ substrate
TM	Transition metals
TMO	Transition metal oxides
XANES	X-ray Absorption Near Edge Structure
XRD	X-ray Diffraction
ZFC/FC	Zero-field-cooled and field-cooled
ZnMgO	Mg-doped ZnO

SYMBOLS

I	Electric current
ω	Angular velocity
r	Radius
$\boldsymbol{\mu}$	Magnetic moment
A	Area
$\boldsymbol{J}$	Total angular momentum
$\boldsymbol{L}$	Orbital angular momentum
$\boldsymbol{S}$	Spin angular momentum
m	Electron mass
g	Landé g-factor
C	Curie constant
$\boldsymbol{B}$	Magnetic induction
$\boldsymbol{H}$	Magnetic field
Hc	Coercive field
Mr	Remanent Magnetisation
Ms	Magnetisation saturation

Oe	Oersted
p_{eff}^2	Effective magnetic moment
P_{O_2}	Oxygen partial pressure
T_C	Curie temperature
T_N	Néel temperature
χ	Magnetic susceptibility
μ	Magnetic permeability
K	Magnetic anisotropy
V	Particle volume
T_B	Blocking temperature
R	Reflection coefficient
T	Transmission coefficient
α	Absorption coefficient
E_g	Band gap

PHYSICAL CONSTANTS

c	Velocity of light in free space (2.998×10^8 m s^{-1})
e	Electronic charge (1.6022×10^{-19} C)
h	Planck's constant (6.63×10^{-34} J s)
$\hbar$	Reduced Planck's constant (1.05×10^{-34} J s)
k_B	Boltzmann constant ($1{\times}38 \times 10^{-23}$ J K^{-1})
N_A	Avogadro's number (6.022×10^{23} mol^{-1})
μ_B	Bohr magneton (9.27×10^{-24} J T^{-1})
Φ_0	Magnetic quantum flux (2.06×10^{-15} T m^{-2})
μ_0	Magnetic permeability of free space ($4\pi \times 10^{-7}$ H m^{-1})

This page intentionally left blank

Chapter 1

INTRODUCTION AND THESIS OVERVIEW

1.1 INTRODUCTION

This thesis explores how various properties of oxide materials, such as structural, magnetic, optical, and magneto-optical, can be affected and controlled via certain parameters when using pulsed laser deposition (PLD) and sputtering techniques. These parameters include: substrate type, oxygen partial pressure, deposition time (thin film thickness), and different precursors of transition metal oxides (TMO) used to make Fe-doped In_2O_3 targets, including FeO, Fe_3O_4, Fe_2O_3 and Mn_2O_3. For this purpose, a set of different materials, such as multiferroics and dilute magnetic semiconductors (DMS) were studied. The materials chosen for these classes of materials were: $GdMnO_3$ (GMO) as an example of multiferroics; TM (Fe and Mn)-doped In_2O_3, as examples of DMS materials; and Mg-doped ZnO (ZnMgO). However, ZnMgO belongs to a specific class of DMS materials known as d^0 magnetic materials because it does not contain any transition metal ions.

The effects of different conditions in determining the magnetic properties of the above mentioned materials are investigated in detail below. This was achieved using different growth techniques and measurements. The growth techniques used to prepare thin films of different materials include direct current (DC) and radio frequency (RF) magnetron sputtering, as well as pulsed laser deposition (PLD).

X-ray Diffraction (XRD), Focused Ion Beam (FIB), Energy Dispersive Spectrometer (EDS), X-ray Absorption Near Edge Structure (XANES) and Extended

X-ray Absorption Fine Structure (EXAFS) measurements were used to investigate structural properties.

A superconducting Quantum Interference Device (SQUID) magnetometer was utilised for studying different magnetic properties such as hysteresis loops, zero-field-cooled and field-cooled (ZCF/FC) measurements.

Optical measurements of transmission and reflection were used to obtain absorption data and thus determine the band gap values of different materials. In addition, magneto-optic studies were performed to investigate the MCD spectra of GMO and TM-doped In_2O_3 samples in order to gain more information about the band structure and electronic states.

Multiferroics are, in general, defined as materials that can exhibit coupling between ferromagnetic, ferroelectric and ferroelastic properties. This means that multiferroic materials can show two or three of the ferroic properties in the same phase. For instance, electric polarisation and a magnetic long-range order can simultaneously exist and, therefore, each one can affect the other [1-6].

The correlation between the magnetism and ferroelectricity of multiferroic materials makes them promising candidates for multifunctional applications. Hence, multiferroics have attracted a great deal of scientific interest due to their extraordinary physical properties [6, 7].

Studying multiferroics is, by no means, an emerging field as they were studied to some extent in the 1960s and 1970s; then, interest declined because of the difficulty in producing single-phase materials with ferromagnetic and ferroelectric ordering. Nonetheless, interest has been re-stimulated in the multiferroics by virtue of well-developed deposition techniques that produce high quality thin films, making possible the modification of the properties of such materials through strain engineering. This

improvement has also raised the possibility of multiferroics as candidates for spintronic applications, where both the electronic spin and the electronic charge are exploited for processing data and information storage. Spintronic devices have several attractive advantages over the conventional charge-based electronics, such as smaller size, high data-processing speed, and lower power consumption [4, 8].

Multiferroic materials are very sensitive to strain. This effect can be induced by distorting the lattice of a multiferroic thin film when grown epitaxially on a substrate. This occurs due to the lattice mismatch that exists between the thin film and the substrate. The magnetisation of multiferroic materials has been found to be strain-related [9-13]. Thus, the magnetisation of GMO was studied as a function of strain produced by growing epitaxial GMO thin films on two different substrates of LSAT, $(LaAlO_3)_{0.3}$ $(Sr_2AlTaO_6)_{0.7}$, these are (100) and (111) [1, 2, 14, 15].

For d^0 magnetic materials, ZnMgO was studied as an example. The interest in studying such materials has arisen as they show ferromagnetic behaviour with a Curie temperature (T_C) at or above room temperature [8]. From a theoretical point of view, increasing the band gap proportionally affects the magnetisation of the ZnMgO [16]. Accordingly, MgO was included as a dopant in the ZnO matrix, because of its wide band gap of ~ 7.8 eV, to investigate how such doping can influence the magnetic and optical properties of ZnMgO thin films [17-20].

The effects of film thickness and oxygen pressure on the magnetisation as well as the band gap of ZnMgO thin films grown on silicon, glass, quartz and sapphire substrates were studied. The highest magnetisation was obtained for the ZnMgO with thinnest film thickness of ~ 55 nm grown on sapphire at low oxygen pressure [19, 20].

TM-doped In_2O_3 is an example of DMS materials which is a transparent material with a wide band gap of ~ 3.7 eV. In such a material, a small fraction of the

TM magnetic ions, typically less than 10%, are incorporated in the host material, substituting its cations. TM materials have partially filled *d* states which, in turn, enhance the magnetic properties of the host oxide material [21-24].

The study of (TM)-doped In_2O_3 was undertaken for two different purposes. The first was to find out how it is possible to control the magnetic properties via the preparation of the target used for the growth of thin films. For this purpose, three different precursors of FeO, Fe_3O_4 and Fe_2O_3 were used for doping In_2O_3 with 5% of Fe [23-25]. The second purpose was to examine the sensitivity of doping In_2O_3 with different TM dopants. Thus, the In_2O_3 was doped with Mn because Fe-doped In_2O_3 films showed a considerable fraction of Fe metallic clusters which obviously affects the magnetisation when deposited under a base pressure of 5×10^{-5} Torr.

On the other hand, Mn was found to give less disordered structures where all Mn ions are substitutional to In ions in the In_2O_3 matrix; meaning that the Mn-doped In_2O_3 films exclude any formation of Mn defects. This is evidence that In_2O_3 is more sensitive to Fe-doping than when doped with Mn under the same growth conditions [25, 26].

1.2 THESIS OVERVIEW

This thesis consists of seven chapters: **Chapter One** provides a general introduction to the thesis and its structure. Brief definitions and information about the materials studied are also given. This chapter also mentions the deposition methods of sputtering and PLD that were used to grow GMO, ZnMgO, and TM-doped In_2O_3 thin films.

In addition, the investigation of structural, magnetic, optical, and magneto-optical properties of the materials studied using the experimental techniques of XRD,

FIB, EDS XANES, EXAFS, SQUID, optical spectroscopy, and magneto-optic spectroscopy are also mentioned. Manipulation of a number of growth conditions, such as substrate type, film thickness, oxygen pressure, TM precursor and their effects on the properties of the materials of interest are introduced.

Thus, this chapter should give the reader an idea about the area of research, why these materials were chosen, and the possibility of any future applications.

Chapter Two introduces the background to magnetism required to understand the work and the results obtained. Each part of these fundamentals is explained to give a fairly complete picture of the behaviour of magnetic materials.

The first part will introduce the idea of electron movement around the nucleus (the orbital motion) and its spin. A number of properties will then be mentioned, such as the orbital and spin magnetic moment, orbital and spin angular momenta, quantum numbers and the *g*-factor. Then, the Pauli exclusion principle and Hund's rules are presented and discussed.

Different magnetic materials, including diamagnetic, paramagnetic, ferromagnetic, antiferromagnetic and ferrimagnetic, are defined and explained. The related magnetic properties and the role they play in classifying these materials are also introduced. These properties include magnetic susceptibility, the Curie temperature and the Néel temperature (T_N).

Exchange interactions such as direct and indirect interactions including super-exchange, double exchange and Ruderman-Kittel-Kasuya-Yosida (RKKY) interaction are explained. Covering such topics will assist in understanding the different behaviours of magnetic oxides.

Chapter Three describes the experimental methods and techniques used to carry out the practical procedures and make different measurements: the fabrication of

TM-doped In_2O_3 target using the solid state reaction method; the deposition of TM-doped In_2O_3 thin films using the PLD technique; the measurement of thin film thickness using a Dektak surface profiler; SQUID magnetometer; XRD, FIB, EDS, XANES, and EXAFS; and optical and magneto-optical measurements.

Chapter Four describes the motivation behind the work on multiferroic manganite GMO thin films deposited on LSAT (100) and (111) substrates. The effect of the strain introduced by these substrates on the structural, magnetic, optical and magneto-optical properties is shown and discussed. The obtained data are discussed and compared to previous work done on GMO bulk and GMO thin films deposited on $SrTiO_3$ (STO) (100) substrates.

Chapter Five introduces the aim of the work on ZnMgO thin films deposited by sputtering and PLD techniques. This chapter displays experimental results on the structural, optical and magnetic properties of ZnMgO and the influence of different parameters on these properties. The parameters that were varied in this section were film thickness, oxygen pressure and substrate type. All these growth conditions were varied using two deposition techniques: sputtering and PLD.

The effects of each parameter on various properties are studied separately and the resultant data are compared to the previous work on ZnMgO thin films in order to determine which parameter was most effective on which property. For example, the band gap was found to be more affected by oxygen pressure, while the thickness was found to strongly enhance the magnetisation of ZnMgO thin films.

Chapter Six contains two main sections: Fe-doped In_2O_3 and Mn-doped In_2O_3. The influence of different precursors as sources of Fe to introduce different oxygen contents to the Fe-doped In_2O_3 system is studied. For this purpose, the films were deposited at a base pressure of 5×10^{-5} Torr.

In addition, two different oxygen pressures of 5×10^{-4}, and 5×10^{-3} Torr were introduced to the Fe-doped In_2O_3 during growth to compare the effect of this parameter with that of different oxygen contents contained in different targets.

In_2O_3 was doped with Mn_2O_3 precursor to prepare Mn-doped In_2O_3 thin films. Similarly, the Mn-doped In_2O_3 films were deposited as a function of oxygen pressure at three different oxygen pressures.

The structural, magnetic, optical and magneto-optical properties of Fe-doped In_2O_3 thin films are discussed first, then followed by the discussion of these properties of Mn-doped In_2O_3.

Chapter Seven has two parts; the first part concludes and summarises all the experimental results obtained and discussed in the chapters **Four**, **Five** and **Six**. The aim of this is to identify links between the results obtained in these chapters.

The second part of the chapter provides a plan for proposed future studies. These are mainly based on the work of TM-doped In_2O_3 thin films undertaken at the University of Sheffield and on the facilities provided in Saudi Arabia at Najran University, where the author works.

1.3 REFERENCES

1. M. S. Al Qahtani, M. S. Alshammari, H. J. Blythe, A. M. Fox, G. A. Gehring, N. Andreev, V. Chichkov and Y. Mukovskii, International Conference on Strongly Correlated Electron Systems (Sces 2011) **391**, 012083 (2012).
2. N. Andreev, V. Chichkov, T. Sviridova, N. Tabachkova, A. Volodin, C. Van Haesendonck and Y. Mukovskii, EPJ Web of Conferences **40**, 15014 (2013).
3. N. S. Fedorova, C. Ederer, N. A. Spaldin and A. Scaramucci, Physical Review B **91** (16) (2015).
4. M. Bibes and A. Barthelemy, IEEE Transactions on Electron Devices **54** (5), 1003-1023 (2007).
5. Y. Romaguera-Barcelay, J. Agostinho Moreira, A. Almeida, P. B. Tavares and J. Perez de la Cruz, Thin Solid Films **564**, 419-425 (2014).
6. H. Schmid, Ferroelectrics **162**, 317-338 (1994).
7. H. Béa, M. Gajek, M. Bibes and A. Barthélémy, Journal of Physics: Condensed Matter **20** (43), 434221 (2008).
8. J. M. D. Coey, Solid State Sciences **7** (6), 660-667 (2005).
9. N. Hur, S. Park, P. A. Sharma, J. S. Ahn, S. Guha and S. W. Cheong, Nature **429** (6990), 392-395 (2004).
10. M. W. Kim, S. J. Moon, J. H. Jung, J. Yu, S. Parashar, P. Murugavel, J. H. Lee and T. W. Noh, Phys. Rev. Lett. **96** (24), 247205 (2006).
11. T. Kimura, Annual Review of Materials Research **37** (1), 387-413 (2007).
12. T. Kimura, S. Ishihara, H. Shintani, T. Arima, K. T. Takahashi, K. Ishizaka and Y. Tokura, Physical Review B **68** (6), 060403 (2003).
13. X. Li, C. Lu, J. Dai, S. Dong, Y. Chen, N. Hu, G. Wu, M. Liu, Z. Yan and J.-M. Liu, Scientific Reports **4**, 7019 (2014).

14. R. Choithrani, M. N. Rao, S. L. Chaplot, N. K. Gaur and R. K. Singh, New Journal of Physics**. 11**, 073041 (2009).

15. M. W. Kim, P. Murugavel, P. Sachin, J. S. Lee and T. W. Noh, New Journal of Physics **6** (1), 156 (2004).

16. W. Zhou, H. Deng, H. Cao, J. He, J. Liu, P. Yang and J. Chu, Materials Letters **144**, 93-96 (2015).

17. J. D. Hwang, J. S. Lin and S. B. Hwang, Journal of Physics D: Applied Physics **48** (40), 405103 (2015).

18. S. K. Mahadeva, J. Fan, A. Biswas, K. S. Sreelatha, L. Belova and K. V. Rao, Nanomaterials **3** (3), 486-497 (2013).

19. S. K. Mahadeva, Z.-Y. Quan, J. C. Fan, H. B. Albargi, G. A. Gehring, A. Riazanova, L. Belova and K. V. Rao, MRS Online Proceedings Library Archive **1494**, 115-120 (2013).

20. S. K. Mahadeva, Z.-Y. Quan, J.-C. Fan, H. B. Albargi, G. A. Gehring, A. V. Riazanova, L. M. Belova and K. V. Rao, MRS Online Proceedings Library Archive **1577**, 1-6 (2013).

21. F.-X. Jiang, X.-H. Xu, J. Zhang, X.-C. Fan, H.-S. Wu, M. Alshammari, Q. Feng, H. J. Blythe, D. S. Score, K. Addison, M. Al-Qahtani and G. A. Gehring, Journal of Applied Physics **109** (5), 053907 (2011).

22. S. Kaleemulla, A. S. Reddy, S. Uthanna and P. S. Reddy, Journal of Alloys and Compounds **479** (1–2), 589-593 (2009).

23. M. Ying, H. J. Blythe, W. Dizayee, S. M. Heald, F. M. Gerriu, A. M. Fox and G. A. Gehring, Applied Physics Letters **109** (7), 072403 (2016).

24. M. J. Ying, W. Dizayee, Z. X. Mei, X. L. Du, A. M. Fox and G. A. Gehring, Journal of Physics D-Applied Physics **48** (25) (2015).

25 F.-X. Jiang, X.-H. Xu, J. Zhang, H.-S. Wu, G.A. Gehring, Appl. Surf. Sci. **255**, 3655 (2009).

26. Q. Feng, H. J. Blythe, F.-X. Jiang, X.-H. Xu, S. M. Heald, A. M. Fox and G. A. Gehring, APL Mater. **1** (2), 022107 (2013).

Chapter 2

THEORETICAL BACKGROUND OF MAGNETISM

2.1 INTRODUCTION

This chapter covers magnetic principles and different possible exchange interactions, direct and indirect; the latter include super-exchange interactions, double exchange interaction and Ruderman-Kittel-Kasuya-Yosida interaction. These will assist in understanding and investigating the magnetic behaviour of the materials studied in this thesis. The following introduction to the principles of magnetism, magnetic materials, and exchange interactions has been derived from various text books: *Magnetism and Magnetic Materials* by J. M. D. Coey [1]; *The Magnetic Properties of Solids* by J.R Crangle [2]; *Magnetic Materials Fundamentals and Device Applications* by N. A. Spaldin [3]; *Introduction to Magnetic Materials* by B. D. Cullity [4]; and *Introduction to Solid State Physics* by C. Kittel [5].

2.2 PRINCIPLES OF MAGNETISM

In the classical model of the atom, an electron of charge – *e* and mass *m* rotates in a circular orbit of radius, ***r***, at angular velocity, ω. This situation is equivalent to an electric current $I = \frac{-e\omega}{2\pi}$. Accordingly, due to such a current loop, a magnetic moment $\boldsymbol{\mu}$ is associated with the atom given by:

$$\boldsymbol{\mu} = \mathrm{I}\boldsymbol{A} = -\frac{1}{2}e\boldsymbol{r}\times\boldsymbol{v} = \frac{-e\omega}{2\pi}(\pi r^2) = -\frac{1}{2}e\omega r^2\hat{n} \qquad (2.1).$$

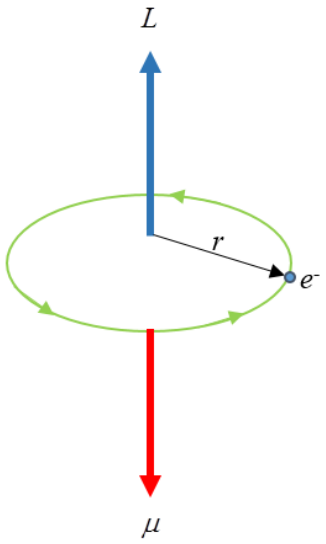

Figure 2.1: The electron of charge *e* moves in a circular orbit where the magnetic moment $\boldsymbol{\mu}$ and the angular momentum $\boldsymbol{L}$ are opposed.

The orbital angular momentum $\boldsymbol{L}$ of the electron is directed in an antiparallel direction to the magnetic moment as shown in Figure 2.1. Since the orbital angular momentum of an electron is given by:

$$|\boldsymbol{L}| = m|\boldsymbol{r} \times \boldsymbol{v}| = m\omega r^2 \qquad (2.2).$$

then the relationship between the magnetic moment and the angular momentum is given by:

$$\boldsymbol{\mu} = \frac{-e}{2m}\boldsymbol{L} \qquad (2.3).$$

According to quantum mechanics, the orbital angular momentum is a quantised quantity in units of $\hbar$ ($h/2\pi$) where h is Planck's constant. The orbital angular momentum of the electron in the ground state must equal $\hbar$, thus the lowest non-zero value of the magnetic moment is:

$$\mu_B = \frac{e\hbar}{2m} = 9.27\times10^{-24}\ \mathrm{J\ T^{-1}} \qquad (2.4).$$

where μ_B is the Bohr magneton, and is the natural unit for expressing atomic magnetic moments.

The orbital magnetic moment is also quantised and can be rewritten in terms of the Bohr magneton as follows:

$$\boldsymbol{\mu} = -g_l \mu_B \boldsymbol{L} \tag{2.5}$$

where $\hbar\boldsymbol{L}$ is the angular momentum vector of the orbiting electron and g_l is the orbital *g*-factor ($g_l \equiv 1$).

The direction of the orbital magnetic moment can be specified by applying an external magnetic field along the *z* direction. Accordingly, the *z* component of the magnetic moment along the direction of the applied magnetic field is given by:

$$\mu_{l_z} = -\mu_B m_l \tag{2.6}$$

where m_l is the component of $\boldsymbol{l}$ along the *z* axis. The values of the magnetic orbital quantum number are given by $m_l = -l, -l+1, \ldots, 0, \ldots, l-1, l$.

In addition, the electron has an intrinsic angular momentum which is called spin; this is responsible for the spin magnetic moment μ_s. By analogy to the orbital motion, the relationship between the spin magnetic moment and the spin angular momentum can be expressed as follows:

$$\boldsymbol{\mu}_s = -g_s \mu_B \boldsymbol{S} \tag{2.7}$$

and the *z* component of the magnetic moment is given by:

$$\mu_{s_z} = -g_s \mu_B m_s \tag{2.8}$$

where g_s is the spin *g*-factor of the electron. It is experimentally found to be approximately twice the value of the orbital *g* factor ($g_s \approx 2$). The spin can have only two orientations, characterised by the spin magnetic quantum number, m_s, that takes the values $-\frac{1}{2}$ and $+\frac{1}{2}$, representing the spin-down and spin-up states, respectively.

Accordingly, the component of the spin magnetic moment for a single electron spin will be $\pm \mu_B$.

As in the orbital case, the direction of the spin magnetic moment is antiparallel to the direction of the spin angular momentum. However, the analogy between the spin motion and the orbital motion must not be taken literally since the spin is a non-classical quantity. This is because the spin quantum number has a fixed value of $\frac{1}{2}$.

In a many-electron atom, except for the heavy elements, the spin magnetic moments form a resultant vector, ***S***, and the orbital magnetic moments form a resultant vector, ***L***, which are given by:

$$\boldsymbol{S} = \sum_i \boldsymbol{s}_i \text{ and } \boldsymbol{L} = \sum_i \boldsymbol{l}_i \tag{2.9}$$

There are two ways in which a total angular momentum, ***J***, can be defined. The most common coupling scheme in which total spin and orbital angular momenta are combined into the total angular momentum is as follows:

$$\boldsymbol{J} = \boldsymbol{L} + \boldsymbol{S} \tag{2.10}$$

This is known as spin-orbit ($L - S$) or Russell-Saunders coupling in which the spin magnetic moment interacts with the magnetic field produced by the orbital motion.

This type of interaction exists in isolated atoms of transition metals and rare-earths since they have incomplete 3*d* and 4*f* shells, respectively. This interaction is considered if the spin-orbit interactions between the spin and orbital angular momenta of individual electrons are small, compared to the interactions of the orbital or spin angular momenta of different electrons.

The magnitude of the total angular momentum is determined by:

$$|J| = \sqrt{J(J+1)}\,\hbar \tag{2.11}$$

where J is the total angular momentum quantum number which takes the values $|L – S|, |L – S + 1|, \ldots, 0, \ldots, |L + S – 1|, |L + S|$.

The total magnetic moment of the atom can be obtained from the following expression:

$$\boldsymbol{\mu}_J = -g_J \mu_B \sqrt{J(J+1)} \tag{2.12}$$

where g_J is the Landé g-factor given by:

$$g_J = 1 + \frac{J(J+1) + S(S+1) - L(L+1)}{2J(J+1)} \tag{2.13}.$$

This factor has the value 2 when $L = 0$, so $J = S$ and an example of this is found in the case of Gd ion.

The component of the total magnetic moment in the direction of the applied field magnetic field (z-axis) is given by:

$$\mu_{J_z} = -g_J \mu_B M_J \tag{2.14}$$

where M_J is the total magnetic quantum number and takes the following values:

$–J, – J + 1, \ldots, 0, ..., J – 1, J$.

In the case of the heavy atoms, the interaction between spin and orbital angular momenta of individual electrons is greater than that of the spin and orbital angular momenta of different electrons. Thus, the spin and orbital angular momenta of each electron couple to give the total angular momentum ($\boldsymbol{j}_i = \boldsymbol{l}_i + \boldsymbol{s}_i$), this is the other coupling scheme that is called JJ coupling which is given by:

$$\boldsymbol{J} = \sum_i \boldsymbol{j}_i \tag{2.15}.$$

However, this case is not-relevant to the materials discussed in this thesis.

2.3 THE PAULI EXCLUSION PRINCIPLE AND HUND'S RULES

In an atom, the energy state of a single electron can be described by the four quantum numbers; n, l, m_l and m_s. According to the Pauli exclusion principle, no two electrons can simultaneously occupy the same energy state. In other words, when two electrons occupy the same electronic state, they must be of opposite spin. This is important when considering the exchange interactions between atoms and the overlap of electron orbitals.

It is also important to consider Hund's rules since they govern all the values of L, S and J of the ground state for a multi-electron atom; these rules state that:

1. Orbitals of the same energy are occupied first with unpaired electrons, making as many spins parallel as possible. As a result of the anti-symmetry of fermion wave functions, the average distance between the unpaired electrons will be large; hence, the electron-electron repulsion energy is minimised. This gives the lowest energy state (the most stable) resulting in S having the maximum value allowed by the Pauli exclusion principle.
2. When the first rule has been satisfied, several values of L are possible. The maximum value of L consistent with the value of S gives the lowest energy state. This can be understood by considering the classical picture of orbiting electrons. When the electrons are orbiting in the same direction, the electron-electron repulsive energy is minimised, therefore the value of L is maximised.
3. $J = |L - S|$ if the shell is less than half-full, and $J = L+S$ if the shell is more than half-full. For a half-filled shell $L = 0$ and $J = S$ (i.e. the atom is said to be in an S-state), and the spin-orbit coupling is inoperative.

For example, in Fe^{2+} ions, representing a 3*d* orbital with six electrons, the available m_l levels will therefore be 2, 1, 0, – 1 and -2. Each of these five levels is occupied with one electron to make as many spins parallel as possible and the sixth electron occupies the level $m_l = 2$ with antiparallel spin. This gives the total spin angular momentum of $S = 4 \times 1/2 = 2$. Since $L = \sum m_l$, we have $L = 2+1+0-1-2+2 = 2$. This results in $J = L + S = 4$. Using the spectroscopic notation ${}^{2S+1}L_J$, the ground state is given by ${}^5D_4$ for the Fe^{2+} ion.

When atoms are brought together to form a solid, only a few materials in the periodic table are magnetic. In non-magnetic materials, the electron spins of the atoms cancel each other and the net magnetic moment of the whole system becomes zero. Other materials, such as 3*d* transition metals and 4*f* rare earths, are magnetic in their metal state as they have a partially-filled orbital and, therefore, a net magnetic moment. The net magnetic moment forming the magnetism of the materials mainly results from spin and orbital moments arising from the net magnetic moment of the unbalanced electron spins in the partially-filled orbital.

In a solid, unlike isolated atoms, the orbital moment might not contribute to the total angular moment; this is known as orbital angular momentum quenching, accordingly $J = S$. This is generated from the effect applied on each atom by the 'crystal field' arising from other surrounding atoms in the solid. This field forces the orbits to be strongly bound or coupled to the crystal lattice. Consequently, when an external magnetic field is applied, the strong orbit-lattice coupling prevents the orbits, and therefore their orbital magnetic moments from turning in the magnetic field direction, whereas the spin can freely turn due to weak spin-orbit coupling.

In many transition metals, for instance, the surrounding anions quench the orbital angular momentum and only the spin magnetic moment needs to be taken into account; meaning that $J = S$.

2.4 MAGNETIC MATERIALS

The magnetic state of a material is described by its magnetisation, $\boldsymbol{M}$, which is defined as the magnetic moment per unit volume of the material. Magnetisation is proportional to the magnetic field, $\boldsymbol{H}$, where the proportionality constant represents the magnetic susceptibility, χ. This magnetic quantity is defined as the tendency of a material to become magnetised when placed in a magnetic field and is given by:

$$\chi = \lim_{H \to 0} \frac{\boldsymbol{M}}{\boldsymbol{H}} \tag{2.16}$$

Magnetic susceptibility is a dimensionless quantity in the SI unit system. In the cgs unit system, however, magnetic susceptibility has a unit of emu per centimetre cubed per Oersted (emu cm^{-3} Oe^{-1}).

In general, magnetic materials can be classified by the sign and magnitude of their magnetic susceptibilities, where the values can be either negative, zero or positive. The magnetic susceptibility of many paramagnets, in addition to ferromagnets and antiferromagnets, is temperature dependent; whereas it is independent of temperature for all diamagnets. More details on the magnetic susceptibility will be given when discussing different types of magnetic materials (see **sections 2.4.1** to **2.4.5**).

Equation (2.16) shows that the magnetisation depends linearly on the magnetic field and becomes zero when the field is removed. This is the case for many solids since they are paramagnetic. However, some materials show a non-zero magnetisation in a zero magnetic field; these are the ferromagnets. In other words, ferromagnetic materials

show a hysteresis loop when zero magnetic field is reached after applying a strong magnetic field. This property of ferromagnets disappears at a characteristic temperature, which is known as the Curie temperature above which the ferromagnetic material becomes paramagnetic.

In addition, when a magnetic material is placed in a magnetic field, two types of magnetic inductions arise: one due to the magnetic field, and the other as a result of the magnetisation of the material. Thus, the produced magnetic induction, $\boldsymbol{B}$, inside the material is given by:

$$\boldsymbol{B} = \mu_0(\boldsymbol{H} + \boldsymbol{M}) \tag{2.17}$$

where μ_0 is the permeability of free space.

Provided that $\boldsymbol{M} = \chi\boldsymbol{H}$, (i.e. not for the ferromagnets), using equation (2.16) in (2.17), the magnetic induction is then given by:

$$\boldsymbol{B} = \mu_0(1+\chi)\boldsymbol{H} \tag{2.18}$$

or

$$\boldsymbol{B} = \mu_0 \mu_r \boldsymbol{H} \tag{2.19}$$

where $\mu_r = 1 + \chi$ is the relative permeability of the material.

2.4.1 Diamagnetism

Atoms in diamagnetic materials have no permanent magnetic moment; the outermost shell in such materials is completely filled with paired electrons. This idea can be better understood by considering two electrons with the same magnitude of magnetic moment and orbiting in opposite directions; this situation results in the two magnetic moments cancelling each other, then the magnetic moment of the atom is zero.

However, applying an external magnetic field to a diamagnetic material produces a magnetic moment that is weak and in the opposite direction to the direction of the externally applied magnetic field. Therefore, diamagnetic materials exhibit a small and negative susceptibility ($\chi < 0$). This means that the magnetic field is weakly repelled by the diamagnetic materials which do not retain magnetic properties when the external field is removed.

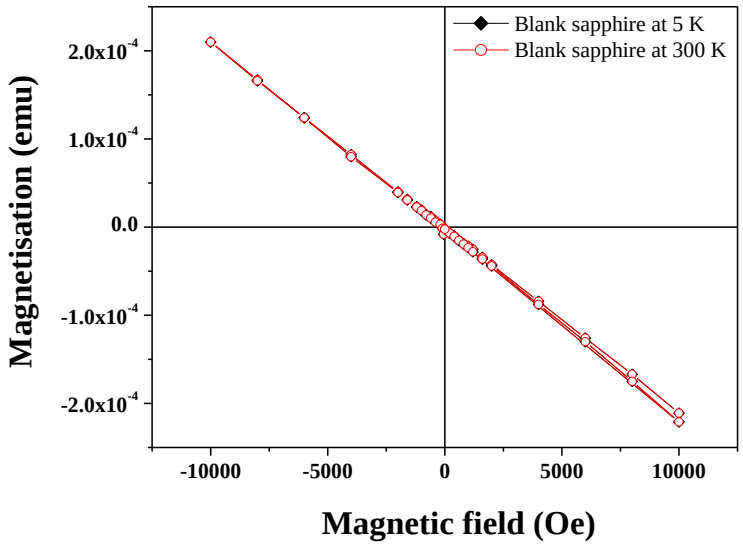

Figure 2.2: The variation of the magnetisation of a blank sapphire substrate with the magnetic field measured at 5 and 300 K.

As noted above, diamagnetic behaviour is independent of temperature. This was found experimentally in the case of a blank sapphire substrate, where there is no difference in the negative values of the magnetic susceptibilities measured at 5 K or 300 K, as illustrated in Figure 2.2.

2.4.2 Paramagnetism

Paramagnetic materials have a small positive susceptibility ($\chi > 0$). The paramagnetic behaviour is attributed to the existence of atoms or ions that have permanent magnetic moments; this behaviour is due to unpaired electrons in the

partially-filled orbitals. Such magnetic moments have random orientations when there is no external magnetic field applied to the material, resulting in zero magnetic moment.

However, in the presence of an external magnetic field, all the unpaired electrons are influenced and tend to align themselves in the direction of the applied external magnetic field. In addition, increasing temperature affects the magnetic moments, causing them to randomise; resulting in decreasing the magnetisation of the paramagnetic material.

It is found experimentally that the magnetisation is proportional to the applied magnetic field, whilst it is inversely proportional to the absolute temperature; this is known as the Curie law which is given by:

$$\boldsymbol{M} = \lim_{H \to 0} \frac{C\boldsymbol{H}}{\boldsymbol{T}} \tag{2.20}$$

where, C is the Curie constant. The above equation can be rewritten in terms of magnetic susceptibility as follows:

$$\chi = \frac{C}{T} \tag{2.21}.$$

The Curie constant is found to be:

$$C = \frac{N\mu_B^2 p_{eff}^2 \mu_0}{3k_B} \tag{2.22}$$

where N is the total number of atoms per unit volume V, k_B is Boltzmann's constant, and p_{eff} is the effective magnetic moment (a useful quantity to compare the magnetic properties of different materials), and is theoretically given by:

$$p_{eff}^2 = g^2 J(J+1) \tag{2.23}.$$

Since not all paramagnetic materials obey the Curie law, it is modified to a more general form known as the Curie-Weiss law:

$$\chi = \frac{C}{T - \theta} \tag{2.24}$$

where θ is called the Curie-Weiss constant or paramagnetic Curie temperature. The modification arises because most magnetic materials have interacting magnetic moments.

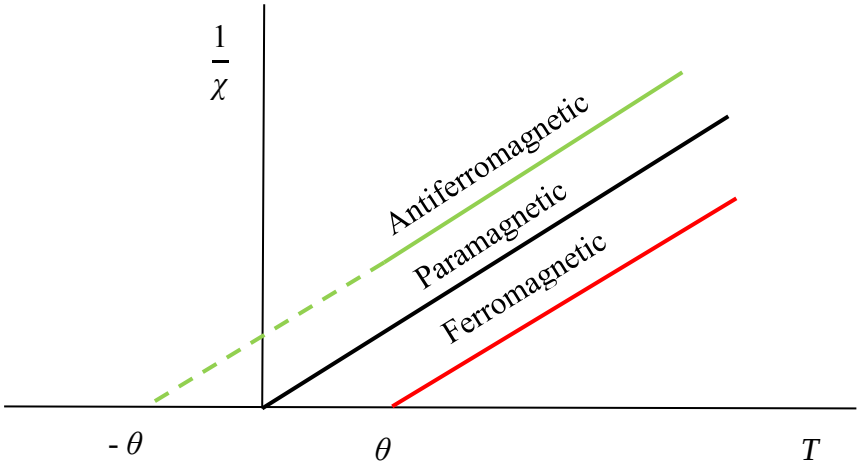

Figure 2.3: The inverse susceptibility as a function of temperature. $\theta = 0$ for a paramagnetic material, $\theta > 0$ for a ferromagnetic material, and $\theta < 0$ for an antiferromagnetic material.

To obtain θ, the inverse susceptibility is plotted as a function of temperature. For a material obeying the Curie-Weiss law, the inverse susceptibility varies linearly with temperature and the intercept on the temperature *x*-axis gives θ.

Values of θ can be either zero, positive, or negative, as shown in Figure 2.3. When $\theta = 0$, then the material is paramagnetic and the equation (2.24) is the expression of Curie's law. A positive value for θ indicates that a material undergoes a paramagnetic to ferromagnetic transition. A negative value for θ indicates that a material undergoes a transition from a paramagnetic to an antiferromagnetic state. Ferromagnetism and antiferromagnetism will be introduced in more detail in the following two sections.

2.4.3 Ferromagnetism

As with paramagnetic materials, ferromagnetic materials also have a positive susceptibility at high temperature. An important property of ferromagnets is that below the Curie temperature they show a spontaneous magnetisation ($\boldsymbol{M} \neq 0$) in the absence of an external magnetic field ($\boldsymbol{H} = 0$).

However, this is quite unlike the behaviour of paramagnetic materials discussed in the previous section, where the ferromagnetism is attributed to the existence of interactions between neighbouring magnetic moments. These interactions are strong enough to yield a cooperative alignment of magnetic moments, creating an internal 'molecular field'. This results in the presence of magnetisation even in the absence of an external magnetic field.

Above the Curie temperature, however, the thermal energy destroys the alignment of the magnetic moments of the ferromagnetic material and behaves as a paramagnet, see Figure 2.4.

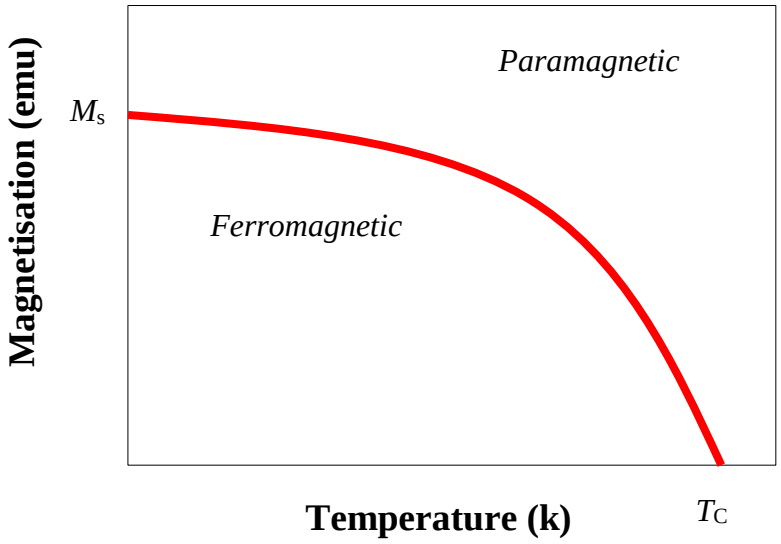

Figure 2.4: Magnetisation versus temperature of a ferro/paramagnetic material.

The values of T_C and θ for a ferromagnetic material are positive and usually close to each other. It should be noted that T_C (the actual transition temperature) is usually slightly higher than θ, in practice, by as much as 20 K. Thus, the gradual transition from ferromagnetic to paramagnetic state is ascribed to the persistence of the internal field due to the short-range magnetic order above T_C.

The magnetisation of a ferromagnetic material below T_C is dependent on its history, thus it exhibits a well-known curve known as the hysteresis loop. Figure 2.5 shows an example of the hysteresis loop of a 5% Fe-doped In_2O_3 sample.

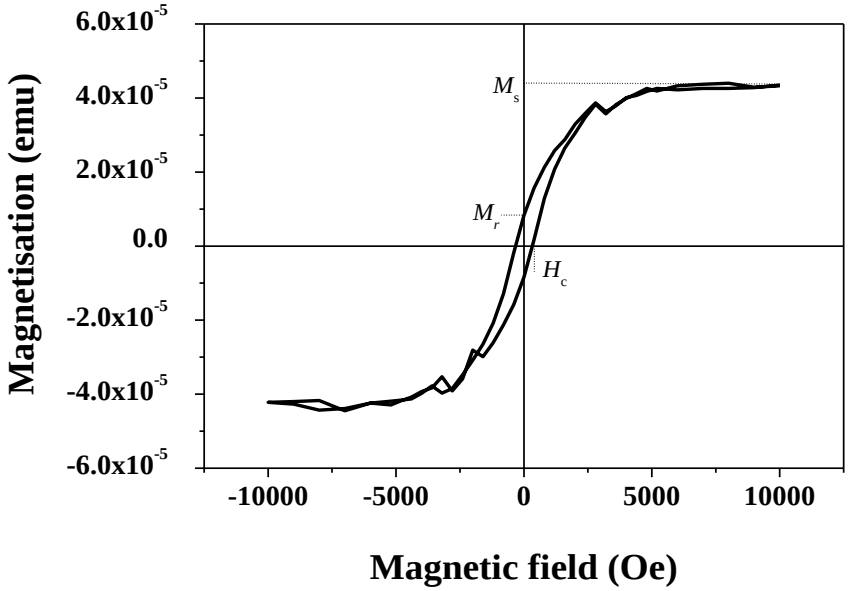

Figure 2.5: A hysteresis loop of of 5% Fe-doped In_2O_3 thin film. The saturation magnetisation, M_s, the remanent magnetisation, M_r and the coercive field, H_c are indicated.

By application of a small external magnetic field to a sample of ferromagnetic material, its magnetisation starts to increase gradually and reversibly. When the magnetic field is increased, the magnetisation increases until it reaches a constant value. This is the saturation magnetisation, M_s, at which the sample is magnetised.

If the magnetic field is decreased to zero, the magnetisation does not return to zero. Instead it reduces to a value known as the remnant magnetisation or remanence, M_r. To reduce the magnetisation of the already saturated sample to zero, the magnetic field must be reversed. The value of the magnetic field at which the sample is fully demagnetised is called the coercive field or coercively, H_c. The M_s, M_r and H_c quantities usually enable the material class of a sample to be identified.

2.4.4 Antiferromagnetism

For an antiferromagnetic material, half of the magnetic moments are aligned in one direction and the other half in the opposite direction. The ordered magnetic moments can be considered to lie on two sub-lattices. This means that there is no net magnetisation of the antiferromagnetic material.

As with ferromagnetic material, there is a critical transition temperature which is known as the Néel temperature, T_N. Above this temperature, the magnetic moments are disordered and the antiferromagnetic material becomes paramagnetic. Below T_N, however, there is a net magnetisation due to different magnetisations of the two sub-lattices. Hence, this can be used as a magnetic ordering parameter for antiferromagnetic materials.

The magnetic susceptibility of an antiferromagnetic material is temperature dependent and it is small and positive at all temperatures. For temperatures above the T_N, the magnetic susceptibility follows the Curie-Weiss law, which is given by:

$$\chi = \frac{C}{T + \theta_N} \tag{2.25}.$$

where θ_N is the Curie-Weiss constant, where θ_N is often considerably larger than T_N.

2.4.5 Ferrimagnetism

This occurs where two dissimilar sub-lattices tend to align antiparallel. If the magnetisations of the two sub-lattices are not equal there will be a net spontaneous magnetisation in the direction of the larger sub-lattice magnetic moment.

It is worth mentioning that in a number of materials, neighbouring magnetic moments are not fully aligned parallel or antiparallel to each other, but at an angle. This arrangement is referred to as a canted antiferromagnetic state, which occurs as an intermediate state between the ferromagnetic and antiferromagnetic states.

2.5 EXCHANGE INTERACTIONS

Different exchange interactions occur in different magnetic systems. Thus, exchange interaction type is an important factor in determining which of the magnetic states described above exist in a system. These interactions are divided into two main categories: direct and indirect interactions.

2.5.1 Direct Exchange Interactions

A direct exchange interaction between the magnetic dipole moments of atoms (ions) is known as the dipole–dipole magnetic exchange interaction. Since the energy of this kind of interaction is extremely small, of the order of ~ 10^{-23} J, it is too weak to be responsible for magnetic ordering above ~ 1 K. This is because many ferromagnetic materials retain their magnetic ordering at Curie temperatures of the order of 1000 K. The exchange interaction energy required to break such ordering is of the order of 10^{-20} J, i.e. it is five orders higher than the energy of dipole-dipole interactions.

Dipole-dipole interactions require extremely low temperatures which cannot be reached in our experiment. These interactions then are irrelevant to our studies and do not influence the magnetic data of the systems investigated in this thesis.

There is another mechanism of direct exchange interaction that exists between magnetic moments localised on atoms. This interaction produces a strong but short range coupling which decreases rapidly with distance between interaction atoms.

Thus, when two free atoms are close enough to each other, then their wave functions overlap. According to the Pauli exclusion principle, the overall wave functions must be antisymmetric. So that, if the spatial part of the wave function is symmetric, the spin part of the wave function must be an antisymmetric state ($S = 0$). If the spatial part of the wave function is antisymmetric, the spin part of the wave function must be a symmetric state ($S = 1$).

Hence, electrons with parallel spins always occupy different spatial orbitals to avoid each other; meaning that the average distance between them is large and as a result the electron-electron repulsion energy is reduced.

2.5.2 Indirect Exchange Interactions

When the magnetic moments are separated by a relatively large distance, then they cannot be coupled through direct exchange interaction. In this situation, the exchange interaction can occur indirectly. A number of indirect exchange mechanisms can interpret the magnetic coupling of many magnetic oxides. These mechanisms are known as super-exchange, double exchange and RKKY.

2.5.2.1 Super-exchange Interactions

In this type of interactions, non-neighbouring magnetic cations are mediated via a non-magnetic anion. Such interactions occur, for example, in transition metal

oxides [10]. The super-exchange interaction contains a virtual transfer of two electrons simultaneously; resulting in the formation of an excited state.

In the case of a half-filled *d* orbital, such as MnO, there are two possible configurations of the *d*-orbitals to be coupled by an oxygen *p*-orbital: these are antiparallel and parallel spins. However, the antiparallel spin configuration is favoured since it is lower in energy than the parallel spin configuration. This is because both electrons of the oxygen *p*-orbital can be coupled with the unoccupied *d*-orbitals.

The super-exchange interaction is sensitively dependent on geometry; this is why the M-O-M bond angle is an important factor in determining the strength and type of super-exchange interaction. Thus, the super-exchange interaction can be a strong antiferromagnetic or weak ferromagnetic one, and these are respectively presented in Figures 2.6 (a) and 2.6 (b).

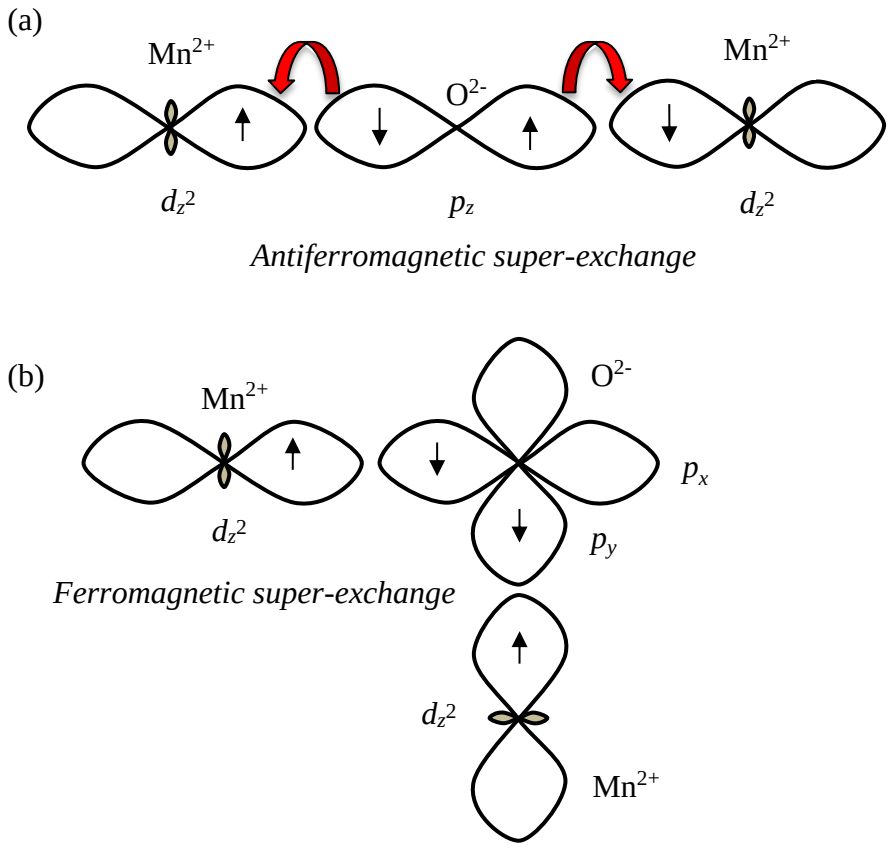

Figure 2.6: Schematic diagram of the indirect super-exchange interactions of MnO, (a) antiferromagnetic super-exchange and (b) ferromagnetic super-exchange. Adapted from reference [12].

The above classification of the super-exchange interaction is summarised in the following Goodenough-Kanamori rules:

1. Rule 1: When two cations have lobes of magnetic orbitals (i.e. singly occupied *d*-orbitals) pointing towards the same anion *p*-orbital, there is a reasonably large overlap. The super-exchange interaction is then strong and favours antiferromagnetic exchange to satisfy the Pauli exclusion principle. This interaction is known as 180° super-exchange where the M-O-M bond angle is 180°.
2. Rule 2: When the magnetic orbitals of two cations couple to different *p*-orbitals, then there is no overlap by symmetry. Thus, it is not possible for an electron from the *d*-orbital on one side to reach the *d*-orbital on the other side. The super-exchange interaction in this case is ferromagnetic and relatively weak; this is known as 90° super-exchange where the M-O-M bond angle is 90°.

The 90° super-exchange interaction is commonly known to be several times weaker than the 180° super-exchange interaction. Thus, the super-exchange interaction is generally antiferromagnetic because the overlap is larger than zero.

2.5.2.2 Double Exchange Interactions

This exchange interaction was proposed by Zener to explain the ferromagnetism observed in perovskite manganites [22]. Unlike the ferromagnetic super-exchange interaction, the double exchange mechanism requires the existence of mixed-valence configuration and is expected to occur only in oxides containing two magnetic cations that have two different valence states, provided that the magnetic moments are parallel.

During the double exchange, in a system containing Mn^{3+} O^{2-} Mn^{4+} ions for example, there is a simultaneous transfer of two electrons: one from the oxygen to the empty e_g orbital of the Mn^{4+} ion and the other from the e_g orbital of the Mn^{3+} to the oxygen ion. Thus, the configuration becomes Mn^{4+} O^{2-} Mn^{3+} and has the same energy as the previous configuration since the spin orientation is preserved, resulting in a ferromagnetic alignment, as shown in Figure 2.7 [16, 17].

Another example of the double exchange interaction is found in magnetite (Fe_3O_4) which contains Fe^{2+} and Fe^{3+} ions. In this case, an electron transfers from the Fe^{2+} ($3d^6$) ion to the oxygen ion which in the same time transfers an electron of the same orientation to the Fe^{3+} ($3d^5$) ion. Therefore, the double exchange between Fe^{2+} and Fe^{3+} ions is ferromagnetic [21-23, 25].

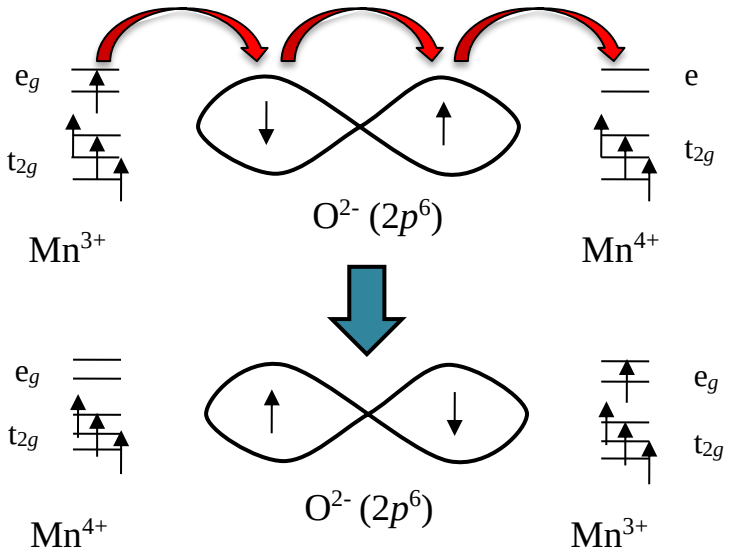

Figure 2.7: Schematic diagram of the indirect ferromagnetic double exchange interaction between the Mn^{3+} and Mn^{4+} ions via the *p* orbital of the O^{2-} ion. Adapted from reference [12].

2.5.2.3 RKKY Exchange Interaction

This interaction occurs when there are both localised and band electrons. In rare-earths, for example, the observed magnetisation was found to be due to the 4*f* electrons. However, since these electrons are strongly localised then there is no direct interaction. Instead, the interaction between the localised magnetic moments of the 4*f* shell is obtained via the electrons in the 5*d* or 6*s* conduction band. This is known as the RKKY interaction and is used to interpret the resulting magnetism in metals.

The mechanism of this interaction depends on polarising the delocalised (itinerant) conduction electrons by a localised magnetic moment; this polarisation in turn interacts magnetically with the neighbouring localised magnetic moment that is located at a distance *r* from the first magnetic moment [8, 13].

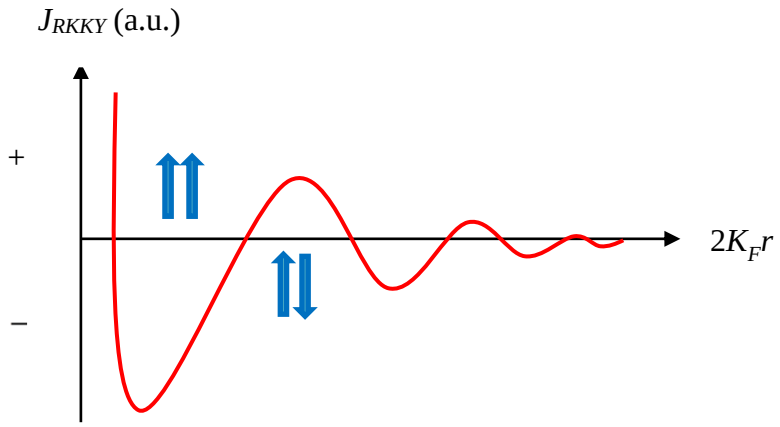

Figure 2.8: Schematic diagram of the RKKY indirect ferromagnetic/antiferromagnetic exchange interactions depending on the interatomic distance *r*. Adapted from reference [8].

RKKY is a long-range interaction compared to the direct exchange interaction. The main feature of this interaction is the oscillatory behaviour that varies its sign depending on the distance between the interacting magnetic moments. Thus, the resulting RKKY interaction can be either ferromagnetic or antiferromagnetic, as shown in Figure 2.8, where K_F is the Fermi wave vector [26, 27].

2.6 REFERENCES

1. J. M. D. Coey, *Magnetism and magnetic materials*. (Cambridge University Press, Cambridge, 2010).
2. J. Crangle, *The Magnetic Properties of Solids.* (Edward Arnold, London, 1977).
3. N. A. Spaldin, *Magnetic materials:fundamentals and device applications*. (Cambridge University Press,Cambridge, 2003).
4. B. Cullity and C. Graham, *Introduction to Magnetic Materials*, 2nd edition. (IEEE PRESS, 2009).
5. C. Kittel, *Introduction to solid state physics*, 8th edition. (Wiley & Sons, New York, 2004).
6. R.M. White, *Quantum Theory of Magnetism:* Magnetic Properties of Materials, 3rd edition. (Springer-Verlag, Berlin, 2007).
7. J.R. Hook and H.E. Hall, *Solid State Physics*, 2nd edition (John Wiley & Sons, Chichester, 1991).
8. M. Getzla, *Fundamentals of Magnetism*, 1st edition. (Springer-Verlag Berlin Heidelberg, 2008).
9. S. Kouvel and R. H. Wilson, Journal of Applied Physics, Vol. **32**, 435–441 (1961).
10. J. Kübler, Physics Letters A, Vol. **81**, 81 – 83 (1981).
11. C. Zener, Physical Review, Vol. **82**, 3, 403-405 (1951).
12. M. Opel, Journal of Applied Physics, Vol. **45**, 033001 (2012).
13. K. Yosida, Theory of magnetism. (Springer, Berlin ; New York, 1996).
14. P.W. Anderson, Physical Review. Vol. **79**, 350 (1950).
15. P.W. Anderson, Physical Review. Vol. **115**, 2 (1959).
16. I. V. Solovyev *et al*, Physical Review. **B 87**, 144424 (2013).

17. S. A. Nikolaev *et al*, Physical Review. **B 89**, 064428 (2014).

18. J.B. Goodenough, Physical Review, Vol. **100**, 564 (1955).

19. J. Kanamori, Journal of Physics and Chemistry of Solids, Vol. **10**, 87-98 (1959).

20. J. Farrell *et al*, New Journal of Physics, Vol. **6**, 168 (2004).

21. A. J. Millis, Physical Review. **B 55**, 6405 (1997).

22. C. Zener, Physical Review**,** Vol. **81**, 440-444 (1951).

23. I.Di. Marco *et al*, Nature communications, Vol. **4**, 2645 (2013).

24. J.B. Goodenough, *Magnetism and the Chemical Bond*. (International science Publisher, New York, 1963).

25. K. H. Ahn *et al*, Physical Review. **B 64**, 115103 (2001)

26. T. Kasuya, Progress of Theoretical physics. Vol. **16**, 45 (1956).

27. K. Yosida, Physical Review. Vol. **106**, 893-898 (1957).

Chapter 3

EXPERIMENTAL BACKGROUND AND PROCEDURES

3.1 INTRODUCTION

This chapter discusses the wide range of experimental methods that were used for thin films preparation and investigation. This includes the production of bulk targets, which were used to prepare thin films by PLD technique. Thickness measurements of thin films were obtained using a Dektak surface profiler.

The experimental techniques that were utilised to investigate different properties of various magnetic oxide materials involve, (1) the study of the magnetic properties using a SQUID magnetometer, (2) structural properties using XRD, FIB, EDS, XANES and EXAFS measurements. It should be mentioned that all structural measurements, except some of the XRD measurements, were performed as a collaborative work with other groups, (3) optical properties using absorption spectroscopy through transmission and reflection measurements, and (4) magneto-optical properties using MCD spectroscopy in Faraday (transmission) geometry. In the following, each of the above-mentioned techniques and measurements will be introduced and discussed in more detail.

3.2 THIN FILM PREPARATION

Bulk targets of TM-doped In_2O_3 were prepared by mixing appropriate amounts of In_2O_3 and a TM dopant such as Fe and Mn. The Fe was obtained from three different precursors: FeO, Fe_3O_4 and Fe_2O_3, whereas the Mn was only obtained from the precursor Mn_2O_3. By successive grinding of the mixture and then sintering it at different temperatures, stoichiometric targets of TM-doped In_2O_3 were obtained. A powerful pulsed laser, as will be described later in **section (3.2.2)**, was used to ablate a small part of the surface of a bulk target onto a sapphire substrate. Growth conditions such as oxygen partial pressure and substrate temperature were closely monitored during the ablation procedure.

3.2.1 Target Fabrication

A variety of different bulk targets were produced using the technique of solid state reaction. In this method, the required mass of each component of the target was calculated and then weighed with an electrical balance. All components were then ground in a mortar and pestle. All powders used were purchased from Alfa Aesar and were of the high purity obtainable (99.99%).

As an example, the details of the preparation of the target of 5% Fe_2O_3-doped In_2O_3 are as follows: first, we need the atomic weights (A_{In}, A_O and A_{Fe}) for In, O and Fe, respectively, in order to calculate the atomic weight for the whole compound. In all cases, we need to know how many metal ions there are per gram. In In_2O_3, for example, this is:

$$N_{In} = \frac{2}{(2A_{In} + 3A_O)\,\text{amu}} = \frac{1}{(114.8 + 24)\,\text{amu}} = \frac{1}{138.8\,\text{amu}} \qquad (3.1).$$

Similarly, for Fe_2O_3 it is:

$$N_{Fe} = \frac{2}{(2A_{\mathrm{Fe}} + 3A_{\mathrm{O}})\,\mathrm{amu}} = \frac{1}{(55.85 + 24)\,\mathrm{amu}} = \frac{1}{79.85\,\mathrm{amu}} \tag{3.2}$$

For 5% of Fe in In_2O_3 we need a number ratio of:

$$\frac{N_{Fe}}{N_{In}} = \frac{5}{100 - 5} \tag{3.3}$$

The mass ratio then can be given by:

$$\frac{M^{Fe_eO_3}}{M^{In_2O_3}} = \frac{5}{95}\left(\frac{79.85}{138.8}\right) \tag{3.4}$$

This gives the value 0.0303, meaning that each gram of In_2O_3 needs to be mixed with 30.30 mgs of Fe_2O_3. So, for a target of ~ 10 gm we need 10 gm of In_2O_3 and 303.0 mgs of Fe_2O_3.

The initial powder mix was ground by hand in a mortar and pestle for 20 min. After that, the powder was placed in a high-quality ceramic crucible and fired at a relatively low temperature of 300 $^{\circ}$C for 12 hours in air in a furnace. This procedure was repeated for another two temperatures: 600 $^{\circ}$C and 900 $^{\circ}$C.

After the final anneal, the mixture was placed in a *Specac* die, which was evacuated with a roughing-pump and, using a manual hydraulic press, compressed to 25000 kPa. This produced a relatively dense, cylindrical pellet of diameter 25 mm and thickness between 2 to 5 mm, depending upon the amount of the initial powders used.

The pellet was then given a final anneal at a maximum temperature of 1000 ^{0}C . All anneals were performed in air.

All the other three targets FeO-, Fe_3O_4- and Mn_2O_3-doped In_2O_3 were produced using the same method. All the TM-doped In_2O_3 films were deposited on *c*-cut (0001) sapphire substrates.

3.2.2 Pulsed Laser Deposition (PLD)

PLD technique is one of several methods used to grow high-quality stoichiometric thin films. Among these techniques are sputtering, molecular-beam epitaxy (MBE) and chemical vapour deposition (CVD) [1, 2].

The use of PLD has a number of advantages, one of which is that the laser is located outside the deposition chamber so that it is possible to fabricate multilayer films by successive ablation of different targets without opening the chamber. The targets used in the PLD technique are rather small in comparison to a large size target required for the sputtering technique.

Another advantage is the flexibility in controlling the growth parameters during the deposition, these include the gas partial pressure and temperature [3]. Moreover, the overall experimental process is a relatively simple and straightforward one.

Nevertheless, there are some disadvantages of the PLD technique, such as the degradation of the target by the laser during ablation, which may reduce film quality. The uniformity of the film might also be affected due to one of the main drawbacks of PLD, which is called “splashing”. This phenomenon occurs due to the fast vaporisation that expels a liquid layer at or close to the surface, leading to the expulsion of the molten particles. This, therefore, induces the formation of defects such as boulders that appear on the film surface. These boulders can be detected by scanning electron microscopy (SEM) [4].

The PLD system consists essentially of three parts: laser, vacuum system and deposition chamber, as shown in Figure 3.1.

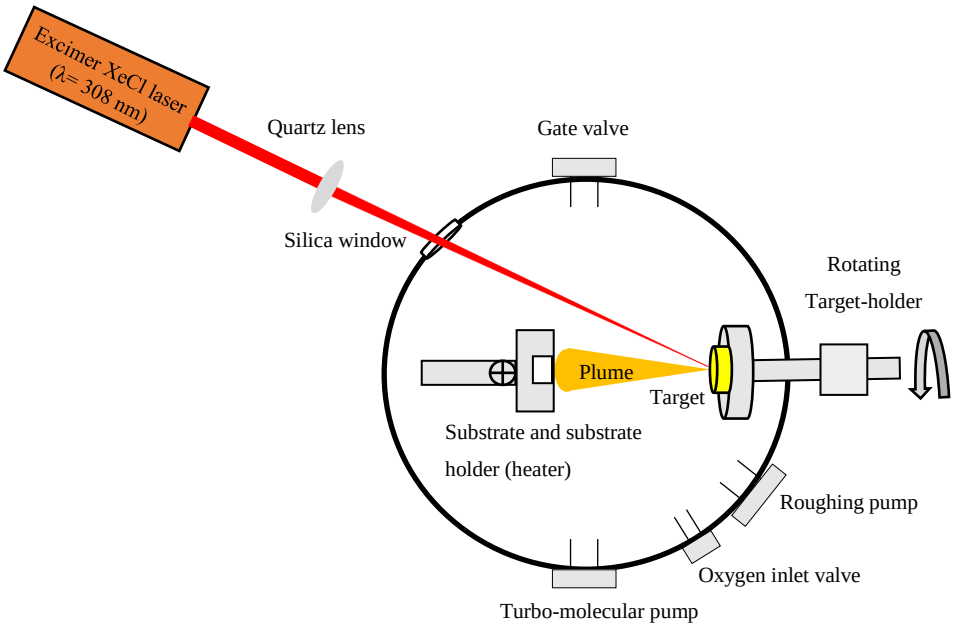

Figure 3.1: Schematic diagram of the PLD system.

The laser used in this work was an excimer XeCl laser, (Lambda Physik LEXTRA 200), operating at a wavelength of 308 nm. The laser could produce a pulse of energy of up to 400 mJ and a pulse length of 28 ns operating at a 10 Hz repetition rate. The laser beam is focused by a quartz lens, which is positioned close to the silica window of the deposition chamber, onto the surface of a rotating target, creating a spot size of about 3 mm^2 [5].

The deposition chamber is constructed from stainless steel. The substrate is oriented parallel to the target at a fixed distance of only a few centimetres, usually 3.5 cm. The target is rotated by a motor at a speed of 60 rpm which prevents ablating the same spot constantly. This can reduce the formation of the molten particles mentioned previously. The chamber can be pumped down to a minimum base pressure of 10^{-5} Torr. This is performed by two pumps: a roughing pump and a turbo-molecular pump (TMP).

However, the pressure inside the deposition chamber can be varied from base pressure up to a few hundreds of mTorr of oxygen. This can be controlled by injecting

oxygen in a controlled manner via three valves: oxygen inlet valve, roughing pump valve and gate valve.

For depositing a film, the target is placed in a rotating holder. Then a small HeNe laser is used as a pointer, striking the target at approximately the position where the ablating laser would be incident. A new sapphire substrate is cleaned with ethanol in an ultra-sonic bath. The substrate holder, which has two electric-heater elements sandwiched inside it, is carefully cleaned with methanol in order to remove all traces of the previous run. The substrate is then clamped onto the substrate holder using two small, metal clamps.

It is worthwhile noting here that the areas underneath the clamps represent the blank substrate where there is no film deposited, as shown in Figure 3.2. These areas are used as a reference when measuring film thickness using a Dektak surface profiler; this will be discussed in more detail in the section on film thickness measurement.

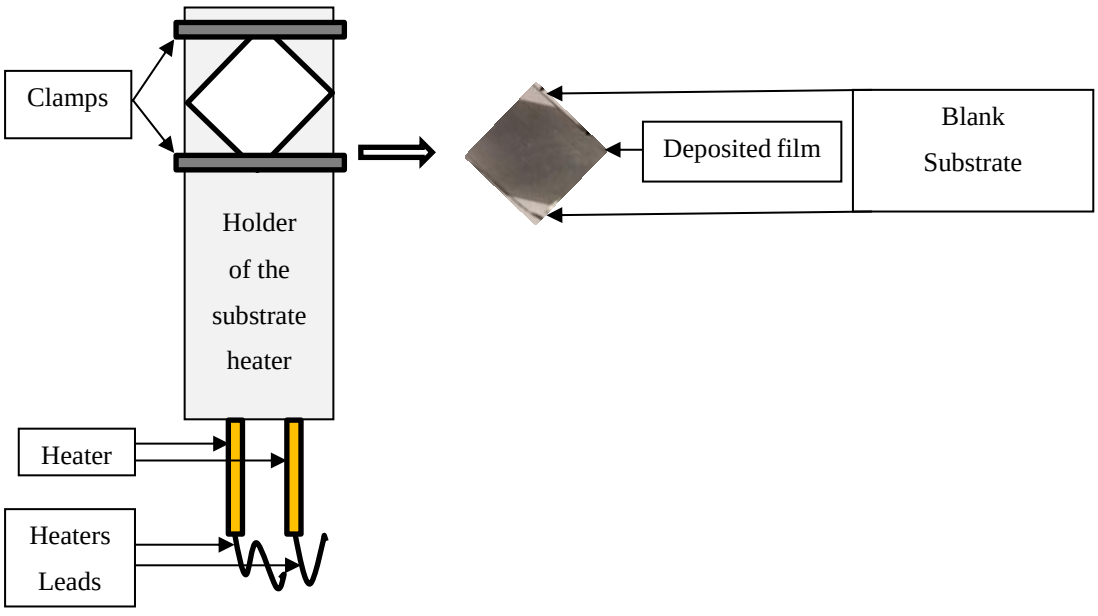

Figure 3.2: Schematic of the substrate holder and a photograph of the deposited film, showing the film-free areas in the substrate.

The deposition temperature is achieved by connecting the two substrate heaters to a power supply. The substrate temperature is then monitored during the deposition using a chromel-alumel thermocouple.

All connections between the power supply, the substrate heaters and the thermocouple are checked before the deposition chamber is sealed in order to ensure that they are working correctly. A substrate temperature of 450 °C was chosen for growing all the TM-doped In_2O_3 films. This is because, at higher temperatures, the transition metal ions tend to form isolated clusters [6, 7].

The chamber is pumped down to the base pressure of 5×10^{-5} Torr using the rotary and TMP pumps. The chamber pressure is continuously monitored by two pressure gauges: initially a Pirani gauge and then a Penning gauge. These gauges measure the pressure in different ranges, where the Pirani gauge measures the pressure down to about 10^{-3} Torr, and the Penning gauge is used for the measurement of pressure down to 10^{-5} Torr.

For a growth at oxygen partial pressure, the deposition chamber is filled back with oxygen via the oxygen inlet valve. The TMP valve is shut and the roughing pump valve remains opened, where a careful balance between the gate valve and the oxygen inlet valve is taken into account in order to maintain an oxygen flow for the desired pressure.

The XeCl laser beam is focused onto the rotating target. The target surface absorbs the beam, as a result, the target surface is ablated and evaporated. This forms a plasma plume that is perpendicular to the plane of the substrate, to which it transports atoms, molecules and ions. These condense onto the heated substrate, where a thin film sample is deposited.

At the end of the deposition period, the laser and the target-rotation motor are switched off and the substrate is cooled down to room temperature. Then, the pressure inside the chamber is raised to atmospheric pressure and finally the substrate holder is removed from the deposition chamber.

It is worthwhile mentioning that the plume shape is affected by different deposition pressures, as shown approximately in Figure 3.3. Hence, increasing oxygen pressure during the deposition reduces the amount of ablated species from the target, compared to the base pressure. As a result, the deposition time of a film grown in an oxygen atmosphere increases as compared to that of a film of comparable thickness grown at base pressure [8-10].

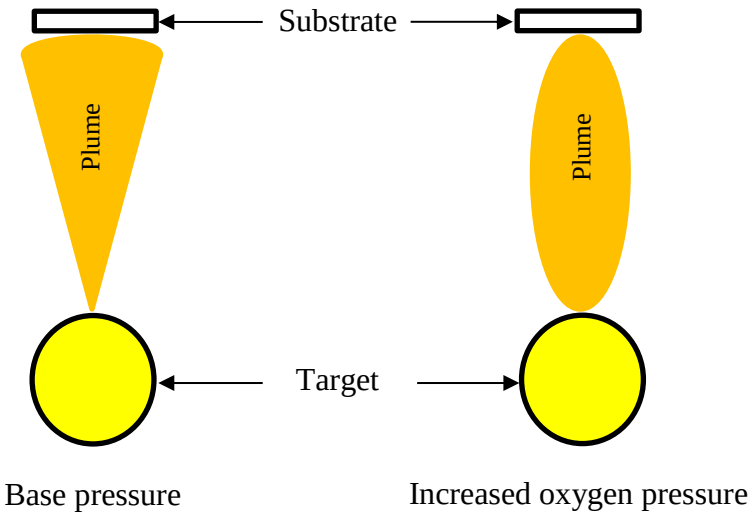

Figure 3.3: Sketches of plume shape of deposition process at two different oxygen pressures; base pressure of ~ 2×10^{-5} Torr and oxygen partial pressure of ~ 2×10^{-3} Torr.

The substrate temperature, the chamber pressure and the plume quality are monitored and recorded throughout the deposition run, typically every 5 minutes, in order to be used as a reference for the next run.

3.3 FILM THICKNESS MEASUREMENT

Thickness measurements of the TM-doped In_2O_3 films were made with a Veeco Dektak profilometer (Model 150). It is a microprocessor-based instrument that can provide different surface measurements using a diamond-tipped stylus profiler. This can accurately measure vertical features from 10 nm up to 65 knm [11]. The vertical movement of the stylus across the film surface is translated into changes in signal through an electrical circuit. This signal change is then converted to a height and is displayed as a 2D plot of the film surface [12].

A film thickness is measured by moving the stylus profiler across the substrate-film edge, from one blank region of the substrate to another, which is produced by the two clamps that cover two corners of the sapphire substrate during the deposition process, as mentioned previously. This movement of the stylus represents the measurement that is used to deduce the value of film thickness, as in Figure 3.4.

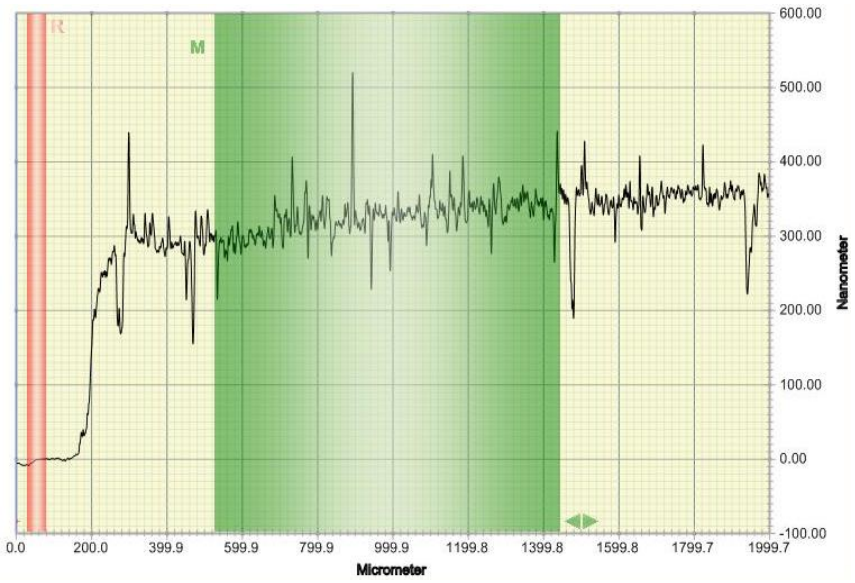

Figure 3.4: Film thickness data as measured by the Dektak surface profiler for a 5% Fe_2O_3-doped In_2O_3 sample.

The thickness of the film of 5%Fe_2O_3-doped In_2O_3 grown on a sapphire substrate as a function of deposition time is plotted in Figure 3.5, where the film thickness depends linearly on the time as expected.

The growth rate in this case is estimated to be about 27 nm/min. Several measurements of thickness are recorded in order to calculate an average. The uncertainty in the Dektak measurements is estimated to be ± 10% [10, 13].

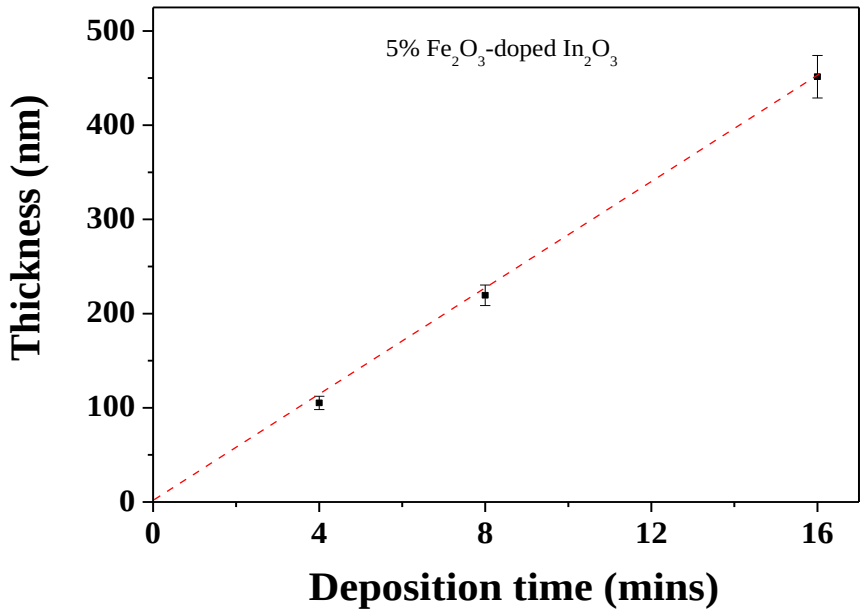

Figure 3.5: Thicknesses of 5% of Fe_2O_3 doped In_2O_3 thin films grown on sapphire substrates as a function of deposition time at a fixed oxygen pressure of 2×10^{-5} Torr and a substrate temperature of 450 ˚C.

3.4 MAGNETIC MEASUREMENTS

The SQUID magnetometer is one of the most sensitive sensors of magnetic flux that is used to measure small changes in the magnetic property of a sample when it is exposed to different magnetic fields or temperatures. Hence, it is a useful device that is used to obtain different magnetic measurements, providing crucial information about the magnetic properties of a material.

The SQUID magnetometer consists of a SQUID connected to detection coils which are located inside a superconducting magnet. The SQUID comprises of a Nb superconducting loop which has a single Josephson junction. This SQUID loop is inductively coupled to a field-sensing coil via superconducting transformers. The other side of the SQUID loop is inductively coupled to a RF circuit to read out any changes in the SQUID loop [17]. The RF circuit is excited by a RF current that oscillates at ~ 20 MHz. The SQUID is shielded from the superconducting magnet in order to detect only the current from the detection coils [11, 17].

A Radio Frequency (RF) SQUID magnetometer, model MPMS-5 manufactured by *Quantum Design*, was used to obtain all magnetic measurements of all the samples reported in this thesis [14, 15]. This instrument can operate over a temperature range from 2 K to 400 K and with magnetic fields up to 50000 Oe.

3.4.1 Theoretical Background

The SQUID does not directly measure the magnetic moment of a sample. Instead, it is based on the measurement of a voltage induced in the field-sensing coil by the magnetic response from a sample.

Since the field-sensing coil forms a closed loop with the SQUID, any variation in the magnetic flux produces a variation in the persistent current in the superconducting loop, which is proportional to the variation of the magnetic flux. As a result, the corresponding changes in the SQUID output voltage represent the magnetic moment of the sample [17]. The variations in the magnetic flux are converted using a least-squares fitting program to a theoretical expression in order to obtain the magnetic moment of the sample [11].

The lines of the magnetic flux penetrating the superconducting loop are trapped in discrete levels and can only exist in multiples of a quantum magnetic flux

(fluxon) that is given by $\Phi_0 = h/2e = 2.06 \times 10^{-15}$ Wb; where 1 Wb/m^2 = 1 T; h is Planck's constant and e is the electronic charge. However, when the magnetic field generated by the sample is removed, the trapped magnetic flux results in an induced current that circulates around the loop in order to sustain the magnetic flux inside it. As long as the superconducting loop is kept below its transition temperature, the current flows indefinitely, without any resistance [11, 17].

The phase of the oscillating voltage across the resonant circuit varies sensitively as a periodic function of the magnetic flux threading through the loop. The SQUID, therefore, functions as a sensitive magnetic flux-to-voltage transducer. Hence, using suitable electronics to monitor the voltage amplitude, the SQUID can measure extremely small changes in the magnetic flux which are proportional to the magnetic moment of a sample [16, 17].

3.4.2 Experimental Setup

A sample is mounted on a long, uniform sample holder, in practice, this was a plastic drinking straw. The sample is held in position towards the centre of the straw using a thin cotton thread. The drinking straw is then attached to the end of a rigid 3 mm diameter stainless steel rod. This rod is then introduced into the SQUID via an air-lock located at the top the system. Before the sample-rod is completely inserted into the SQUID system, it is vented and purged with helium gas in order to prevent the sample chamber from being contaminated by atmospheric gases.

The top of the sample-rod is connected to a stepping-motor which is used to drive the sample through the pick-up coils in a series of discrete steps. Before any measurement can be made, the centre of the sample must be positioned at the centre of the pick-up coils to obtain accurate results. A full scan over a length of 4 cm is performed to determine the position of the sample, after which the sample can be

centred manually or automatically. For an accurate centring, the procedure is repeated over a shorter scan length, typically 2 cm. Once this is completed, the measurement sequence can then be started.

During a measurement, the sample is moved through the field-sensing coils, which are configured as a second-order gradiometer; this, in principle, ensures that the field-sensing coils are not sensitive to the external magnetic field that is constant, or to their first-order derivatives, but are only affected by the second-order field variations. Accordingly, the sample generates a field that in turn induces a supercurrent in the field-sensing coils and therefore a magnetic flux through the SQUID loop. Recording these measurements as a function of different magnetic fields allows us to gain data about the sample magnetisation as a function of externally applied magnetic field.

There are two types of measurement that will be considered in this thesis. The first type of measurement is undertaken as a function of an external applied magnetic field, which is swept over a range from + to – H, whereas the temperature is fixed at a chosen value. This is called a magnetic hysteresis (M-H) loop measurement.

In the second type of measurement, the magnetic field is held constant, whereas the temperature is swept whilst recording the magnetisation data of a sample. This is called a zero-field-cooled/field-cooled measurement, ZFC/FC. These measurements shall be explained in more detail next.

There are generally two contributions to the total raw signal from the sample: one contribution from the film, and the other from the substrate. The contribution from the film is a ferromagnetic with, possibly, a paramagnetic contribution. In addition, there may even be a very small diamagnetic contribution, depending upon the materials in the target. The contribution from the substrate is essentially diamagnetic, but there

may be a small paramagnetic contribution arising from paramagnetic impurities in the substrate.

3.4.2.1 Magnetic Hysteresis Loop Measurement

In this type of measurement, the magnetisation of a sample is studied as a function of the magnetic field, the temperature is fixed, typically at 5 K or 300 K whilst the external magnetic field is increased from zero up to 10000 Oe, and decreased through zero to – 10000 Oe, and then back again through zero to + 10000 Oe. The magnetic field can be either applied parallel or perpendicular to the plane of the sample; this depends upon how the sample is mounted in the drinking straw. From the obtained data the magnetisation can be plotted as a function of the magnetic field where a magnetic hysteresis loop is produced.

Such a measurement is widely used to determine the general important characteristics of a ferromagnetic material and yield information such as saturation magnetisation, coercivity, and remanence.

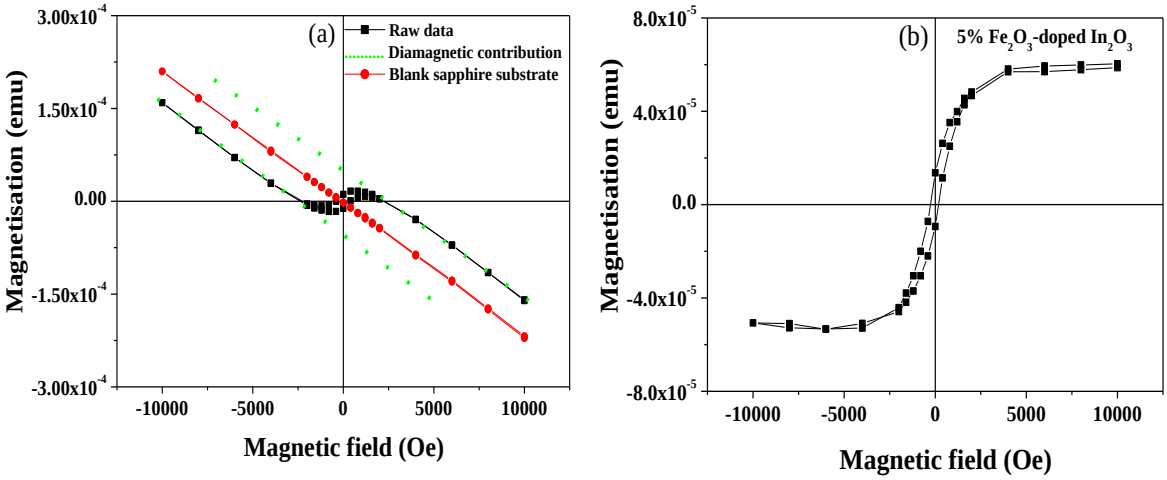

Figure 3.6: (a) Raw data of hysteresis loop measurement of a 5% Fe_2O_3-doped In_2O_3 sample measured at 300 K (black squares) and the hysteresis loop measurement of a balnk sapphire substrate (red circles). (b) The hysteresis loop of the 5% Fe_2O_3-doped In_2O_3 after the subtraction of the diamagnetic and paramagnetic contributions.

The black curve in Figure 3.6 (a) shows the raw, uncorrected SQUID data for a hysteresis loop measured at 300 K for a 5% Fe_2O_3-doped In_2O_3 film grown on a sapphire substrate, while the red curve is the hysteresis loop measurement of a blank sapphire substrate. There are different magnetic contributions that could arise from both the film and the substrate on which it was deposited.

It can be clearly seen from the black curve in the Figure 3.6 (a) that there are two distinct contributions to the raw data: a linear contribution that dominates at high fields, and a saturating ferromagnetic contribution evident at low fields. Since diamagnetism is temperature independent, negative, and varies linearly with applied magnetic field, therefore, the high-field linear variation, illustrated by the dotted green lines is identified as a diamagnetic contribution; this is mainly due to the substrate. Nevertheless, there might be a temperature dependent paramagnetic contribution arising from some unreacted components in the film.

To separate the ferromagnetic contribution from other contributions, the diamagnetic contribution from the substrate is subtracted (added) from the raw data. This subtraction produces a hysteresis loop that saturates at a certain magnetic field, usually at about 3000 Oe. Beyond this field, a linear magnetisation can be noticed where a straight line can be fitted. The slope of this line is calculated and then subtracted from each point to only obtain the ferromagnetic contribution, as in Figure 3.6 (b).

The existence of different contributions in the same film indicates the complicated magnetic nature of the film. Such contributions can be attributed to the contaminants, which can also play a role in this matter since they might result from the growth and/or handling of the sample [18].

3.4.2.2 Zero-Field-Cooled/Field-Cooled Measurements

In this type of measurement, the temperature dependence of the magnetisation is studied in two regimes: ZFC and FC. In the ZFC mode, the sample temperature is lowered from room temperature, 300 K, in zero magnetic field where all magnetic particles are randomly oriented. At a finite low temperature, usually 5 K, the magnetic moment of the particles are frozen (immobilised) in different directions.

In the ZFC measurement, the sample is cooled down to 5 K in zero magnetic field. When the temperature stabilises, a small magnetic field, typically 100 Oe, is applied and the magnetisation of the sample is then measured while increasing the temperature from 5 K to 300 K.

In the FC measurement, however, the magnetisation is measured as the sample is cooled from 300 K to 5 K in the same applied magnetic field. In this situation, as the temperature is lowered, the aligned magnetic moments are frozen and remain aligned in the direction of the applied field. Usually, the ZFC and FC measurements are performed in a single run. Both data of the ZFC and FC magnetisations are plotted as functions of temperature in the same graph. The aim of ZFC/FC measurements is to show the dependence of the magnetisation on temperature as well as the magnetic field history.

Using the ZFC/FC magnetisations, the magnetic susceptibility can be calculated. If the inverse of the magnetic susceptibility is plotted as a function of temperature, this allows one to obtain information about the Curie's constant using the Curie-Weiss law which was previously introduced in **equation (2.24)**.

ZFC/FC measurements are shown in Figures 3.7 (a) and 3.7 (b) for the GMO film grown on LSAT (100) substrate and for the 5% Fe-doped In_2O_3 film grown on a sapphire substrate. The diamagnetic contributions arising from the LSAT (100) and sapphire substrates have been subtracted. The data in Figures 3.7 (c) and 3.7 (d) show the ZFC/FC magnetisations of blank LSAT (100) and sapphire substrates, respectively.

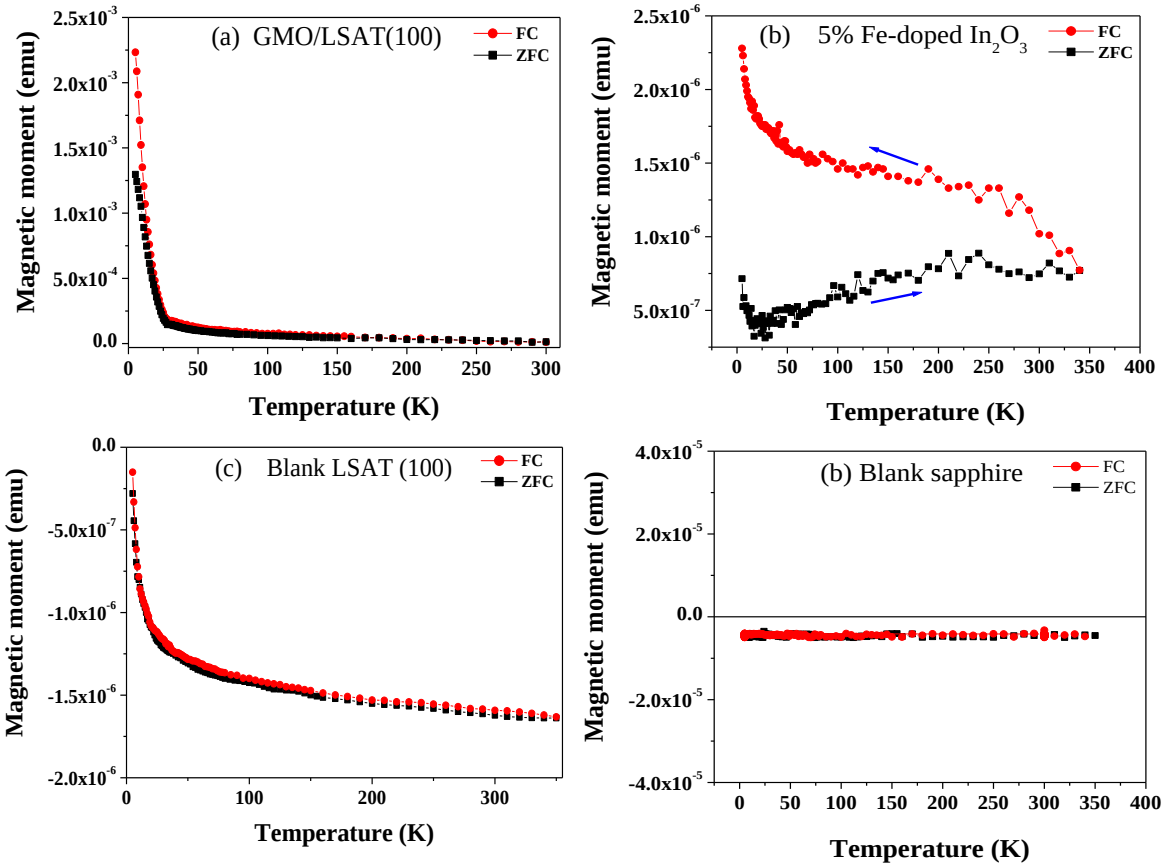

Figure 3.7: (a) and (b) the ZFC/FC measurements of a GMO film and 5% Fe-doped In_2O_3 film grown on LSAT (100) and sapphire substrates, respectively. (c) and (d) the ZFC/FC measurements of blank LSAT (100) and sapphire substrates, respectively.

If there is a blocking, ZFC/FC measurements can also provide information about the size of magnetic nanoparticles in magnetic materials. Such materials are generally characterised by a certain temperature, which is known as the blocking temperature, T_B. Above this temperature, the nanoparticles of a ferromagnetic material

are characterised by superparamagnetic behaviour. Below the blocking temperature, however, the magnetic moments of the particles are frozen in the field direction [19].

In the absence of an external magnetic field, each particle tends to align its magnetic moment along a certain direction (a so-called easy direction of magnetisation), which is defined by the magnetic anisotropy of the material. If there is only one preferred direction, then the magnetic nanoparticle is said to have uniaxial anisotropy.

At thermal equilibrium, there will be two energetically minimum directions along the easy axis of magnetisation. Between these two directions, there is an energy barrier of size *KV*, where *K* is the magnetic anisotropy constant, and *V* is the particle volume [20]. Thermal energy, $k_B T$, affects the magnetic nanoparticles by randomly flipping their directions of magnetisations. The particle size can be obtained from the well-known Bean-Livingston equation [20]:

$$25 k_B T_B = KV \tag{3.5}$$

The time to perform such a process is called the relaxation time, τ. In a typical magnetisation measurement of a particle. The duration of this measurement is, for simplicity, assumed to be 100 sec [17, 20].

3.5 STRUCTURAL MEASUREMENTS

In this section, different types of measurements will be discussed, since they provide different information about the structure of a material. These measurements include; XRD, FIB, EDS, XANES, and EXAFS.

XRD is used to determine any change in the lattice spacing/constant, which is affected by different parameters, such as substrate type, film thickness and gas pressure.

XRD can also be used to check for the presence of impurity phases. However, not all the impurity phases can be identified by the XRD measurement due to its detection limits.

As mentioned previously, some of the XRD measurements were carried out in Russia and China. At the University of Sheffield, the instrument used was a Bruker D2 X-ray diffractometer that used a CuKα radiation, λ = 1.5406 Å. The X-rays consist of Kα and Kβ radiations where the intensity of the Kβ radiation can be reduced by using blocking-filters which depend on the anode material. In the case of CuK$_\alpha$, the high-energy rays are absorbed by a filter, leaving only the Kα ray; this is more intense than the Kβ ray and, because the wavelength of the Kα ray is useful for inter-planar spacing, it is usually preferred to be used in the XRD measurement for crystalline material [21].

Since the wavelength of the X-rays is comparable or smaller than the interatomic distance of solids, they can be strongly diffracted by the atoms of the solids. Therefore, the crystal structure of solid materials can be determined. So that, by directing a monochromatic beam of X-rays onto a crystalline lattice, a constructive interference can be produced when it satisfies the conditions expressed by Bragg's law:

$$n\lambda = 2d \sin \theta \tag{3.6}$$

where n is an integer, λ is the wavelength of the radiation, d is the lattice spacing and θ is the incident angle of the X-rays [21, 22].

In a cubic material, the lattice constant, α, and the spacing between the diffracting planes are related by the expression:

$$d = \frac{\alpha}{\sqrt{h^2+k^2+l^2}} \tag{3.7}$$

where (h,k,l) are the Miller indices of the diffracting planes.

The XRD θ–2θ scans are used to obtain the lattice spacing of a material [23]. When the diffraction peaks of the material are identified, and by knowing the lattice constant of the material, then the separation between planes can be calculated [22, 23].

The lattice spacing data can also provide information about the strain introduced to the material. More details in this regard can be found in **chapter 4** when discussing the strain introduced to the GMO by different orientations of LSAT substrates.

FIB is a versatile microscopy technique which can be used to destructively remove material through a process known as sputtering [24, 25]. The operational principle of FIB is to generate a beam of heavy ions from a liquid-metal ion source (LMIS), typically gallium (Ga), this source is connected to a tungsten pin. By heating the ion source, Ga atoms flow to the tip of the pin. Applying a strong electric field to the pin tip results in the extraction and ionisation of the Ga atoms. The Ga^+ ions are, therefore, accelerated up to 30 keV, then the ions are focused by electrostatic lenses into the surface of the sample [25-27].

The collision between the Ga^+ ions and the atoms in the sample results in the sputtering of a certain number of atoms. This collision generates ion-induced secondary electrons which can be used to produce a high-resolution image of the sample surface. In addition, since the FIB allows material removal by the primary ions beam, it is utilised as an excellent tool to form cross-sectional images of the sample; these can be then used to measure the sample thickness [24, 25, 27].

EDS is a powerful X-ray micro-analytical technique which provides information on the chemical composition of a sample [24, 25]. In principle, it can detect all elements with atomic number ($Z > 3$). The EDS system is conjugated with a SEM, which can be used to produce element distribution images [28].

When the sample is bombarded by a high-energy beam of electrons, then the electrons from the atoms close to the surface of the sample are ejected. As a result, electron vacancies are created which are filled by electrons from a higher energy state, generating X-rays in order to balance the energy difference between the two energy states [24, 28].

Since different elements have different atomic structures, then the energy of the emitted X-ray is characteristic of the energy difference between the energy states of each element. So that, the X-rays measurements can be converted into a final X-ray spectrum which allows one to identify the chemical elements present in the sample and also to determine their concentrations [24, 25, 28].

XANES and **EXAFS** belong to X-ray absorption fine structure spectroscopy (XAFS) that is an essential tool to obtain information about the electronic structure of a material. XAFS is a result of scattering of the photon emitted from an absorbing atom as a result of the photoelectric effect. This spectroscopy is used to determine the local geometric structure around the central atom. Thus, it can be utilised to detect any secondary phases that could be formed during the growth process [29-32].

When X-rays are incident on a sample, some of them are scattered and the others are absorbed. Accordingly, the absorption shows strong peaks when the photon energy is exactly able to excite electrons from the inner shell of the absorbing atom to unoccupied states, thus producing a photo-electron. These are called absorption edges, each of which results when a core electron absorbs energy equal to, or greater than, its binding energy. For instance, the excitation of an electron from the 1*s* state corresponds to the *K*-edge absorption [31].

Since different elements have characteristic energy levels, then they can be studied separately. Nevertheless, once the photo-electron escapes the absorbing atom,

its wave is backscattered by the neighbouring atoms, generating constructive and destructive interference regions, which are seen as maxima and minima in the XAFS spectrum, corresponding to the outgoing and backscattered waves, respectively [3, 29].

When the X-ray passes through a sample of thickness, x, the intensity, I, of the transmitted X-ray beam is reduced according to the expression:

$$I(x) = I_0 \, e^{-\mu x} \tag{3.8}$$

where μ is the linear absorption coefficient which depends on both the material and the photon energy, and I_0 is the intensity of the X-ray beam incident on the sample [29-32].

There are three main regions of an XAFS absorption spectrum from which the information of the electronic structure can be obtained: pre-edge, XANES, and EXAFS, these regions are shown in Figure 3.8 [3].

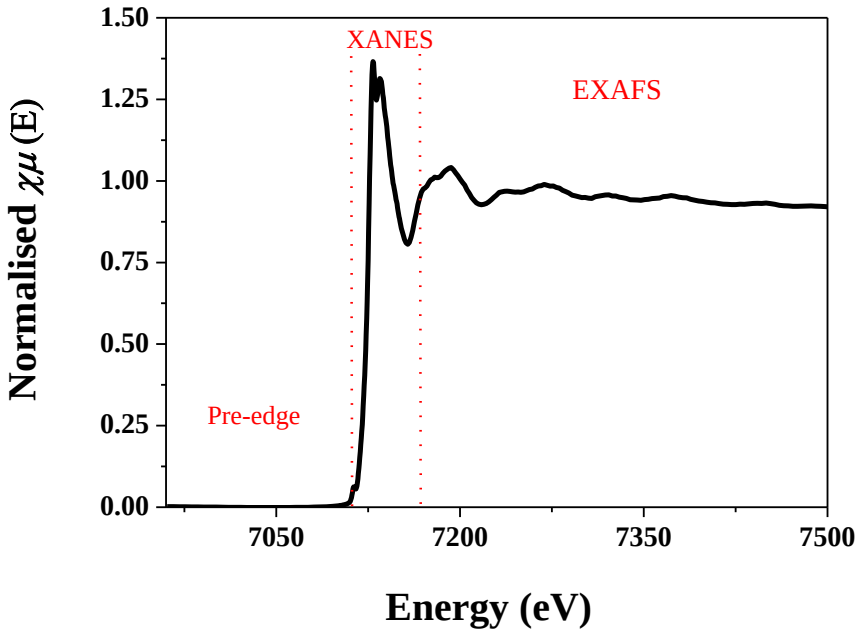

Figure 3.8: XAFS spectrum, where the pre-edge, XANES and EXAFS regions are identified.

XANES spectrum is mainly used to give information about the oxidation state and neighbouring coordinates of the absorbing atom [30,31].

EXAFS is used to gain information about the distances and the neighbouring species of the absorbing atom [30, 31].

From spectra of both the XANES and EXAFS, the data are generated by taking unknown data and fitting them to linear combinations of known (standard) data. It should be mentioned that the XANES and EXAFS measurements are more sensitive to the presence of secondary phases than XRD measurements [29, 31].

3.6 OPTICAL AND MAGNETO-OPTIC MEASUREMENTS

This section discusses two techniques: absorption spectroscopy and MCD spectroscopy. The purpose of using these techniques is to provide a better understanding of the electronic structure through the absorption spectra.

3.6.1 ABSORPTION SPECTROSCOPY

This technique is used for the investigation of optical properties of our samples in the energy range of 1.7 to 4.5 eV. This includes the measurements of transmission and reflection spectra. The data of these measurements are then used to obtain the absorption data which are then used to determine the band gap of the materials studied. Determination of the band gap from absorption data will be discussed in more details in the following sections.

3.6.1.1 Background Theory

The incidence of light on a solid material results in the occurrence of a number of optical phenomena: transmission, reflection, absorption and scattering. The transmission and reflection, for instance, can be described by their coefficients *T* and *R*, respectively. The transmission is defined as the ratio of transmitted light to the total

incident light. Similarly, the reflection is defined as the ratio of the reflected light to the total incident light. As energy is conserved in the process, and assuming there is no scattering or absorption, the combination of *R* and *T* results in the following expression [34]:

$$T + R = 1 \qquad (3.9).$$

However, when the light passes through a sample of thickness, *t*, the film strongly absorbs some of the incident light. This assumes that the multiple reflections from the film and the substrate are negligible. Hence, the transmission and reflection are related by the expression:

$$T = (1\text{-}R)^2 \, e^{-\alpha t} \qquad (3.10)$$

where α is the absorption coefficient.

Once the transmission and reflection data are obtained, and the film thickness is known, then the absorption coefficient can be calculated using the above-mentioned relationship [34].

In a vertical transition, i.e. a direct band gap, the absorption coefficient is proportional to the density of states that can participate in the absorption process, this is given by:

$$(\alpha h\nu)^2 \propto h\nu - E_g \qquad (3.11)$$

where ν is the frequency of the photon and E_g is the band gap energy. This equation is derived from the equation: $\alpha h\nu = A\,(h\nu - E_g)^{1/n}$, where *n* depends on the nature of transition. In our experiment, *n* is equal to 2 because we are interested in measuring the direct transitions.

In order to determine the energy band gap, $(\alpha h\nu)^2$ is plotted as a function of photon energy ($h\nu$), where the band gap is obtained from the point at which the

extrapolated line of the absorption data goes to zero and intersects with the horizontal axis of the photon energy; this is known as Tauc plot [3, 23, 34].

3.6.1.2 Experimental Setup

A conventional absorption spectroscopy setup is based on the equation (3.10), where an excitation by electromagnetic radiation is used to measure the transmitted and reflected light intensities. Thus, the absorption can be derived directly from the transmission and reflection data.

In this system, the configuration can be changed between the transmission and reflection geometries merely by changing the positions of the sample holder and the photomultiplier tube (PMT) detector, as in Figure 3.9.

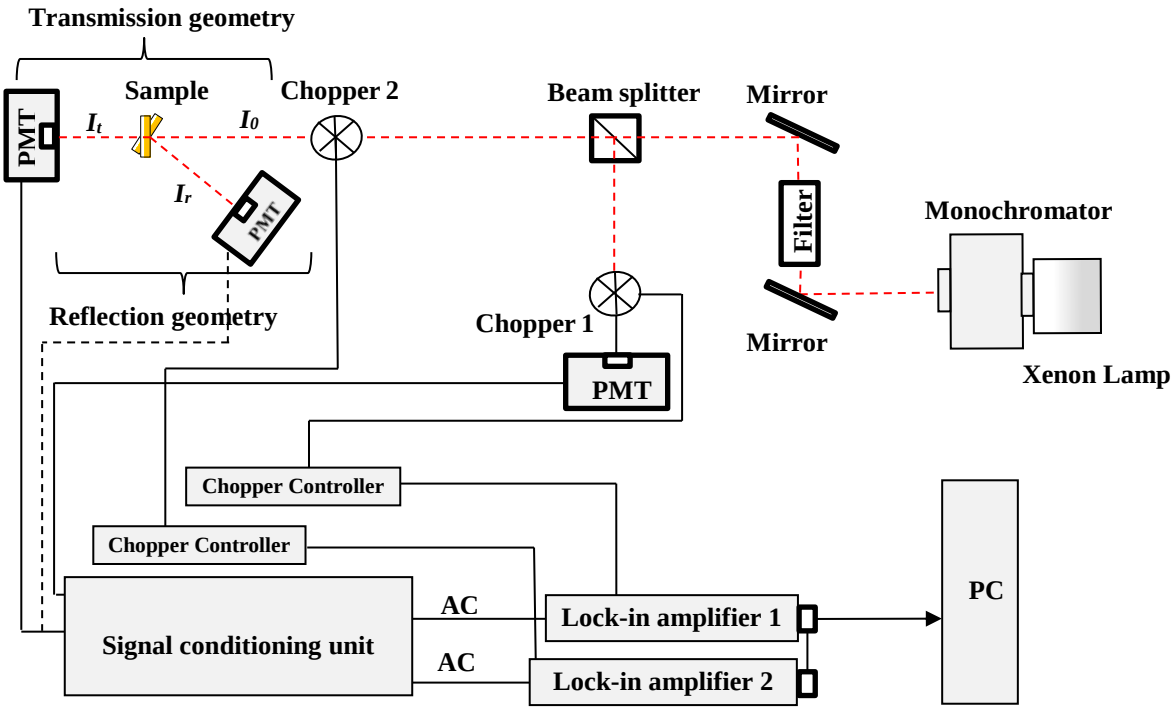

Figure 3.9: Schematic diagram of the absorption spectroscopy system. Adapted from M. S. Alqahtani PhD thesis [35].

A Xenon lamp is used as the light source; covering the spectral range from ~ 830 to 275 nm (~ 1.5 to 4.5 eV). The light beam passes through a *SpectraPro*-275 spectrometer to produce high-resolution spectra using a 1200 line/mm grating that covers the wavelength range between 190 and 1100 nm [23, 35].

After the beam leaves the spectrometer, a bandpass filter is used to remove the unwanted wavelengths. The beam then is directed onto a beam-splitter; generating a sample beam and a reference beam. These are then passed through optical choppers. The reference beam is chopped at a frequency of 370 Hz, whereas the sample beam is chopped at a frequency of 310 Hz. These two frequencies were chosen as they were not multiples of the mains frequency, so as to minimise any interference between the two signals. The aim of using the optical choppers is to minimise the noise effect and improve the signal-to-noise ratio.

The reference beam is recorded by a PMT detector, whereas the sample beam passes through the sample and is recorded by another PMT detector. The difference between the two light intensities is then calculated and converted into an electrical signal. This is then sent to a signal conditioning unit in order to be amplified and split into AC and DC components. The AC signals are amplified and recorded using two signal recovery lock-in amplifier; one of them is used to measure the intensity I_0 which represent the intensity reference of the incident light, whereas the other lock-in amplifier is used to either record the intensity, I_t, or the intensity, I_r, that represent the transmitted and reflected light, respectively. In addition, there is a set of mirrors and lenses that allows as much light as possible to be focused on the sample [35].

An example of the absorption spectrum as a function of photon energy for a 5% Fe_2O_3-doped In_2O_3 film grown on a sapphire substrate is illustrated in Figure 3.10, where the band gap energy, E_g, is estimated to be around 3.75 ± 0.01 eV.

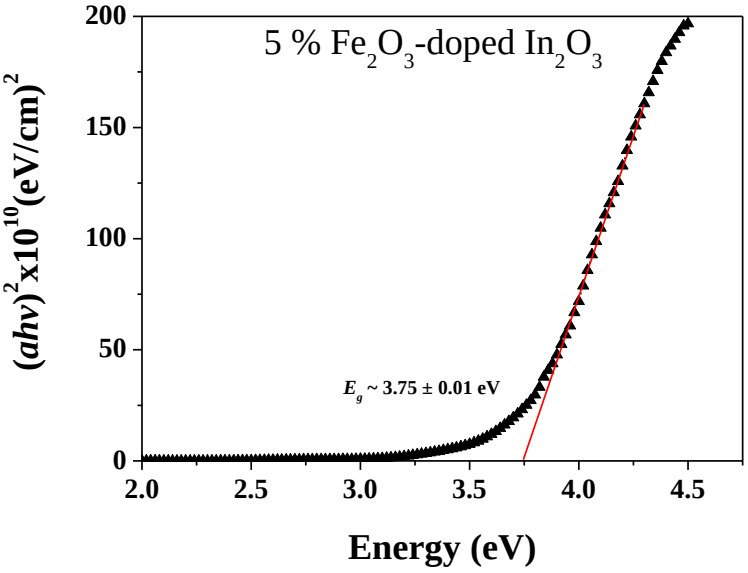

Figure 3.10: Absorption spectrum of 5% Fe_2O_3-doped In_2O_3 film grown on a sapphire substrate.

The error in band gap values are calculated using the standard deviation of the mean of at least four readings; these are based on the number of points that are included in the extrapolated line. For example, if we have four readings taken from four extrapolated lines: E_g1, E_g2, E_g3, and E_g4 equal to 3.76, 3.76, 3.75 and 3.74, respectively, then the error in the band gap is ~ 0.01 eV.

3.6.2 MAGNETIC CIRCULAR DICHROISM SPECTROSCOPY (MCD)

MCD is one of the most sensitive techniques for the study of the effect that arises from the interaction between light and a magnetic material. This is obtained by measuring the properties of a circularly polarised light beam transmitted through the material [11, 36].

3.6.2.1 Background Theory

The propagation of a beam of light through a transparent medium is expressed by the refractive index, *n*. Hence, the refractive index of a medium is defined as the

ratio of the velocity of light in *vacuo*, *c*, to the velocity of light in the medium, *v*, as follows:

$$n = \frac{c}{v} \tag{3.12}$$

However, when light passes through an absorbing material, then the refractive index becomes a complex, $\tilde{n}$, which is given by:

$$\tilde{n} = n + i\kappa \tag{3.13}$$

where *n* is the real part and κ is the imaginary part, the latter being known as the extinction coefficient.

There is a relationship between κ and the absorption coefficient. This relationship can be derived from the electric field, *E*, of a wave propagating through a medium in the *z* direction of the light, as follows:

$$E(z, t) = E_0 \, \mathrm{e}^{\,\mathrm{i}(kz - \omega t)} \tag{3.14}$$

where k is the wavenumber of the light and ω is the angular frequency, these are then related to the refractive index through the equation:

$$k = \frac{\omega \tilde{n}}{c} = (n + i\kappa)\frac{\omega}{c} \tag{3.15}$$

By substituting this equation into the equation (3.14), it can be deduced that the wave decays exponentially in the medium. Then, the optical absorption coefficient previously defined in the equation (3.10) is given by:

$$\alpha = \frac{2\kappa\omega}{c} = \frac{4\pi\kappa}{\lambda} \tag{3.16}$$

where λ is the wavelength of the light in *vacuo* [34].

Linearly polarised light consists of equal parts of left circularly polarised light (LCP) and right circularly polarised light (RCP), as shown in Figure 3.11 (a). Taking into account that these two states pass through a magnetic medium, the equation (3.13) is then rewritten as:

$$\tilde{n}_{\pm} = n_{\pm} + i\kappa_{\pm} \tag{3.17}$$

where the negative term is the LCP component, and the positive term is the RCP component [11, 37, 38].

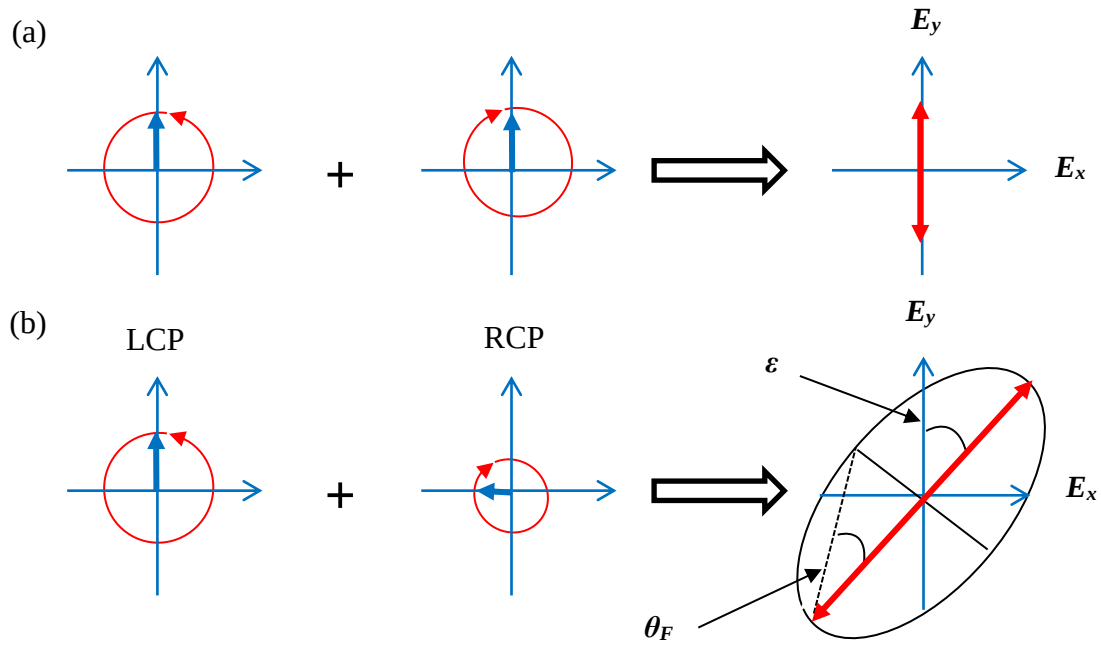

Figure 3.11: (a) Linearly polarised light made up of equal parts of LCP and RCP. (b) If these are unequal after being incident upon a sample in a magnetic field, the transmitted or reflected light will be elliptically polarised and rotated. Adapted from A. J. Behan PhD thesis [11].

The magneto-optic (MO) effect can be seen when the LCP and RCP parts are recombined after leaving the magnetic medium. This is because the LCP and RCP are absorbed differently, since their refractive indices are not equal ($\tilde{n}_{-} \neq \tilde{n}_{+}$). This results in relative changes in the phase and amplitude between the LCP and the RCP light, this is illustrated in Figure 3.11 (b). The rotation of angle θ and the change in the light intensity cause the light to be elliptically polarised [11]. In transmission, the phase lag and attenuation are different from left and right circularly polarised beams, so that they

combine to give elliptically polarised light. The ellipticity and rotation of CP light results in the MO effects of the Faraday effect and MCD, respectively [39].

FR effect is the difference in refractive indices between the LCP and RCP components, this is given by:

$$\theta_{\mathrm{F}} = \frac{\omega l}{2c}(\Delta n) = \frac{\omega l}{2c}\,(n_{+} - n_{-}) \tag{3.18}$$

The difference between the extinction coefficients κ_{-} and κ_{+} gives rise to the LCP and RCP light to be differently absorbed at a frequency ω, where MCD is given:

$$\mathrm{MCD} = \frac{\omega l}{2c}(\Delta \kappa) = \frac{\omega l}{2c}\,(\kappa_{+} - \kappa_{-}) \tag{3.19}$$

Since the MCD is dependent on transitions at ω, it is non-zero if the medium is absorbing [11]. This makes it a very useful method to determine the structural magnetic state of the absorbing material. For this reason, the focus here will be on the MCD measurements [11, 35, 36].

Both Faraday rotation and MCD depend linearly on thickness, they are given in radians and they are dimensionless. However, the apparatus measures the total Faraday rotation and MCD where it is useful to define the Faraday oration per unit thickness and MCD per unit thickness. Hence, in the observed data the thickness in the equations (3.18) and (3.19) are moved down to get Faraday rotation and MCD in degrees per centimetre.

3.6.2.2 Experimental Setup

The setup for measuring the MO effects is based upon the Sato method using Faraday geometry [41], as shown in Figure 3.12. The system is configured to simultaneously obtain measurements of the MCD and Faraday rotation of magnetic materials. In addition, using this method allows one to perform the MO measurements at different wavelengths across a wide region of the spectrum.

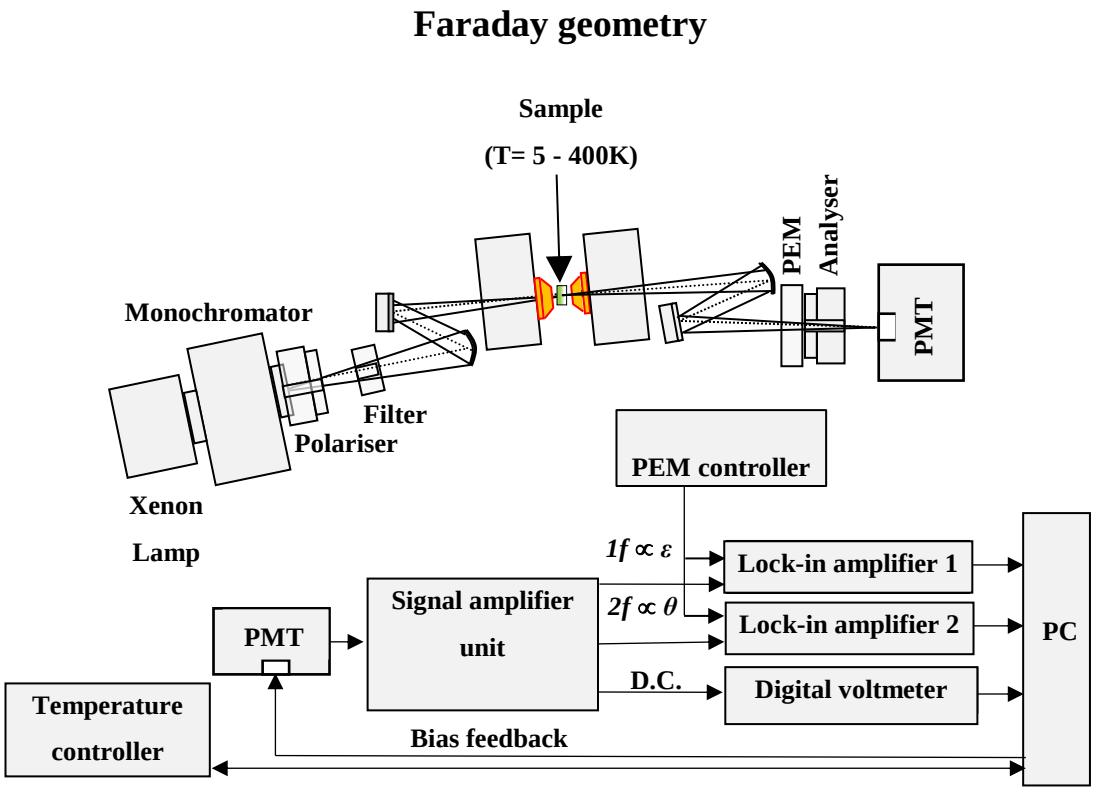

Figure 3.12: Schematic diagram of magneto-optics setup in Faraday geometry. Adapted from A. J. Behan PhD thesis [11].

The sample is mounted on a sample holder which has an aperture diameter of about 3 mm to allow light to pass through it. In the case of RT measurements, the sample is placed directly between the poles of an electromagnet. This allows a magnetic field of up to 18000 Oe to be applied perpendicular to the sample plane. When the measurement is performed at low temperature, the sample is positioned in a cryostat. In this configuration, however, the electromagnetic poles need to be moved slightly further apart in order to accommodate the cryostat. This, in turn, results in decreasing the value of the magnetic field to ~ 10000 Oe.

The setup uses a 150 watt Xenon lamp that covers the spectral range from 1.5 to 4.5 eV. The light is aligned to pass through a SpectraPro-275 spectrometer in order to generate monochromatic light. Before the light beam passes through the sample, it must be plane polarised; this is achieved using a UV prism polariser.

At the sample, the light is focused to the same size of the aperture in the sample holder by using a series of mirrors in order to transmit as much light as possible through the sample. The positions of the mirrors need to be frequently optimised in order to ensure that the maximum amount of light passes through the sample. This is an important step as any errors in the alignment will cause some of the light beam to be scattered by the poles, which directly affects the sensitivity of the measurement.

The polarised lighted is then transmitted through the sample onto a photo-elastic modulator (PEM). This generates a modulation signal that is proportional to the rotation and ellipticity; this allows them to be measured simultaneously.

The PEM working principle is based on the photo-elastic effect, where a sample exhibits birefringence when exposed to a stress. The device consists of a birefringent crystal of fused silica mounted on a piezoelectric transducer (vibrator) that oscillates at a certain resonant frequency.

Hence, any stress applied to the piezoelectric transducer causes the fused silica to become birefringent, inducing a periodic retardation shift to one of the two elliptical polarised components of the transmitted beam. This periodic retardation is parallel to the vibration direction and is given by $\delta = \delta_0 \sin(2\pi ft)$, where δ_0 and f represent the amplitude of the retardation and the modulation frequency, respectively. The vibration direction of the birefringent crystal is set at 45° with respect to the first polariser.

After the light leaves the PEM, it passes through an analyser before it is focused onto a PMT detector. If the sample has a circular polarisation and MCD due to its magnetism, the transmitted light has components of $2f$ and f due to the oscillations in the light intensity. In this way, ellipticity and Faraday rotation can be measured by detecting the f and $2f$ components, respectively. If, however, the sample shows no MO effect, the light intensity at the detector will remain constant.

The PMT will then convert the light intensity into an electrical signal. After that, the signal is transferred to an amplifier unit, where it is amplified and split into AC and DC components. The DC component is measured using a *Keithley* voltmeter, and this signal is kept constant in order to be used as a reference intensity, I_0. The AC measurements are taken using two lock-in amplifiers to obtain the intensities I_f and I_{2f} that represent the MCD and Faraday rotation, respectively.

MCD and Faraday rotation can be obtained through the measurements of the above three intensities. Based on Sato theory, these intensities are given by:

$$I_1(0) = I_0 T\{1 + J_0(\delta_0)\sin(\Delta\theta + 2\phi)\} \tag{3.20}$$

$$I_2(f) = I_0 \Delta T J_1(\delta_0) \tag{3.21}$$

$$I_3(2f) = 2I_0 T J_2(\delta_0)\sin(\Delta\theta + 2\phi) \tag{3.22}$$

$$T = \frac{1}{2}\left(t_+^2 + t_-^2\right) \tag{3.23}$$

$$\Delta T = \left(t_+^2 - t_-^2\right) \tag{3.24}$$

where I_0 is the constant intensity, ϕ is the analyser angle, $\Delta\theta$ represents the difference of rotation for the LCP and RCP components, $t_\pm$ are the Fresnel coefficients that describe the LCP and RCP components of the transmitted light. The J_0, J_1 and J_2 are respectively the zeroth-, first-, and second-order Bessel functions.

The Bessel functions are used to determine the retardation value that is set by the PEM, which was found to be 0.383, where the J_0 is zero the J_1 and J_2 are near their maxima. This indicates that, when the retardation is set to the value of 0.383, the MO sensitivity is at its maximum while being insensitive to fluctuations in light intensity [42].

The MCD, ε, and Faraday rotation, θ_F, can then be related to the previous intensities according to the Sato method as follows:

$$\varepsilon = \frac{1}{4}(\Delta T/T) \tag{3.25}$$

$$\theta_F = -\frac{1}{2}\Delta\theta \tag{3.26}.$$

The values of $\Delta T/T$ and $\Delta\theta$ can be measured experimentally since the ratios of (I_2/I_1) and (I_3/I_1) are related to the MCD and Faraday rotation, respectively. By setting $\phi = 0$, and when $J_0 = 0$ and since $\Delta\theta << 1$, the MCD and Faraday rotation are then given by:

$$\varepsilon \approx \frac{I_2(f)}{I_1(0)} = A\frac{J_1(\delta_0)\Delta T/T}{1+J_0(\delta_0)\sin(\Delta\theta+2\phi)} = AJ_1(\delta_0)\frac{\Delta T}{T} \tag{3.27}$$

$$\theta_F \approx \frac{I_3(2f)}{I_1(0)} = B\frac{2J_2(\delta_0)\sin(\Delta\theta+2\phi)}{1+J_0(\delta_0)\sin(\Delta\theta+2\phi)} = BJ_2(\delta_0)2\Delta\theta \tag{3.28}$$

where A and B, in the above expressions, are calibration factors [41].

The components of the MCD system are connected to a PC and run by LabVIEW® software. An example of room temperature MCD measurement of a 5% Fe_2O_3-doped In_2O_3 film deposited on a sapphire substrate is illustrated in Figure 3.13.

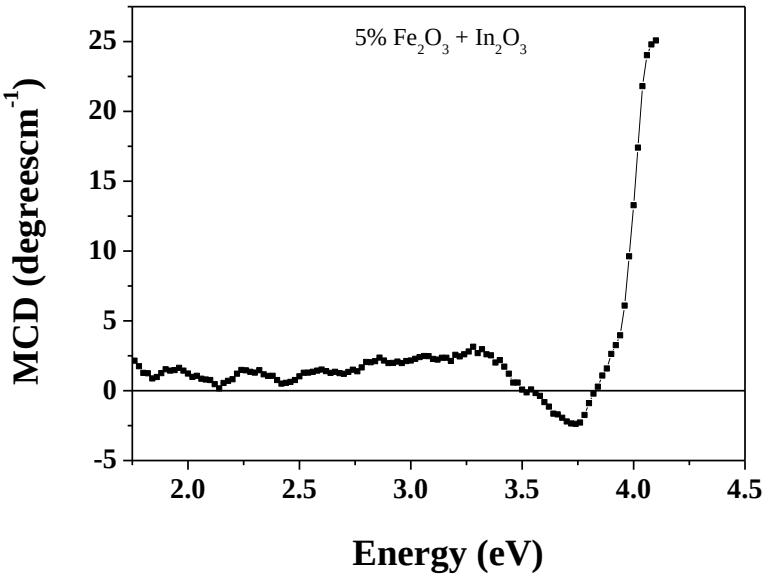

Figure 3.13: MCD measurements of 5% Fe_2O_3 doped In_2O_3 film deposited deposited on a sapphire substrate.

3.7 REFERENCES

1. B. R. Pamplin, *Molecular Beam Epitaxy*. (Pergamon Press, Oxford, 1980).
2. B. Chapman, *Glow Discharge Processes: Sputtering and Plasma Etching* (John Wiley & Sons, New York, 1980).
3. Q. Feng, *Magnetic and Magneto-Optical Properties of Magnetic Oxide Thin Films*. PhD thesis, University of Sheffield, 2013.
4. A. Carter, W. Chang, S. Qadri, J. Horwitz, R. Leuchtner and D. Chrisey, Journal of Materials Research **13** (06), 1418-1421 (1998).
5. J. F. Lawler, J. M. D. Coey, J. G. Lunney and V. Skumryev, Journal of Physics: Condensed Matter **8** (49), 10737 (1996).
6. P. Sharma, A. Gupta, K. Rao, F. J. Owens, R. Sharma, R. Ahuja, J. O. Guillen, B. Johansson and G. Gehring, Nature materials **2** (10), 673-677 (2003).
7. A. K. Pradhan, K. Zhang, S. Mohanty, J. Dadson, D. Hunter, J. Zhang, D. J. Sellmyer, U. Roy, Y. Cui and A. Burger, Applied Physics Letters **86** (15), 152511 (2005).
8. M. N. Ashfold, F. Claeyssens, G. M. Fuge and S. J. Henley, Chemical Society Reviews **33** (1), 23-31 (2004).
9. D. Lichtenwalner, O. Auciello, R. Dat and A. Kingon, Journal of Applied Physics **74** (12), 7497-7505 (1993).
10. X. Chen, S. Xiong, Z. Sha and Z. Liu, Applied Surface Science **115** (3), 279-284 (1997).
11. A. J. Behan, *Characterisation of Doped ZnO Thin Films for Spintronic Applications*. PhD thesis, University of Sheffield, 2008.

12. R. Beal, *Morphology and Efficiency of Polymer: Fullerene Solar Cells*. PhD thesis, University of Oxford, 2010.

13. M. Ziese, S. Sena and H. J. Blythe, Journal of Magnetism and Magnetic Materials **202** (2), 292-300 (1999).

14. J. Clarke, *Superconductor applications : SQUIDs and Machines*, edited by Brian B. Schwartz and Simon Foner. (Plenum Press, New York, 1977).

15. J. Clarke, Proceedings of the IEEE **77** (8), 1208-1223 (1989).

16. A. Bruno, Brazilian Journal of Physics **31** (4), 587-596 (2001).

17. R. Fagaly, Review of Scientific Instruments **77** (10), 101101 (2006).

18. A. J. Behan, A. Mokhtari, H. J. Blythe, M. Ziese, A. M. Fox and G. A. Gehring, Journal of Physics: Condensed Matter **21** (34), 346001 (2009).

19. A. Zelenakova, J. Kovac and V. Zelenak, Acta Physica Polonica-Series A General Physics **115** (1), 357 (2009).

20. C. P. Bean and J. D. Livingston, Journal of Applied Physics **30** (4), S120-S129 (1959).

21. D. K. Bowen and B. K. Tanner, *High Resolution X-Ray Diffractometry And Topography*. (Taylor and Francis Ltd., London, 2005).

22. C. Kittel, *Introduction to Solid State Physics*. (John Wiley & Sons, New York, 2004).

23. S. P. Sena, *An Investigation of some Magnetic Oxides grown by Pulsed Laser Deposition*. PhD thesis, University of Shefield, 1998.

24. S. K. Mahadeva, *Magnetism in Band Gap Engineered Sputtered $Mg_xZn_{(1-x)}O$ Thin Films*. PhD thesis, KTH Royal Institute of Technology, 2013.

25. A. Riazanova, *Direct Nanoprototyping of Functional Materials via Focused Electron Beam*. PhD thesis, KTH Royal Institute of Technology, 2013.

26. K. Edinger, J. Melngailis and J. Orloff, Journal of Vacuum Science & Technology B: Microelectronics and Nanometer Structures Processing, Measurement, and Phenomena **16** (6), 3311-3314 (1998).

27. R. Wirth, Chemical Geology **261** (3–4), 217-229 (2009).

28. G. Stachowiak and A. W. Batchelor, *Experimental Methods in Tribology*. (Elsevier Science, Oxford, 2004).

29. E. Alp, S. Mini and M. Ramanathan, LEGIBILITY NOTICE **5** (5), 25 (1990).

30. Y. An, Y. Xing, F. Pan, Z. Wu and J. Liu, Physical Chemistry Chemical Physics **18** (19), 13701-13709 (2016).

31. M. Newville, Reviews in Mineralogy and Geochemistry **78** (1), 33-74 (2014).

32. D. C. Koningsberger and R. Prins, *X-Ray Absorption: Principles, Applications, Techniques of EXAFS, SEXAFS and XANES*. (John Wiley & Sons, New York, 1988).

33. S. Wang, Y. An, D. Feng, Z. Wu and J. Liu, Journal of Applied Physics **113** (15), 153901 (2013).

34. A. M. Fox, *Optical Properties of Solids*, 2nd ed. (Oxford University Press, 2010).

35. M. S. Alqahtani, *Magnetic and Magneto-Optical Properties of Doped Oxides.* PhD thesis, University of Sheffield, 2013.

36. E. Lage, L. Beran, A. U. Quindeau, L. Ohnoutek, M. Kucera, R. Antos, S. R. Sani, G. F. Dionne, M. Veis and C. A. Ross, APL Materials **5** (3), 036104 (2017).

37. B. Brumfield and G. Wysocki, Optics Express **20** (28), 29727-29742 (2012).

38. S. Sugano and N. Kojima, *Magneto-Optics*. (Springer, Berlin, 2000).

39. F. J. Kahn, P. S. Pershan and J. P. Remeika, Physical Review **186** (3), 891-918 (1969).

40. A. M. H. Hakimi, *Magnetism and Spin Transport Studies on Indium Tin Oxide* PhD thesis, University of Cambridge, 2011.

41. K. Sato, Japanese Journal of Applied Physics **20** (12), 2403 (1981).

42. W. P. Van Drent and T. Suzuki, Journal of Magnetism and Magnetic Materials **175** (1), 53-62 (1997).

Chapter 4

$GdMnO_3$ grown on LSAT (100) and (111)

4.1 INTRODUCTION

Multiferroic rare-earth materials have received a large amount of interest due to their potential in spintronic applications since they simultaneously exhibit ferroelectric and magnetic ordering. Investigations into multiferroic materials started in the 1960s [1-6]. However, since 2001, research in this field has received much interest because these materials have been found to have complicated magnetic states and multiferroic properties at low temperatures [3, 4, 8].

An earlier study of GMO thin film on STO substrates was limited by two factors: first, the strong absorption from STO above 3.2 eV prevents optical studies above this energy; and second, STO has a structural phase transition at around 110 K which provides birefringence, making magneto-optic measurements difficult [1]. These disadvantages, however, can be overcome using a LSAT substrate which has an energy gap of 4.9 eV; hence, absorption is much less than for STO and there is no structural transition [10]. LSAT has a slightly smaller lattice constant of 3.868 Å than STO which has a lattice constant of 3.905 Å. This makes LSAT a suitable substrate for growing a wide range of perovskite oxides with a reduced lattice mismatch and a relatively low strain [11, 12].

In this work, epitaxial films of GMO on LSAT (100) and (111) substrates have been investigated and compared with GMO on STO (100) substrate [1]. The different strains and orientation of the films on such substrates give rise to novel effects on the magnetic and optical properties of GMO thin films. The data, which will be presented

later in this chapter, have already been accepted for publication in the Journal of Thin Solid Films.

4.2 LITERATURE REVIEW OF MANGANITES

Rare-earth manganites can be divided into two groups: a hexagonal phase ($P6_3cm$), including (R = Ho, Er, Tm, Yb, Y and Lu) which have a smaller ionic radii (r_R); and an orthorhombic phase (*Pbmn*) with (R = La, Pr, Nd, Sm, Eu, Gd, Tb and Dy) which have larger ionic radii [4, 13, 14]. The boundary between these two groups exists between $DyMnO_3$ and $HoMnO_3$. For those compounds located close to the boundary of the orthorhombic phase, such as $DyMnO_3$ and $TbMnO_3$, there are structural phase transitions which have attracted many researchers [13-15]. Depending on the growth technique used, some hexagonal phase compounds can be formed into metastable orthorhombic phase and *vice versa* [16, 17].

Until recently, it has been rather difficult to control the ferroelectric and ferromagnetic properties of manganites directly. However, these properties can be coupled indirectly in multiferroic materials through strain [18]. The strain effect can be achieved in multiferroic materials when grown as thin films rather than bulk. Thus, manganite thin film fabrication plays a crucial role in achieving multiferroics with novel magnetic properties that can be used to develop multifunctional devices [5, 18].

Manganites exist among a class of materials well known as distorted perovskites. These materials have a general chemical formula of ABX_3, in the form of the cubic structure shown in Figure 4.1, where A and B are cations and X is an anion. In a GMO compound, A, B, and X represent Gd^{3+}, Mn^{3+} and O^{2-}, respectively [19-22]. In the crystal of manganite, the cations and anions generally tend to arrange themselves in a certain way to minimise the electrostatic repulsion effect. Such an arrangement of

ions is highly dependent on the atomic orbitals which, in turn, significantly affect manganite magnetic properties [23].

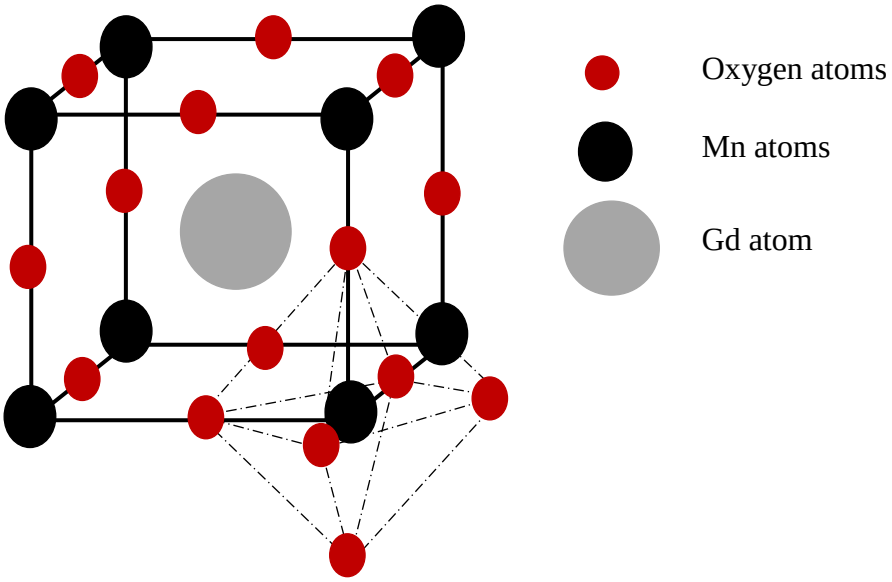

Figure 4.1: ABX_3 cubic perovskite structure, showing the presence of the BX_6 octahedral site.

GMO is an interesting multiferroic candidate; it has an orthorhombic distorted perovskite lattice structure with lattice parameters a = 5.310 Å, b = 5.840 Å, c = 7.430 Å. GMO contains a Gd^{3+} ion which has a large spin moment, S = 7/2 and g = 2, and hence a large value of $g[S(S+1)]^{1/2}$ as well as a Mn^{3+} ion, S = 2, in which the highest d state is singly occupied [7].

Because the ground state of the Mn^{3+} ion has five degenerate partially occupied orbitals, the crystal tends to distort to lift the orbital degeneracy; this is a Jahn-Teller distortion [4, 24]. Since GMO has a structure that is affected by distortion, it is worthwhile discussing the local environment of octahedral crystals in terms of crystal field and Jahn-Teller distortion.

In GMO, the electrostatic forces occur between the d orbitals of the Mn^{3+} ($3d^4$) ions and the p orbitals of the O^{2-} ions. The crystal field is then responsible for breaking

the degeneracy between orbitals. Thus, five different forms of *d* orbitals are divided into two levels: the e_g level has d_{z^2} and $d_{x^2-y^2}$ orbitals, where d_{z^2} points along the *z*- axis; and the t_{2g} level has d_{xy}, d_{xz} and d_{yz} orbitals which point between the *x*-, *y*- and *z*- axes.

In octahedral coordination, this splitting of *d* orbitals results in the e_g levels being higher in energy than the t_{2g} levels, as shown in Figure 4.2 [7].

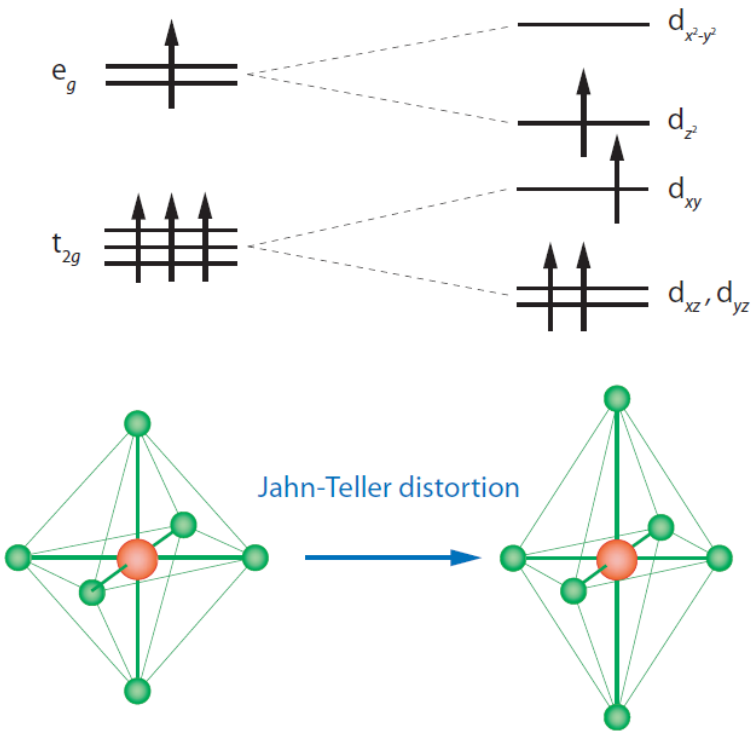

Figure 4.2: Jahn-Teller distortion of a Mn^{3+} ion in the MnO_6 octahedral environment [7].

As a result, there is an energy difference, Δ, between the two sets of the *d* orbitals, as shown in Figure 4.3. This depends on several factors, including the geometry of the octahedron, the repulsion force between like ions, and the effect of Jahn-Teller [25].

According to Hund's first rule, all four spins of the Mn^{3+} ion must be parallel to one another; this results in the lower energy t_{2g} levels being occupied by three electrons and the higher energy e_g level is occupied by the remaining electron.

The distortion of MnO_6 octahedra can occur via expanding the *z*-axis and compressing the *x*- and *y*-axes. Hence, the e_g and t_{2g} levels are split in energy and, as a consequence, the electron in the e_g level occupies the lower energy level [7, 24, 25].

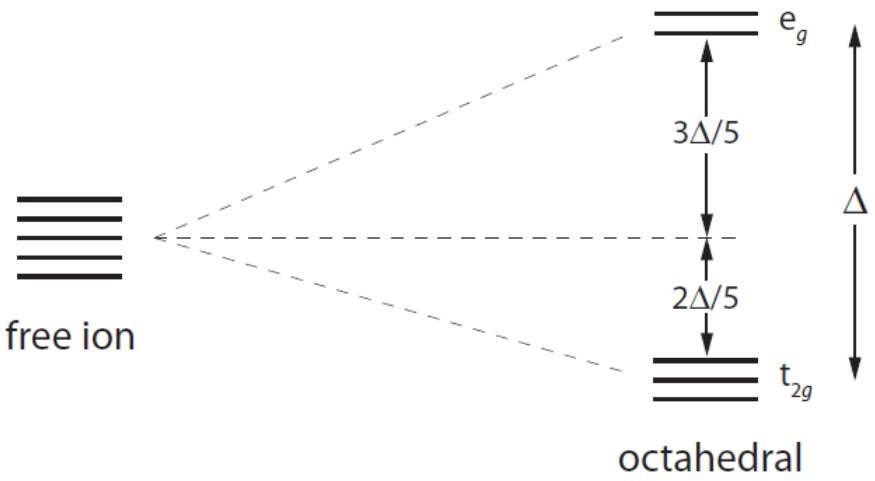

Figure 4.3: *d* orbital splitting in an octahedral manganite [7].

The ionic radius of the Gd^{3+} ion is in the region between La and Dy, which causes its physical properties to be sensitive to strain. In other words, decreasing the ionic radius gives rise to enhance the competition between different types of the magnetic interactions [26, 27].

Bulk crystalline GMO undergoes a phase transition to an incommensurate antiferromagnetic phase (ICAFM) at ~ 42 K and to a canted antiferromagnetic phase (CAFM) at ~ 23 K. A ferroelectric phase is induced at ~ 6.5 K by applying a magnetic field along the *b* axis; the phase boundaries depend on both the magnitude and direction of the magnetic field [26-28].

Multiferroicity in GMO thin films has been reported to be due to strain considering the relationship between the magnetic ordering and ferroelectricity. Since the ferroelectricity in the rare-earth manganites originates from the lattice modulation, then the multiferroic properties can be controlled by modifying the microstructure as a result of strain effect [5, 14]. The magnetic phase diagram of the orthorhombic manganites as a function of Mn-O-Mn bonding angle and ionic radius, as respectively shown in Figures 4.4 (a) and 4.4 (b), were studied by Kimura *et al* [27, 29].

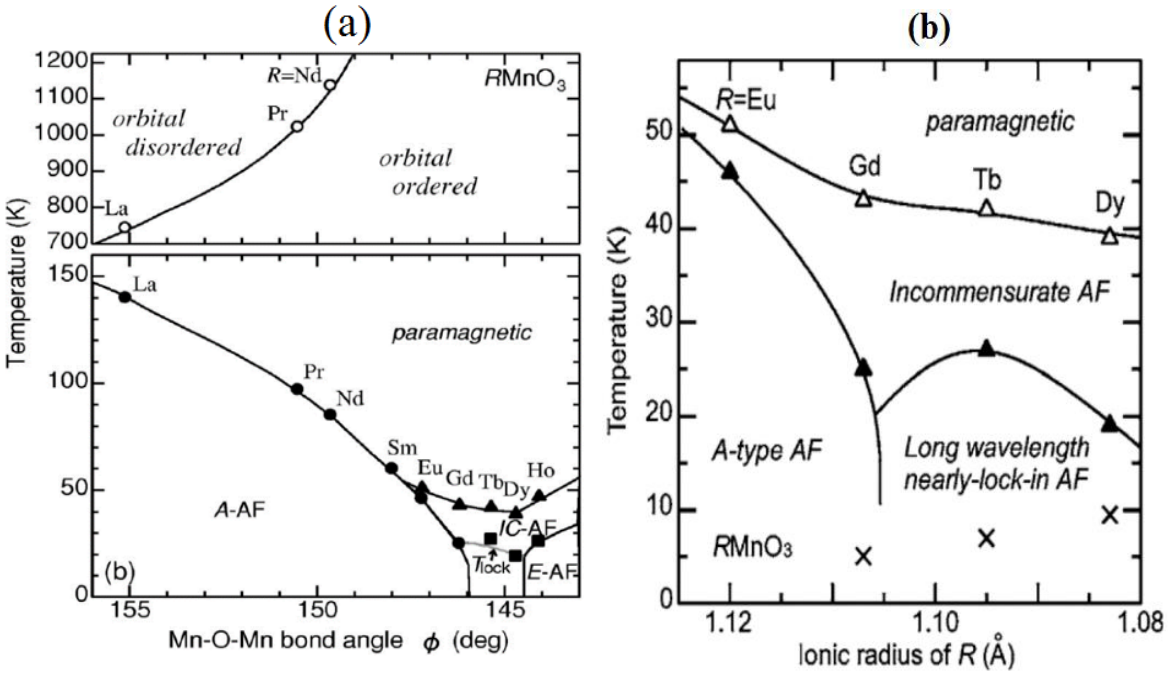

Figure 4.4: The orbital and spin ordering temperatures of $RMnO_3$ as a function of (a) in-plane Mn-O-Mn bond angle [31] and (b) rare earth ionic radius [27, 29].

In manganites, there is a proportional relationship between the Néel temperature and the ionic radius of the rare-earth element where the perovskite structure undergoes some deformation. For example, distortion of MnO_6 octahedron is increased with reduction of the ionic radius, affecting the magnetic interaction. The ionic radii of the lattice sites in a perovskite structure are used to find the tolerance factor. This is an

important factor by which the degree of the deviations from the ideal cubic perovskite structure can be determined [30].

The magnetoelectric transition in GMO can be understood with the help of two crucial aspects:

1. Magnetic frustration which arises from competing super-exchange interactions between successive neighbours. This leads to destabilising ordinary ferromagnetic (FM) and antiferromagnetic (AFM) ordering, giving rise to complex magnetic orders. This phenomenon is responsible for delaying magnetic transitions down to low temperatures [8, 31]. In GMO, the magnetic frustration exists when the Gd cation is situated between four neighbours of Mn^{3+} ions with their spins up, and another four neighbours of Mn^{3+} ions with their spins down. In this case, the Gd spin is said to be frustrated since it has no order due to competing exchange interactions.
2. The spin-lattice coupling that occurs when the oxygen atoms move away from the Mn-Mn bond, resulting in changing the magnetic exchange interaction between the Mn ions [29, 32]. Thus, one of the effects of strain on thin films is changing the microstructure, caused by lattice misfit between the film and substrate [15, 33].

The magnetic phase diagram (H-T) as a function of temperature and magnetic field were obtained for a GMO bulk crystal [19, 28]. It has been reported that the H-T phases are field orientation dependent along the *a*, *b* and *c* axes.

At T_N = 43 K, there is a transition primarily from paramagnetic (PM) to ICAFM phase involving the Mn electrons. Also, the transition from ICAFM phase to a canted A-type antiferromagnetic (cAFM) phase occurs between 16 and 23 K polarising the Gd 4*f* spins. A transition to the ferroelectric phase (FE) takes place at T_C = 12 K by applying a magnetic field along the *b* axis, these transitions are shown in Figure 4.5.

All the previous transitions rely on the intensity and direction of the external applied magnetic field. Thus, it should be mentioned that these transitions occurred with the application of an external magnetic field larger than 20000 Oe [9, 26, 29].

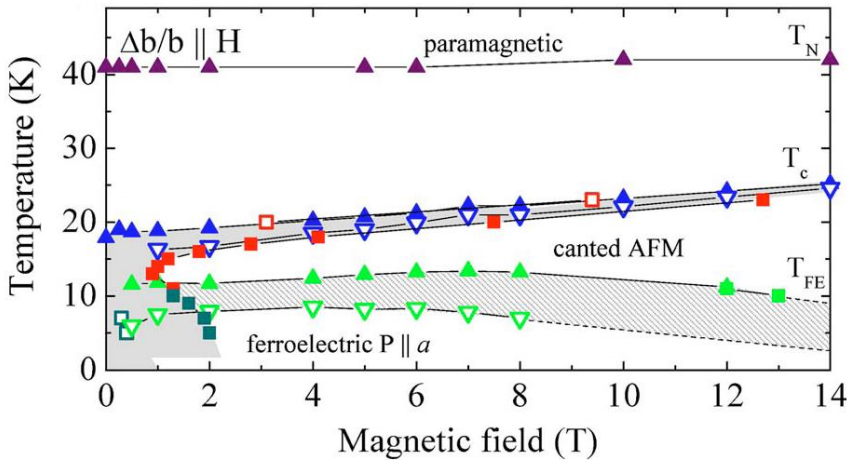

Figure 4.5: Phase diagram of bulk GMO for a magnetic field applied along the *b* axis. Closed and open symbols are obtained by increasing and decreasing temperature or magnetic field, respectively. Shaded areas represent regions of strong hysteresis [9].

In zero-field, however, there is a transition to a canted phase at about 18 K, and generally below 20 K a strong hysteresis can be clearly noticed, indicating that several phases can co-exist. On further cooling, the Gd spins order in a long-range at around 6.5 K which is due to the interaction of the 4*f* spins. Canted Gd spins have a ferromagnetic component that is antiparallel to the ferromagnetic component of the canted Mn spins [28].

Measurements of the ZFC/FC magnetisations of GMO nanoparticles were found to show three magnetic transitions, these are shown in Figure 4.6 [6]. There is a paramagnetic-antiferromagnetic transition that occurs at ~ 44 K; indicating the T_N of the Mn magnetic moments in GMO.

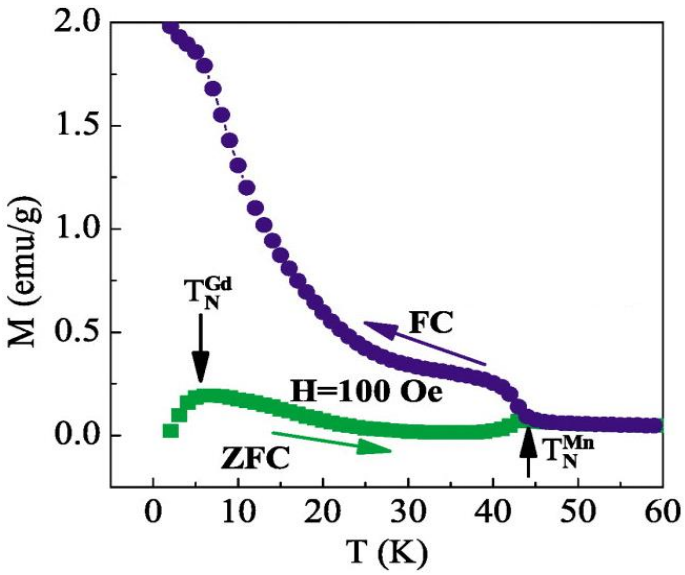

Figure 4.6: ZFC/FC magnetisation of GMO nanoparticles measured in 100 Oe between 2 and 60 K [6].

Decreasing the temperature to ~ 20 K increases magnetisation; this is due to the weak ferromagnetic contribution that arises from the canting Mn magnetic moments and the polarisation of the Gd 4*f* magnetic moments. At 7 K, as a result of the interaction between the Gd magnetic moments, a long-range ferromagnetic order takes place. This is larger than the antiferromagnetic order caused by the canted Mn magnetic moments.

Similarly, it has been reported that the above transitions begin at temperatures of 42 and 39 K for GMO thin films grown on STO and $LaAlO_3$ (LAO) substrates, respectively [34]. This indicates that the strain induced by the substrate on which the GMO is grown plays a significant role in reducing T_N [35].

It has been found that the optical and magnetic data of the GMO thin films differ from those of bulk GMO [24, 36, 37]. The differences have been attributed to the existence of a stress gradient normal to the film surface. Thus, the existing strain may induce a significant change in the Mn–O–Mn bond angle, which has a crucial effect on the balance between the competing ferromagnetic and antiferromagnetic interactions [1, 8]. It is believed that the strain-induced changes in the Mn–O–Mn bond angle give rise to the FM interactions to dominate more compared to the AFM interactions [36].

Figure 4.7 shows the absorption coefficient spectra of a number of RE manganite thin films at room temperature. In general, these spectra exhibit an absorption peak near 2 eV and a higher absorption peak above 3 eV.

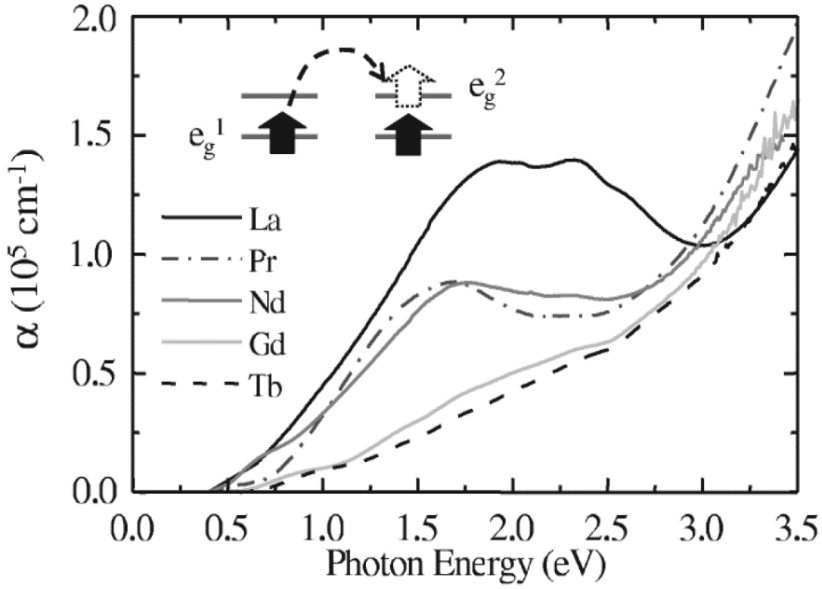

Figure 4.7: Absorption spectra of different $RMnO_3$ thin films measured at room temperature, showing suppressed transition peaks at 2 eV for Gd and Tb elements [8].

The low energy transition around 2 eV is ascribed to the intersite *d-d* charge transfer transition (intersite transition across the Mott gap). This gap arises because of Coulomb energy, occurring when an electron moves from the e_g orbital of an atom into the e_g orbital of another atom. Thus, the hopping energy will be at the expense of repulsion energy, and when the repulsive energy is bigger than the hopping energy, then a Mott gap is created [36]. It can be noted, however, that the 2 eV peak is supressed in the $RMnO_3$ (R = La → Tb) films. This may be due to decreasing the ionic radii that give rise to increasing the Jahn-Teller distortion of the MnO_6 octahedron [8, 36]. On the other hand, the high energy absorption peak around 3 eV is attributed to the charge transfer transition between O 2*p* and Mn 3*d* states [8, 27].

4.3 SAMPLE PREPARATION

The GMO films were grown using RF magnetron sputtering from stoichiometric polycrystalline GMO targets by our collaborators V. Chichkov and N. Andreev from the National University of Science and Technology "MISiS", Russia. Thin films of GMO were grown on LSAT (100) and (111) substrates. The films were grown in a mixture of Ar and O_2 at a pressure of 1-2 mTorr and the substrate temperature was fixed at 650℃. The thickness of each GMO film was 100 nm. The structures of the films were analysed using XRD and found to be grown epitaxially on LSAT (100) and (111) substrates.

4.4 EXPERIMENTAL RESULTS

The magnetic properties of the films were studied using a SQUID magnetometer at room temperature, 300 K, and low temperature, 5 K, to measure the hysteresis loops and the ZFC/FC magnetisation curves. These two types of measurements were made by applying the magnetic field in parallel and perpendicular directions to the plane of the GMO films.

The absorption data were deduced from the transmission and reflection measurements made at room temperature. The films were studied using magneto-optic spectroscopy in Faraday geometry at room temperature and at 10 K using a Xenon lamp over the energy range between 1.5 eV and 3.8 eV [1].

4.4.1 Properties of LSAT (100) and (111) Substrates

LSAT substrate has been used widely because it grows as an untwinned cubic perovskite with lattice parameter a_0= 3.868 Å, which is an excellent lattice match to the manganites. Our substrates were obtained from Materials Technology International

corporation (MTI), both (100) and (111) substrates had thicknesses of 0.5 mm ± 0.05 mm and were oriented to within ± 0.5^0; they were polished on both sides and had surface roughness Ra < 8 Å. This study investigated the optical and magnetic properties of LSAT so that these effects were subtracted from our measurements of GMO films.

LSAT is a substitutionally disordered oxide containing divalent Sr, trivalent La and Al, and pentavalent Ta [24]. The measured transmission of both LSAT substrates at 2 eV is ~ 80 % which is comparable with the value expected from a smooth substrate, $T = \frac{2n}{n^2+1}$ = 0.79 using the refractive index of LSAT, which is 2.02 [20, 40]. In contrast, the transmission at 4.5 eV is ~ 40 % which is considerably less than that for transparent substrate T = 0.74, where the refractive index rises to 2.24. Thus, the loss of transmission at energies above 3.75 eV is clearly due to weak absorption, as shown in Figure 4.8 (a) [10].

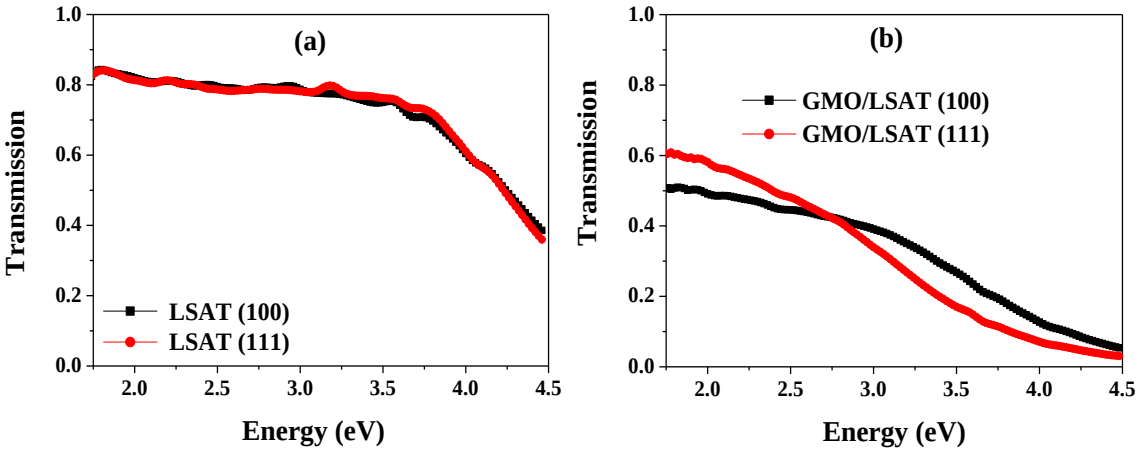

Figure 4.8: Transmission spectra (a) for bare LSAT (100) and (111) and (b) for GMO films on the LSAT (100) and (111) substrates.

These transitions are very weak since the transmission was measured on a substrate that was 0.5 mm thick. There is no difference between the results for the two LSAT substrates. The absorption of the GMO films on LSAT (100) and (111) substrates can be seen from Figure 4.8 (b).

Many disordered oxides have small magnetic moments [41], so we needed to measure the magnetic properties of the substrates carefully so that the results could be subtracted from the measurements taken with the films.

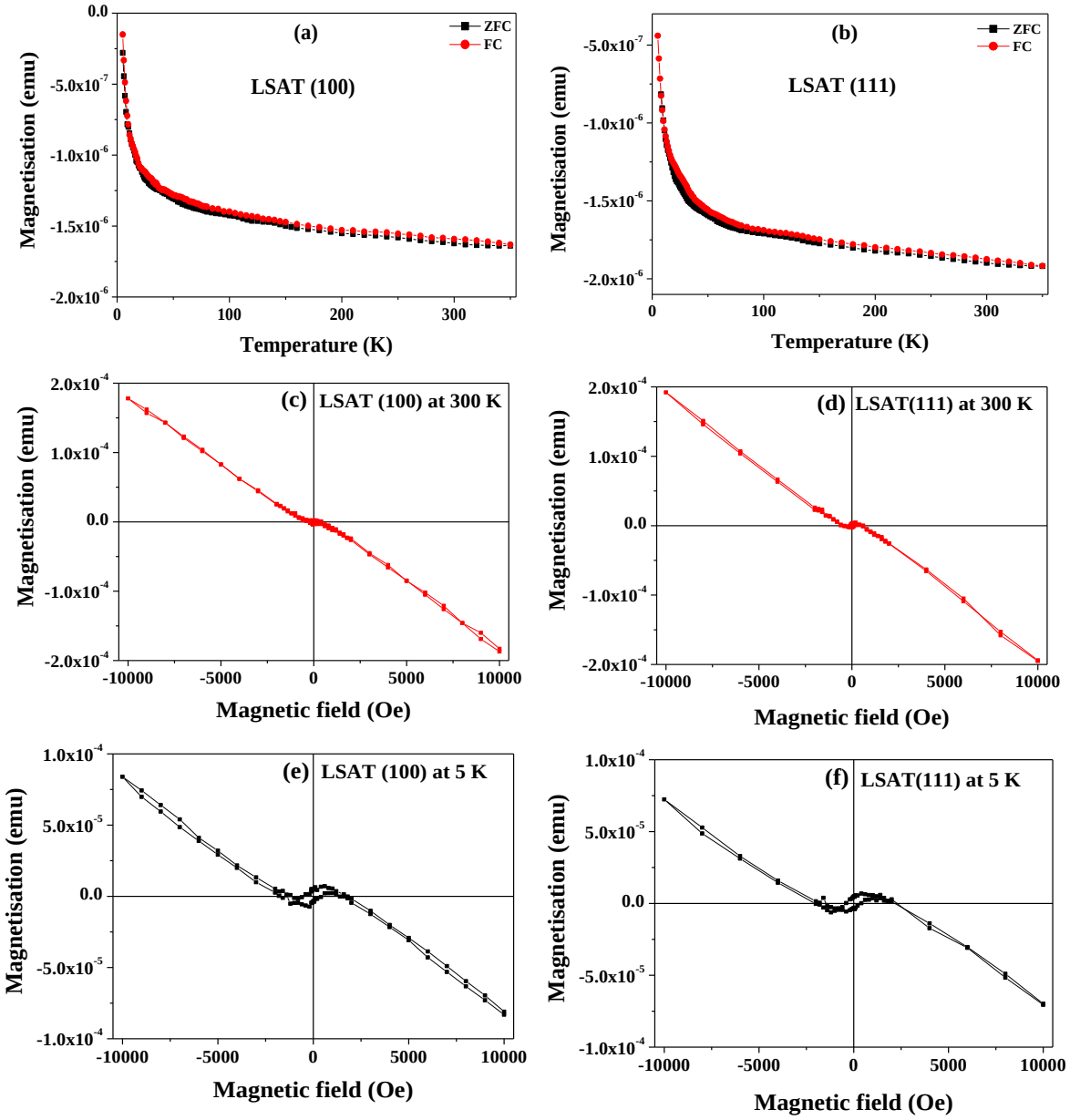

Figure 4.9: (a) and (b) are the ZFC/FC measurements of blank LSAT (100) and (111) substrates, respectively, with the applied magnetic field of 100 Oe, lying in plane. (c) and (d) are the hysteresis loops taken at 300 K for LSAT (100) and LSAT (111), respectively. (e) and (f) are equivalent hysteresis loops taken at a temperature of 5 K.

The expected diamagnetic term dominated in the ZFC/FC magnetisations at high temperatures, $M \sim -1.7\times10^{-6}$ emu and was comparable for both substrates in both orientations. There was a paramagnetic contribution, as shown in Figures 4.9 (a) and 4.9 (b), that dominates at low temperature and depends upon the orientation of the substrate and the direction of the applied magnetic field, being larger for the field perpendicular to the plane of the sample.

M – H loops for LSAT (100) and LSAT (111) substrates, were measured at 300 and 5 K with a magnetic field applied in the parallel and perpendicular directions, showing very small coercive fields for LSAT (111). The measurements taken with the field in plane are shown in Figures 4.9 (c - f). These fields set the limit of what values can be measured for the films. All these magnetic effects are very small and only significant in our study because the substrates were much thicker than the films [28, 41].

4.4.2 Structure of GMO on LSAT (100) and (111) Substrates

The structural properties were investigated using XRD. Detailed measurements were made for the film on LSAT (100) using CuKα radiation. For the GMO film on LSAT (100) substrate, we found two dominant orientations: (a) $(110)_{GMO} \parallel (100)_{LSAT}$; $[001]_{GMO} \parallel [010]_{LSAT;}$ and (b) $(110)_{GMO} \parallel (100)_{LSAT}$, $[001]_{GMO} \parallel [001]_{LSAT}$. Two other less frequent orientations were: (c) $(001)_{GMO} \parallel (100)_{LSAT}$, $[010]_{GMO} \parallel [010]_{LSAT;}$ and (d) $(001)_{GMO} \parallel (100)_{LSAT}$, $[100]_{GMO} \parallel [010]_{LSAT}$. The separation of the (110) planes in structures (a) and (b) needs a small contraction of 1.5% to fit $d_{100}^{LSAT} = 3.868$ Å according to $d_{110}^{GMO} = \left(\left(\frac{1}{a}\right)^2 + \left(\frac{1}{b}\right)^2\right)^{-1/2} = 3.93$ Å, where *a* and *b* are the GMO lattice constants of 5.310 Å and 5.840 Å, respectively. An expansion of 4% and a smaller contraction of 2% occur in plane as the GMO [001] and $[1\bar{1}0]$ axes respectively fit to LSAT [020] or [002] as given in Table 4.1. For cases (c) and (d), the misfit between the planes of GMO

(001) and LSAT (100) forces an expansion of 4% along [001] ($d_{001}^{GMO} = 7.430\,\text{Å}$ and 2 $d_{100}^{LSAT} = 7.736\,\text{Å}$), where the value 7.340 Å is the lattice constant of the GMO *c* axis. There are also contractions in the two in-plane lattice vectors GMO [010] and [100] of 6% and 3%, respectively. Thus, the majority of the film has the plane aligned with the least strains, the results are summarised in Table 4.1.

Table 4.1: The separations between planes and the strains induced along the in-plane axes by the epitaxial growth modes for GMO on LSAT (100) and LSAT (111).

Description	**Spacing**	**Misfit between planes**	**In plane misfit**	**In plane misfit**
GMO plane on LSAT (100)				
(110)	$\left[\left(\frac{1}{a}\right)^2+\left(\frac{1}{b}\right)^2\right]^{-1/2}$	-1.5%	GMO [001] on LSAT [0$\underline{2}$0] 4%	GMO [$1\bar{1}0$] on LSAT [00$\underline{2}$] - 2%
(001)	*c*	4%	GMO [0$\underline{2}$0]on LSAT [0$\underline{3}$0] -0.6%	GMO [$\underline{3}$00]on LSAT [00$\underline{4}$] -3%
GMO Plane on LSAT (111)				
(101)	$\left[\left(\frac{1}{a}\right)^2+\left(\frac{1}{c}\right)^2\right]^{-1/2}$	3%	GMO [010] on LSAT $[1\bar{1}0]$ -6%	GMO $[10\bar{1}]$ on LSAT $[11\bar{2}]$ 4%
(011)	$\left[\left(\frac{1}{b}\right)^2+\left(\frac{1}{c}\right)^2\right]^{-1/2}$	-3%	GMO [100] on LSAT $[1\bar{1}0]$ 3%	GMO $[01\bar{1}]$ on LSAT $[11\bar{2}]$ 0.3%

The crystal structures of LSAT (111) and GMO on LSAT (111) were studied using the XRD Bruker D2 Phaser using CuKα at the University of Sheffield. On the LSAT (111) substrate, the highest peak corresponds to the GMO (202) and GMO (022) reflections lying on the reflection from the (111) substrate as shown in Figure 4.10. The inset of the Figure 4.10 shows the magnified area around 40°.

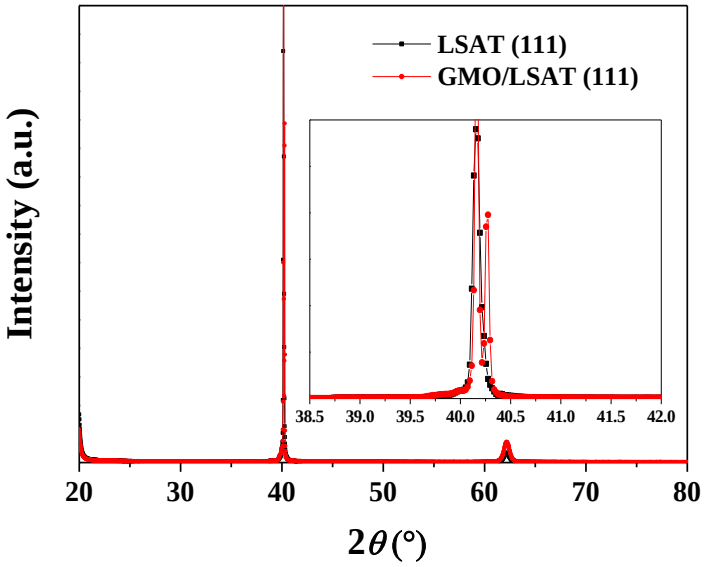

Figure 4.10: Symmetrical spectra of LSAT and GMO on LSAT (111). The inset shows the details of the peak at ~ 40°.

The separations of the (202) and (022) planes are given by; $\frac{1}{2}\left[\left(\frac{1}{a}\right)^2+\left(\frac{1}{c}\right)^2\right]^{-1/2}$ =2.16 Å and $\frac{1}{2}\left[\left(\frac{1}{c}\right)^2+\left(\frac{1}{b}\right)^2\right]^{-1/2}$ = 2.30 Å respectively, which need to be compared with the separation of the LSAT (111) planes of $\frac{a_o}{\sqrt{3}}$ = 2.23 Å; leading to a 3% expansion and a 3% contraction respectively, as can be seen in Table 4.1. The two LSAT lattice vectors lying in plane are LSAT $[1\bar{1}0]$ and LSAT $[11\bar{2}]$ with lengths $\sqrt{2}a_0$ = 5.47 Å and $\sqrt{6}a_0$ = 9.47 Å, respectively.

The GMO lattice vectors are [010] and $[10\bar{1}]$ with lengths 5.84 Å and 9.13 Å respectively, relevant for the GMO (101) plane; and [100] and $[01\bar{1}]$ with lengths 5.31 Å and 9.13 Å respectively, relevant for GMO (011). The best fits for the GMO (101) plane are GMO [010] on LSAT $[1\bar{1}0]$ and GMO $[10\bar{1}]$on LSAT $[11\bar{2}]$; and those for the GMO (011) plane are GMO [100] on LSAT $[1\bar{1}0]$ and GMO $[01\bar{1}]$ on LSAT $[11\bar{2}]$. The strains, defined as: $\frac{d_{LSAT} - d_{GMO}}{d_{GMO}} \times 100$, are given in Table 4.1.

4.4.3 Magnetic Properties

The magnetism of the GMO films was studied and the results compared with those obtained for bulk GMO and GMO/STO thin films to investigate the effects of the epitaxy induced strain. In bulk, there is a strong temperature dependent paramagnetic response along both the *b* and *c* axes and hysteretic magnetisation occurs along the *b* axis [31].

We measured ZFC/FC magnetisations in a magnetic field of 100 Oe with the magnetic field in parallel and perpendicular to the plane of the GMO films on LSAT (100) and (111) substrates as shown in Figures 4.11 (a) and 4.11 (b).

The ZFC/FC plots lie almost on top of each other for all temperatures, but for both films, a larger hysteresis appears for temperatures less than ~ 25 K. The magnetisation in plane is noticeably larger than that perpendicular to the plane for both films. The plots for the GMO film on LSAT (100) show a clear transition at ~ 25 K, however, the transition is more rounded for the GMO film on LSAT (111).

Hysteresis loops were also measured at low temperature, 5 K. The hysteresis loops showed two contributions: a part that varied linearly with the applied magnetic field at fields greater than 2500 Oe; and a part that showed hysteresis with the applied magnetic fields that are less than 2500 Oe. The data are shown in Figures 4.11. (c) and 4.11 (d). The magnetic contributions from the LSAT substrates have been subtracted from all the measurements shown here.

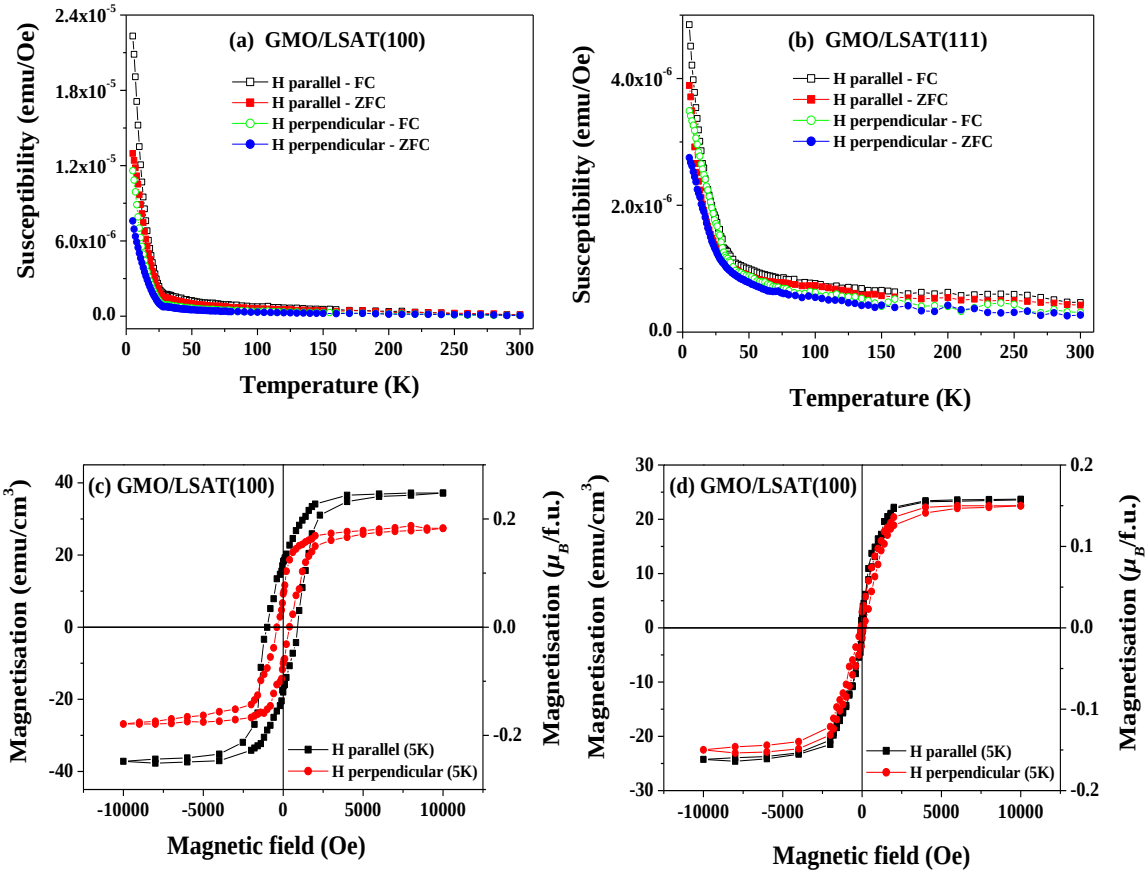

Figure 4.11: The ZFC/FC plots taken in H = 100 Oe for the GMO films on (a) LSAT (100) and (b) (111) substrates; (c) and (d) are the magnetic hysteresis loops taken at 5 K of the GMO films on LSAT (100) and (111) substrates, respectively. In all cases, the magnetic field was applied in parallel and perpendicular directions and the magnetic contributions from all substrates have been subtracted.

The different ordering of the films is seen clearly from the hysteresis loops, found after subtraction of the linear components from the substrates. In the loops for the GMO film on LSAT (100), the magnetisation and hysteresis are greater for the

magnetic field applied in plane. In bulk, the easy direction and the largest moment occur along the *c*-axis [19], and this direction lies in plane for the dominant orientation. The observed magnetisation of 0.26 (μ_B/f.u.) for this film is much lower than that observed for a single crystal, 3.75 (μ_B/f.u.), at 5 K [19, 27]. The coercive fields are 950 Oe and 400 Oe for the GMO film on LSAT (100) measured in parallel and perpendicular magnetic fields, respectively, which compare with the bulk value of 1200 Oe [19, 42]. Hence, the strain due to epitaxy on LSAT (100) leads to a considerable reduction in the magnetisation. This implies that the strains that develop in bulk material as a result of the canting have been suppressed by the epitaxy with the substrate [26].

There is almost no hysteretic behaviour for the Gd spins of the GMO film on LSAT (111) substrate. This is consistent with the antiferromagnetic θ, which will be shown later, observed for this film. Hence, the very considerable distortions described in **section 4.4.2** have caused a qualitative change in the ordering of the Gd spins.

The inverse susceptibilities found from the ZFC plots, as illustrated in Figures 4.12 (a) and 4.12 (b), show two distinct regions in which the Curie law dependence is observed. These regions depend on the substrate and the orientation of the applied field of 100 Oe. In comparison to the GMO films that were grown on STO substrate, similar behaviour was reported; this is shown in Figure 4.12 (c).

In the GMO films on LSAT substrates, a paramagnetic contribution above 30 K arises from Mn as well as Gd ions; this contribution is given by Curie's law $\chi^{high} = \frac{C^{high}}{T + \theta^{high}}$ as seen in bulk for a single crystal and a polycrystalline powder where the measured value of $p_{eff}^2 = g_{Gd}^2 S_{Gd}(S_{Gd}+1) + g_{Mn}^2 S_{Mn}(S_{Mn}+1)$ was close to the free ion value of 87 [1, 19, 42].

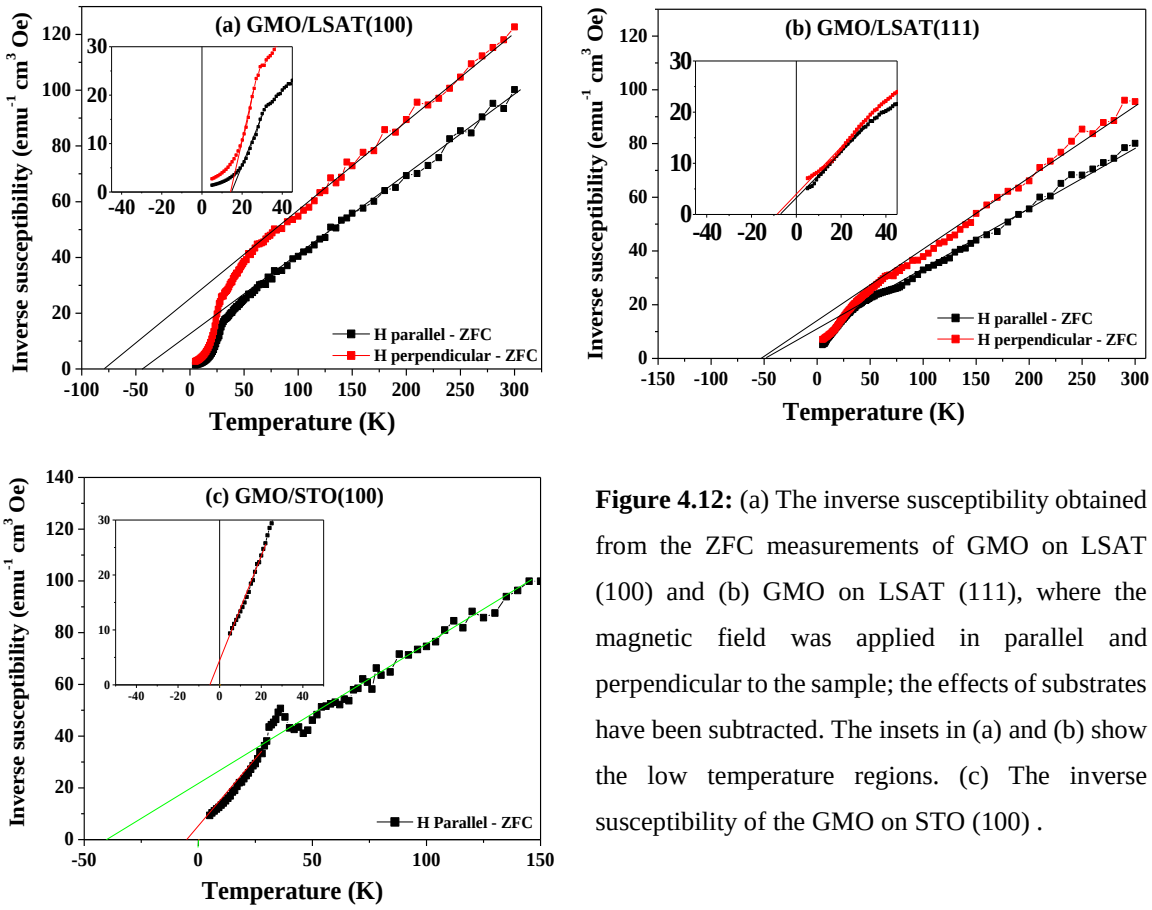

Figure 4.12: (a) The inverse susceptibility obtained from the ZFC measurements of GMO on LSAT (100) and (b) GMO on LSAT (111), where the magnetic field was applied in parallel and perpendicular to the sample; the effects of substrates have been subtracted. The insets in (a) and (b) show the low temperature regions. (c) The inverse susceptibility of the GMO on STO (100) .

There is a second region that is also well described by Curie's law for $8 < T < 30$ K where the Mn spins are canted but the Gd spins are still disordered, $\chi = \frac{C^{low}}{T + \theta^{low}}$, so that $p_{eff}^2 = g_{Gd}^2 S_{Gd}(S_{Gd}+1) \cong 63$. This region is shown in an expanded scale in the insets of Figures 4.12 (a), 4.12 (b) and 4.12 (c).

The measured values of p_{eff}^2 and θ for the GMO films on LSAT (100) and (111) substrates in the high and low temperature regimes are given in Table 4.2 where it is seen that the observed values of p_{eff}^2 for the GMO film on LSAT (100) are close to those expected for free spins; however, those for the GMO film on LSAT (111) are systematically low.

Table 4.2: The measured effective moments and Weiss constants of GMO on LSAT (100), LSAT (111) and STO (100) in the high and low temperature regimes.

Sample	GMO/LSAT(100)		GMO/LSAT(111)		GMO/STO(100)
	H parallel	**H perpendicular**	**H parallel**	**H perpendicular**	**H parallel**
$p^2_{eff\,(high)}$ (Gd+Mn)	84±5	76±5	71±7	65±10	76±10
$p^2_{eff\,(low)}$ (Gd)	68±7	68±7	52±10	46±10	45±10
θ_{high}	42 ± 5	78 ± 5	47 ± 5	51 ± 5	43±5
θ_{low}	-12 ± 2	-11 ± 2	6 ± 2	8± 2	8 ± 2

The values of θ found in the high temperature range are close to ~ 50 K, larger than the 35 K observed in bulk [41]. The ferromagnetic value of θ^{low} for the GMO film on LSAT (100) corresponds to the ordering of the Gd spins observed in bulk at ~ 7 K and appears to be occurring at a slightly higher temperature ~ 11 K. However, different behaviour is seen for the GMO film on LSAT (111) where θ^{low} is positive, implying that the change in the interactions due to the strain causes the Gd spins to order antiferromagnetically.

4.4.4 Optical Properties

Using a LSAT substrate allows measurements over a larger spectral range up to 4.5 eV, compared with 3.2 eV for STO. The absorption spectrum of GMO starts to appear with a small peak the energy of ~ 1.75 eV and rises approximately linearly to ~ 2.5 eV, and then linearly again with an increased slope up to 3.5 eV. The absorption at higher energy is due to the charge transfer transition from O 2*p* to Mn 3*d* [1, 43].

The transmission spectra of blank LSAT (100) and (111), in addition to GMO on LSAT (100) and GMO on LSAT (111), were obtained to determine the effect of the absorption of LSAT substrates on the GMO films, as shown in Figure 4.13.

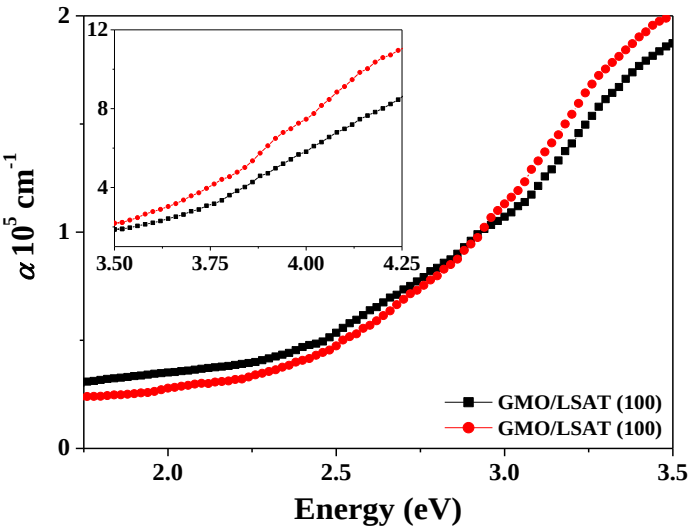

Figure 4.13: Absorption measurements of GMO on LSAT (100) and GMO on LSAT (111) in the range 1.75 < E < 3.5 eV; the inset shows the absorption in the range 3.5 < E < 4.5 eV.

The origin of the absorption peak observed for $RMnO_3$ (R = La – Tb) thin films near 2 eV in the previously presented Figure 4.7 has been debated for a long time. However, it was found that this peak should be attributed to an inter-site transition between the Mn e_g orbitals across the Mott gap [8].

The optical absorption agrees with measurements on bulk GMO because the absorption rises approximately linearly with energy up to E ~ 2.5 eV and then more rapidly at higher energy. The absorption at energy above 3 eV is attributed to the charge transfer transition from O 2*p* to Mn 3*d* states [45, 46].

4.4.5 Magneto-Optical Properties

MCD measurements were taken in Faraday geometry using a Xe lamp and a photoelastic modulator [47, 48]. Results for GMO on LSAT (100) and LSAT (111) ,

measure at 10 and 300 K, are shown in Figure 4.14 (a), where the MCD of the substrate has been subtracted.

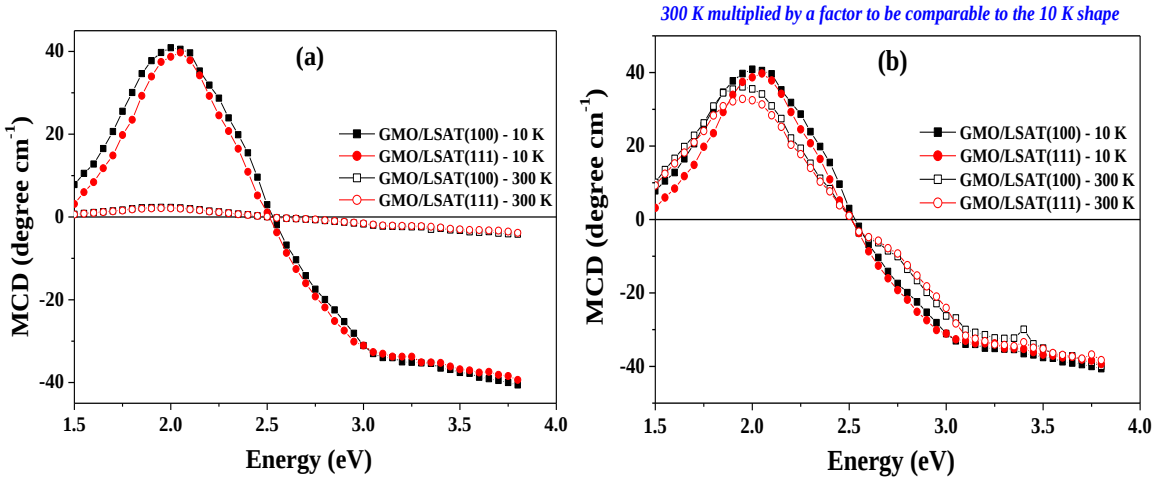

Figure 4.14: (a) MCD spectra of GMO on LSAT (100) and GMO on LSAT (111) at 10 K and 300 K; (b) MCD spectra of GMO on LSAT (100) and GMO on LSAT (111) at 10 K and 300 K where the MCD data at 300 K have been expanded just to be comparable to the 5 K data. The effects of substrates have been subtracted.

We found that the MCD for the two films were very similar in spite of the differences in their magnetic properties. The spectra have two features: the charge transfer transition between Mn *d* states at ~ 2 eV; and the band edge transition from the oxygen *p* band to the Mn *d* states at ~ 3 eV [1, 4, 6, 43].

It can be clearly seen that the MCD is much larger at 10 K where the Mn spins are ordered. In Figure 4.14 (b), we compare the spectrum taken at 10 K with that taken at 300 K, scaled so the curves have a similar magnitude to compare the spectral shapes. This indicates that the main effect is just a change in magnitude due to the magnetic ordering, but that there is a small increase in the MCD magnitude measured at 10 K between 2 and 3 eV, implying that this might be due to a slight increase in the Jahn-Teller splitting at low temperatures.

4.5 SUMMARY AND CONCLUSIONS

The strain of the GMO films due to LSAT (100) and (111) substrates causes substantial differences in the magnetic properties of multiferroic GMO thin films. The magnetic moment obtained in the range of 0.2 μ_B is due to the canted moments of Mn as the magnetic moment of Mn^{3+} ion is 4 μ_B. The canting of the Mn moments is enhanced and a strong easy plane anisotropy is induced by the strain caused by the LSAT (100) that is larger than that induced by STO (100) due to the extra compressive strain in plane along the *b* axis.

Using LSAT (100) and (111) allows us to make measurements over a larger spectral range above 3.25 eV compared to STO (100), because the STO is absorbing more strongly than the LSAT substrates for E > 3.2 eV.

The in-plane compression of the GMO film grown on LSAT (100) strongly enhances the inter-site transition between Mn ions and produces a large enhancement of the MCD around 2 eV relative to the GMO films grown on STO (100). In contrast, the MCD is suppressed for the GMO film grown on LSAT (111). Absorptions at lower energy originate from the Mn (3*d*) electron transition, while the absorption at higher energy is associated with the charge-transfer transitions between O (2*p*) and Mn (3*d*) states. Large changes may be induced in GMO by growing thin epitaxial films on suitably chosen substrates. In particular, a marked enhancement of the saturation magnetisation and the coercive field may be obtained by growing on LSAT (100).

4.6 REFERENCES

1. M. S. Al Qahtani, M. S. Alshammari, H. J. Blythe, A. M. Fox, G. A. Gehring, N. Andreev, V. Chichkov and Y. Mukovskii, International Conference on Strongly Correlated Electron Systems (Sces 2011) **391**, 012083 (2012).
2. N. Andreev, V. Chichkov, T. Sviridova, N. Tabachkova, A. Volodin, C. Van Haesendonck and Y. Mukovskii, EPJ Web of Conferences **40**, 15014 (2013).
3. W. S. Choi, D. G. Kim, S. S. A. Seo, S. J. Moon, D. Lee, J. H. Lee, H. S. Lee, D.-Y. Cho, Y. S. Lee, P. Murugavel, J. Yu and T. W. Noh, Physical Review B **77** (4), 045137 (2008).
4. D. I. Khomskii, Journal of Magnetism and Magnetic Materials **306** (1), 1-8 (2006).
5. X. Li, C. Lu, J. Dai, S. Dong, Y. Chen, N. Hu, G. Wu, M. Liu, Z. Yan and J.-M. Liu, Scientific Reports **4**, 7019 (2014).
6. X. L. Wang, D. Li, T. Y. Cui, P. Kharel, W. Liu and Z. D. Zhang, Journal of Applied Physics **107** (9), 09B510 (2010).
7. S. Blundell, *Magnetism in Condensed Matter*. (Oxford University Press, Oxford, 2001).
8. M. W. Kim, S. J. Moon, J. H. Jung, J. Yu, S. Parashar, P. Murugavel, J. H. Lee and T. W. Noh, Phys. Rev. Lett. **96** (24), 247205 (2006).
9. J. Baier, D. Meier, K. Berggold, J. Hemberger, A. Balbashov, J. A. Mydosh and T. Lorenz, Journal of Magnetism and Magnetic Materials **310** (2), 1165-1167 (2007).
10. A. N. Timothy, W.-G. Travis and S. Zollner, Annual Meeting of the Four Corners Section of the APS Vol **58**, No 12 (2013).
11. G. Gao, S. Jin and W. Wu, Applied Physics Letters **90** (1), 012509 (2007).

12. J. Nichols, J. Terzic, E. G. Bittle, O. B. Korneta, L. E. D. Long, J. W. Brill, G. Cao and S. S. A. Seo, Applied Physics Letters **102** (14), 141908 (2013).

13. D. Lee, J. H. Lee, P. Murugavel, S. Y. Jang, T. W. Noh, Y. Jo, M. H. Jung, Y. D. Ko and J. S. Chung, Applied Physics Letters**. 90**, 182540 (2007).

14. J. H. Lee, P. Murugavel, H. Ryu, D. Lee, J. Y. Jo, J. W. Kim, H. J. Kim, K. H. Kim, Y. Jo, M. H. Jung, Y. H. Oh, Y. W. Kim, J. G. Yoon, J. S. Chung and T. W. Noh, Advanced Materials **18** (23), 3125-3129 (2006).

15. J.-H. Lee, P. Murugavel, D. Lee, T. W. Noh, Y. Jo, M.-H. Jung, K. H. Jang and J.-G. Park, Applied Physics Letters **90** (1), 012903 (2007).

16. S. Ishiwata, Y. Kaneko, Y. Tokunaga, Y. Taguchi, T.-h. Arima and Y. Tokura, Physical Review B **81** (10), 100411 (2010).

17. X. Marti, F. Sanchez, V. Skumryev, V. Laukhin, C. Ferrater, M. V. Garcia-Cuenca, M. Varela and J. Fontcuberta, Thin Solid Films **516** (15), 4899-4907 (2008).

18. S. Picozzi, K. Yamauchi, B. Sanyal, I. A. Sergienko and E. Dagotto, Physical Review Letters **99** (22), 227201 (2007).

19. J. Hemberger, S. Lobina, H. A. Krug von Nidda, N. Tristan, V. Y. Ivanov, A. A. Mukhin, A. M. Balbashov and A. Loidl, Physical Review B **70** (2), 024414 (2004).

20. B. H. Kim and B. I. Min, Physical Review B **80**, 064416 (2009).

21. I. A. Sergienko, C. Şen and E. Dagotto, Physical Review Letters **97** (22), 227204 (2006).

22. I. V. Solovyev, Physical Review B **83** (5), 054404 (2011).

23. P. Kalpataru, M. Anamitra and M. Pinaki, EPL (Europhysics Letters) **84** (3), 37007 (2008).

24. Y. Konishi, Z. Fang, M. Izumi, T. Manako, M. Kasai, H. Kuwahara, M. Kawasaki, K. Terakura and Y. Tokura, Journal of the Physical Society of Japan **68** (12), 3790-3793 (1999).

25. D. T. O'Flynn, *Multiferroic properties of rare earth manganites*. PhD thesis, University of Warwick, 2010.

26. J. Baier, D. Meier, K. Berggold, J. Hemberger, A. Balbashov, J. A. Mydosh and T. Lorenz, Physical Review B **73** (10), 100402 (2006).

27. T. Kimura, G. Lawes, T. Goto, Y. Tokura and A. P. Ramirez, Physical Review B **71** (22), 224425 (2005).

28. K. Noda, S. Nakamura, J. Nagayama and H. Kuwahara, Journal of Applied Physics **97** (10), 103 (2005).

29. T. Kimura, S. Ishihara, H. Shintani, T. Arima, K. T. Takahashi, K. Ishizaka and Y. Tokura, Physical Review B **68** (6), 060403 (2003).

30. R. B. Gangineni, *Extrinsic Magnetotransport in Manganites and Its Dependence on Mechanical Strain*. (Cuvillier Verlag, Dresden, 2008).

31. T. Kimura, T. Goto, H. Shintani, K. Ishizaka, T. Arima and Y. Tokura, Nature **426**, 55-58 (2003).

32. N. Andreev, N. Abramov, V. Chichkov, A. Pestun, T. Sviridova and Y. Mukovskii, Acta Physica Polonica A **117** (1), 218-220 (2010).

33. M. Fiebig, Journal of Physics D-Applied Physics **38** (8), R123-R152 (2005).

34. N. Hur, S. Park, P. A. Sharma, J. S. Ahn, S. Guha and S. W. Cheong, Nature **429**, 392-395 (2004).

35. H. Schmid, Ferroelectrics **162**, 317-338 (1994).

36. M. W. Kim, P. Murugavel, P. Sachin, J. S. Lee and T. W. Noh, New Journal of Physics **6** (1), 156 (2004).

37. Y. Okimoto, Y. Konishi, M. Izumi, T. Manako, M. Kawasaki and Y. Tokura, Journal of the Physical Society of Japan **71** (2), 613-617 (2002).

38. M. Bastjan, S. G. Singer, G. Neuber, S. Eller, N. Aliouane, D. N. Argyriou, S. L. Cooper and M. Rübhausen, Physical Review B **77** (19), 193105 (2008).

39. A. S. Moskvin, A. A. Makhnev, L. V. Nomerovannaya, N. N. Loshkareva and A. M. Balbashov, Physical Review B **82** (3) (2010).

40. B.-Q. Hu, X.-M. Wang, T. Zhou, Z.-Y. Zhao, X. Wu and X.-L. Chen, Chinese Physics Letters **18** (2), 278 (2001).

41. J. M. D. Coey, Current Opinion in Solid State and Materials Science **10** (2), 83-92 (2006).

42. P. Negi, G. Dixit, H. M. Agrawal and R. C. Srivastava, Journal of Superconductivity and Novel Magnetism **26** (5), 1611-1615 (2013).

43. W. S. Choi, K. Taniguchi, S. J. Moon, S. S. A. Seo, T. Arima, H. Hoang, I. S. Yang, T. W. Noh and Y. S. Lee, Physical Review B **81** (20), 205111 (2010).

44. W. S. Choi, S. J. Moon, S. S. A. Seo, D. Lee, J. H. Lee, P. Murugavel, T. W. Noh and Y. S. Lee, Physical Review B **78** (5) (2008).

45. W. Zhou, H. Deng, H. Cao, J. He, J. Liu, P. Yang and J. Chu, Materials Letters **144**, 93-96 (2015).

46. J.C. Loudon, *An investigation of the unconventional phases in the lanthanum calcium manganite system*, PhD thesis, University of Cambridge, 2003.

47. S. Katsuaki, Japanese Journal of Applied Physics **20** (12), 2403 (1981).

48. W. P. Van Drent and T. Suzuki, Journal of Magnetism and Magnetic Materials **175** (1), 53-62 (1997).

Chapter 5

Mg-Doped ZnO

5.1 INTRODUCTION

ZnO as a semiconductor has received a great deal of research attention due to its wide direct band gap of approximately 3.37 eV, a large exciton binding energy of 60 meV at room temperature and high optical transmission in the visible range. In addition, this material has reliable structural, optical and magnetic properties that allow it to be widely used in electronic devices [1-5].

MgO has a wide band gap of ~ 7.8 eV; thus, the bandgap of ZnO can be widened by doping with MgO. Unlike the TM, magnesium (Mg) has no local moment, thus the ZnMgO belongs to a class of materials called d^0 magnetic materials. The magnetism of d^0 materials generally arises from defects such as oxygen vacancies, Mg vacancies and Zn vacancies [7-11].

The aim of this work is to understand how the magnetism of the ZnMgO system can be controlled and whether there is any correlation between the magnetism and band gap increase. For this purpose, a comprehensive investigation of the optical and magnetic properties of ZnMgO thin films was made using different substrates, varied deposition times (film thickness), different oxygen partial pressures and different growth techniques; all these will be discussed in detail below.

5.2 LITERATURE REVIEW OF ZnO AND Mg-Doped ZnO

The ionic radius of the Mg^{2+} is 0.57 Å; this is very close to that of Zn^{2+} which is 0.6 Å. Therefore, substitution of Zn^{2+} by Mg^{2+} does not result in a significant change in the lattice constants [12, 13].

$Zn_{1-x}Mg_xO$ is a solid solution that consists of ZnO and MgO, which have different crystal structures. ZnO has a wurtzite hexagonal structure with *a* and *c* lattice constants of 3.25 Å and 5.20 Å, respectively, whereas MgO has a cubic structure with a lattice constant of 4.24 Å [14]. $Zn_{1-x}Mg_xO$, however, has the hexagonal (wurtzite) structure for $x < 0.33$ and the cubic structure for $x > 0.5$ and a mixed phase for $0.33 < x < 0.5$, as shown in Figure 5.1 [9-14].

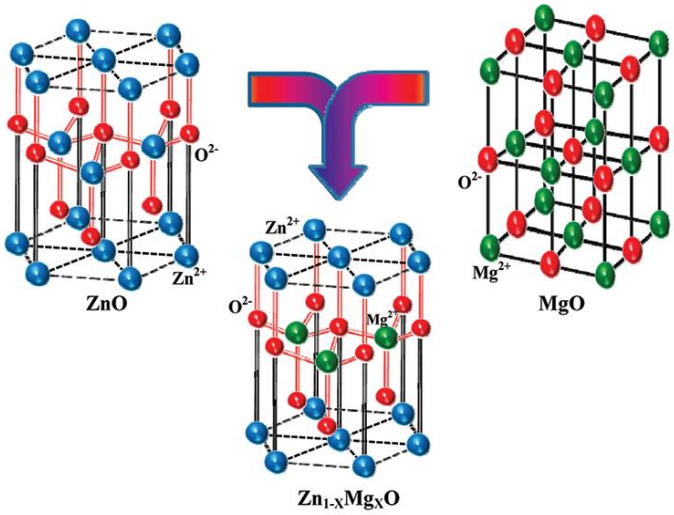

Figure 5.1: Schematic diagram showing the crystal structures of pure ZnO, MgO and $Zn_{1-x}Mg_xO$ [9].

The incorporation of Mg into ZnO has been widely found to shift the absorption band edge of the ZnMgO towards higher energy side. This can be seen from Figure 5.2 which illustrates the expansion of the band gap of ZnO thin film from ~ 3.3 eV to ~ 3.4 eV for ZnMgO thin film [15-19].

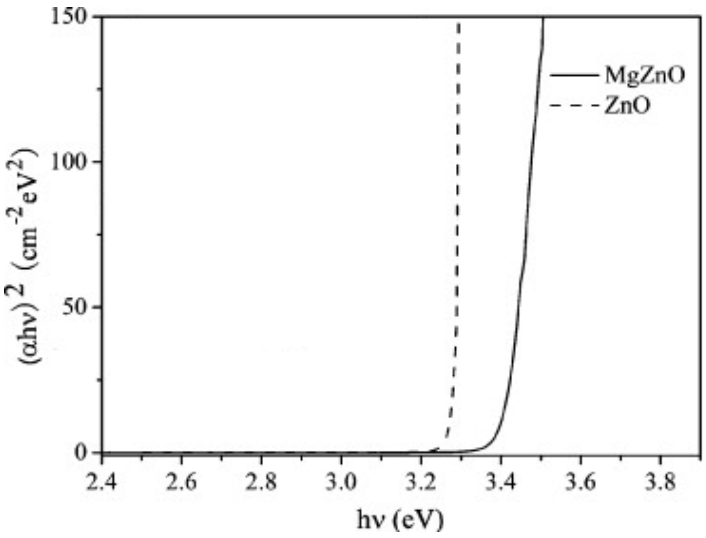

Figure 5.2: The difference between the band gaps of pure ZnO and Mg-doped ZnO [20].

Shifting the band gap of ZnMgO thin films may result from several complex factors such as the variation of Mg content, changing the lattice constant, the concentration of defects, tensile or compressive strain, and the Moss-Burstein effect [9, 15, 16]. According to the Moss-Burstein effect, since all states close to the conduction band are occupied, the oxygen vacancies give rise to an increase in the carrier concentration and hence the band gap increases [9].

The oxygen pressure has been found to strongly affect the amount of ablated species that arrive at the substrate using the PLD technique. Thus, increasing the oxygen pressure during the growth of thin films leads to a decreasing amount of Mg occupying the ZnO lattice; giving rise to the reduction of the band gap of ZnMgO. The Mg content is reduced because the Mg atoms are lighter than the Zn atoms; thus a higher scattering with ambient oxygen results in a lower concentration of Mg atoms in the plume, and therefore in the films grown at higher oxygen pressure [20, 21].

In addition, increasing the gas pressure during the growth using the PLD technique leads to a decrease in the deposition rate; this is because the mean free path of the target species decreases due to collision with gas atoms [22]. This behaviour has

also been found in the case of ZnMgO thin films grown by RF/DC sputtering deposited under different gas pressures. For example, increasing the growth pressure from 7.5×10^{-3} to 6.5×10^{-2} Torr was found to lead to a reduction in the deposition rate from 4.5 to 2.06 nm/min, respectively [23].

5.2.1 DEPENDENCE ON FILM THICKNESS

Different thicknesses of ZnMgO thin films can influence the structural, optical and magnetic properties of the ZnMgO. It is well known that the thickness of thin films is generally controlled by the duration of deposition, so the longer the deposition time, the thicker the thin film will be. Thickness of ZnMgO thin films can also be varied via gas pressure, where thicker films can be produced at low oxygen pressure, and *vice versa* [22, 23].

The crystallinity has been found to improve with increase in the thickness of ZnMgO thin film as a result of the strain reduction; thicker films exhibit improved crystallinity and have less defects and grain boundaries compared with thinner films [24-26].

XRD measurements have revealed that the increment in thickness is responsible for shifting the diffraction peaks to higher angles, as a result of reduced strain [24, 27]. Thus, increasing the film thickness of ZnMgO thin films has been found to increase the band gap energy due to decreasing strain [24]. The band gap of ZnMgO thin films has been reported to increase to ~ 4 eV as a function of thickness; suggesting that the band gap of ZnMgO is controllable by varying film thickness [27, 28].

The variation of the thickness of ZnMgO thin films can also influence the magnetic properties. It has been found that M_s increases first with increasing the thickness of the thin film and then decreases. This involves a change in the

concentration of Mg vacancies where vacancies increase at first in thinner films and then decrease when the films become thicker. Hence, the initial room temperature ferromagnetism (RTFM) can be ascribed to the existence of cation vacancies surrounding ZnO. Similar behaviour has been confirmed theoretically by Bahoosh *et al*. for Mg doped ZnO thin films in which thinner films display higher magnetisation compared to thicker ones [29, 30].

5.2.2 DEPENDENCE ON GAS PRESSURE

The existence of gas in the deposition chamber disturbs the kinetic energy of the ablated materials as they collide with species from the background gas. This effect gives rise to different density and morphology in the deposited films compared to those grown at base pressure. The deposition of ZnMgO under different oxygen partial pressures (P_{O_2}) has been found to cause variations in the structural, optical and magnetic properties [31-33].

Chen *et al*. investigated the ZnMgO thin films grown by sputtering on glass substrates at different gas pressures. The gas contained a mixture of Ar and O_2 with O_2:Ar ratios of 10:10, 15:10 and 20:10; as a result, the band gap decreased respectively from 3.39, 3.38 to 3.37 eV when the P_{O_2} ratio was increased [34]. Shifting the band gap towards the red region of the spectrum (narrowing the band gap) with the increase of oxygen partial pressure may be attributed to a decrease in carrier concentration (Burstein-Moss effect) [35-37].

RTFM has been observed in ZnMgO thin films, where there is a relationship between the RTFM and oxygen partial pressure [38, 39]; the observed magnetism has been reported to arise from the presence of intrinsic defects such as Zn and Mg vacancies [34]. This has been reported theoretically and experimentally in the literature. The increase in oxygen partial pressure has been found to increase Zn and Mg

vacancies, consequently enhancing the magnetisation. However, further increase of the oxygen partial pressure may lead to the formation of oxygen-related defects, such as interstitial oxygen and oxygen antisites that result in reducing the number of Mg vacancies, thereby lowering the magnetisation of the system [40-42].

5.2.3 DEPENDENCE ON SUBSTRATE TYPE

Using different substrates to grow thin films has been widely reported to investigate the effect of substrate type on several properties. The discussion below will mainly focus on quartz, glass and sapphire substrates and their effects on crystallinity, band gap and magnetic properties of ZnO and ZnMgO thin films.

Growth of ZnMgO thin films on glass, quartz and sapphire substrates has been reported to understand the affect the grain size. This, in turn, causes more interstitial Mg atoms at boundaries as a result of the small grain size of the films grown on glass and quartz substrates compared to those grown on a sapphire substrate. Depending on crystallinity and the mismatch between the film and substrate, defects and strain can be introduced, thereby influencing the magnetic properties of ZnMgO thin films. Based on the lattice mismatch, ZnMgO films grown on sapphire have shown a lower mismatch compared to films grown on glass and quartz substrates [46, 47]. A number of researchers have preferred *c*-cut sapphire substrates for preparing both undoped and doped ZnO thin films. This is because of the relatively low mismatch of ~ 2% between the film and the sapphire substrates compared to large lattice mismatches for other substrates [45-49].

The band gap values of ZnMgO films on glass and quartz substrates have been found to be ~ 3.56 eV; that is larger than that of pure ZnO. ZnMgO thin film grown on a sapphire substrate, however, has been found to have a band gap of ~ 3.61 eV [43-45].

The magnetic behaviour of ZnO thin films has been reported to show a correlation with the substrate. The films deposited on sapphire substrates have been found to display a higher ferromagnetic behaviour in comparison with those grown on glass and quartz, and this might be attributed to the comparatively better quality of the films grown on sapphire substrates [50].

5.3 SAMPLE PREPARATION

ZnMgO thin films were deposited on silicon, glass, quartz and sapphire substrates under different deposition times and oxygen pressures using sputtering and PLD techniques. The main objective of this chapter is to investigate the optical and magnetic properties of ZnMgO thin films, understanding the origin of ferromagnetism and any possible correlation between the band gap and magnetism.

The present work is a collaboration project carried out between the research group led by Prof K. V. Rao at KTH, Royal Institute of Technology, Stockholm, Sweden, and our magnetic oxides group led by Prof. Gillian Gehring. The main work of the KTH included: making the targets, growing thin films and performing the structural studies; whereas the optical and magnetic measurements were made at the University of Sheffield. So far, this project has produced some interesting results: the data for ZnMgO films on Si and glass substrates deposited by sputtering have already been published in Materials Research Society Symposium Proceedings [51, 52].

Four sets of ZnMgO films were prepared: the first and second sets were deposited by DC/RF magnetron sputtering on Si and glass substrates. The first group was grown as a function of deposition time while the second group was deposited as a function of oxygen partial pressure. The ZnMgO films were deposited by co-sputtering

pure Mg (99.99%) and Zn (99.99%) targets with 10 W direct current (DC) power on the Mg target, while radio frequency (RF) power on the Zn target was 50 W.

Before deposition, for the first group, the growth chamber was evacuated to a base pressure of ~ 7.5×10^{-6} Torr, and then backfilled with a mixture of argon and oxygen gases ($Ar+O_2$). In the second group, the deposition chamber was backfilled with a mixture of nitrogen and oxygen (N_2+O_2).

In both groups, the total pressure was kept at 1.13×10^{-3} Torr. For the ZnMgO films deposited as a function of deposition time (first group), the oxygen partial pressure was maintained at 1.13×10^{-4} Torr while the films were grown at different deposition times. For the ZnMgO films deposited as a function of oxygen pressure (second group), the deposition time was fixed at 60 mins while the oxygen pressure was varied.

It should be mentioned that the sputtering efficiency of nitrogen is lower than that of argon; this directly affects the thickness of the ZnMgO films [53]. Thus, the films deposited in ($Ar+O_2$) environment were thicker than those deposited in an environment of (N_2+O_2), as seen in Table (5.1).

The third and fourth groups of ZnMgO films were deposited using PLD technique on Si, glass, quartz and sapphire substrates as a function of deposition time and oxygen pressure, respectively. The $Zn_{1-x}Mg_xO$ (x = 5%) target was prepared using a ceramic method from stoichiometric ZnO (99.99 %) and MgO (99.99 %) powders. The target had a diameter of ~ 13.8 mm and was 5.2 mm thick. The target was sintered at 600 ^{o}C and 700 ^{o}C for 1 hour, and finally sintered at 900 ^{o}C for 4 hours.

In the PLD method, the Nd:YAG laser was operated at a wavelength of 355 nm with a pulse duration of 30 ns at a repetition rate of 10 Hz and with an energy density of 100 mJ/pulse. The laser beam was focused on to the target with a lens of 45 cm focal

length and at an incidence angle of 45°. The distance between the target and substrate was kept constant at 5 cm throughout the deposition process. During the growth process, the target holder was kept rotating at a suitable speed in order to avoid target drilling.

Based on the above-mentioned two deposition methods, Table (5.1) shows the growth conditions for the first and second groups of ZnMgO films deposited using sputtering technique; Table (5.2) shows the growth conditions for the third and fourth groups of ZnMgO films deposited by PLD technique.

It is noteworthy that an important aspect of this project is the comparison of the structural, optical and magnetic properties of ZnMgO thin films deposited by sputtering and PLD techniques. As noted above, although the growth conditions differed from one group to another, a couple of films were deposited under similar conditions. These films are highlighted and presented in bold in the following tables:

Table 5.1: Summary of the growth conditions for the ZnMgO films grown using sputtering technique. The two films highlighted and marked in bold were deposited under the same nominal conditions.

Group I - as a function of deposition time				
Substrates	Time (mins)	Oxygen partial pressure (Torr) Total pressure ($Ar+O_2$) = 1.13×10^{-3} (Torr)	Thickness (nm)	Mg concentration from EDS measurements (%)
Si and glass	30	1.13×10^{-4}	40	6
Si and glass	**60**	**1.13×10^{-4}**	**80**	**6**
Si and glass	90	1.13×10^{-4}	120	6.1
Si and glass	120	1.13×10^{-4}	160	6
Si and glass	150	1.13×10^{-4}	200	6
Si and glass	180	1.13×10^{-4}	240	6.8
Group II - as a function of oxygen partial pressure				
Substrates	Time (mins)	Oxygen partial pressure (Torr) Total pressure (N_2+O_2) = 1.13×10^{-3} Torr	Thickness (nm)	Mg concentration from EDS measurements (%)
Si and glass	60	$5\% = 0.56\times10^{-4}$	61.4	18
Si and glass	**60**	**$10\% = 1.13\times10^{-4}$**	**51.6**	**16**
Si and glass	60	$15\% = 1.68\times10^{-4}$	41.6	17
Si and glass	60	$20\% = 2.24\times10^{-4}$	31.7	10

Table 5.2: Summary of the growth conditions for the ZnMgO films deposited using PLD technique. The two films highlighted and marked in bold were deposited under the same nominal conditions.

Group III - as a function of deposition time				
Substrate	Time (mins)	Oxygen pressure (Torr)	Thickness (nm)	Mg concentration from EDS measurements (%)
Si, glass, quartz and sapphire	10	15×10^{-3}	55	…
Si, glass, quartz and sapphire	20	15×10^{-3}	111	…
Si, glass, quartz and sapphire	**30**	**15×10^{-3}**	**166**	**10.6**
Si, glass, quartz and sapphire	40	15×10^{-3}	221	11
Group IV - as a function of oxygen pressure				
Substrate	Time (mins)	Oxygen pressure (Torr)	Thickness (nm)	Mg concentration from EDS measurements (%)
Si, glass, quartz and sapphire	30	6.75×10^{-3}	228	10.2
Si, glass, quartz and sapphire	**30**	**15×10^{-3}**	**176**	**10.6**
Si, glass, quartz and sapphire	30	37.5×10^{-3}	131	9.9
Si, glass, quartz and sapphire	30	75×10^{-3}	126	9.5
Si, glass, quartz and sapphire	30	112.5×10^{-3}	105	8.9

5.4 EXPERIMENTAL RESULTS

Only the ZnMgO films deposited on Si substrates were used to obtain film thickness using FIB coupled with SEM. The error in thickness measurements were estimated to be ~ 5% due to the limitations in the SEM resolution. The Si substrate was preferred because, for a precise optimal analysis, the substrate should be conducting or at least semi-conducting, otherwise charges will be encountered. The compositions of ZnMgO films were determined by EDS.

Room temperature optical and magnetic measurements were taken on the ZnMgO films deposited on glass, quartz and sapphire substrates for all the previous four groups. The band gap of the ZnMgO films deposited on Si substrate was not obtainable because the silicon band gap is ~ 1.1 eV, whereas the measurements were taken in the region of 1.75 – 4.5 eV where the band gap of ZnO is ~ 3.37 eV. This means that in this spectral region the ZnMgO films deposited on Si substrates are totally opaque and therefore cannot be studied.

The characteristics of the ZnMgO films grown using the sputtering technique will be investigated first, followed by the films grown using PLD technique.

5.4.1 SPUTTERED ZnMgO FILMS

The structural, optical and magnetic properties of the sputtered ZnMgO films grown under different conditions (groups I and II) are presented and discussed below. Although FIB and EDS analyses were performed for all ten samples in both groups, showing all the structural data for all films is difficult. Thus, only the FIB and EDS data for one sample of those deposited on Si substrate will be shown here as an example.

5.4.1.1 Structural Properties

A typical cross section of a ZnMgO film grown on Si substrate was measured by FIB technique, as shown in Figure 5.3. This film was deposited for 90 mins under an oxygen partial pressure of 1.13×10^{-4} Torr. The measurement shows a homogeneous growth of the film; film thickness was found to be in the range of ~ 120 nm.

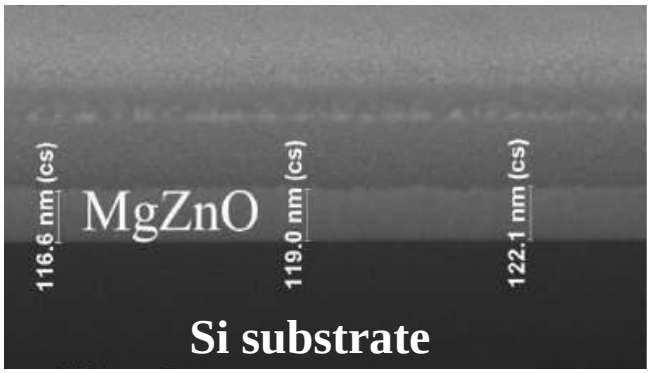

Figure 5.3: Cross-section measurement of ZnMgO film deposited by sputtering on a Si substrate for 90 mins at an oxygen partial pressure of 1.13×10^{-4} Torr where the film thickness can be measured [52].

The EDS spectrum of the ZnMgO film grown on a Si substrate for 90 mins under an oxygen partial pressure of 1.13×10^{-4} Torr is shown in Figure 5.4.

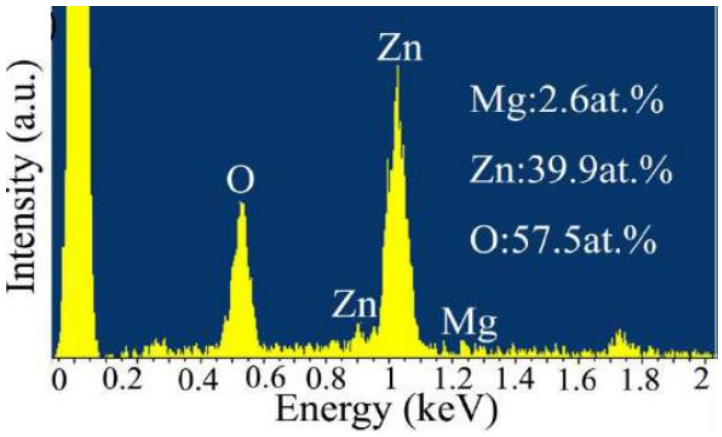

Figure 5.4: EDS spectrum of the ZnMgO film deposited on a Si substrate for 90 mins at an oxygen partial pressure of 1.13×10^{-4} Torr [52].

EDS measurements of all the sputtered ZnMgO films showed only the existence of the Mg, Zn and O elements, meaning that there were no metallic contaminants in the samples within the detection limits of the EDS. The percentages of the detected Mg, Zn and O elements are seen in the inset of the Figure 5.4. Thus, the ratio of Mg to Zn is 0.065; implying that 6.1% is substitutional of Mg to Zn in the $Zn_{1-x}Mg_xO$ matrix. The high oxygen concentration, however, may be from the oxygen in the Si substrate as it has a layer of SiO_2 on its top surface.

The concentration of Mg in the films deposited as a function of time was found to be in the range from 6 to 6.8 %; for the films deposited as a function of oxygen partial pressure it was found to vary from 18 to 10 % with increasing the oxygen partial pressure from 5 to 20%. Decreasing the Mg concentration in the ZnMgO films with the increase in the oxygen partial pressure may be attributed to the scattering effect. This is because under low oxygen pressure the ejected species from the target experience fewer collisions with the atoms of the sputtering gas. Thus, the deposition rate is higher for the films deposited under low oxygen pressure, and *vice versa* [21, 23].

5.4.1.2 Optical Properties

The optical transmission and reflection measurements were carried out on all sputtered ZnMgO films, except the ones grown on Si substrates. From these measurements, the absorption was then deduced using Tauc plot to determine the band gap for each film. Typical absorption data from the ZnMgO film deposited on a glass substrate are shown in Figure 5.5. This plot is shown to indicate how the E_g values of the ZnMgO films, shown in this section, were found. The data are cut at 4 eV because above this energy the glass substrate is absorbing sufficiently.

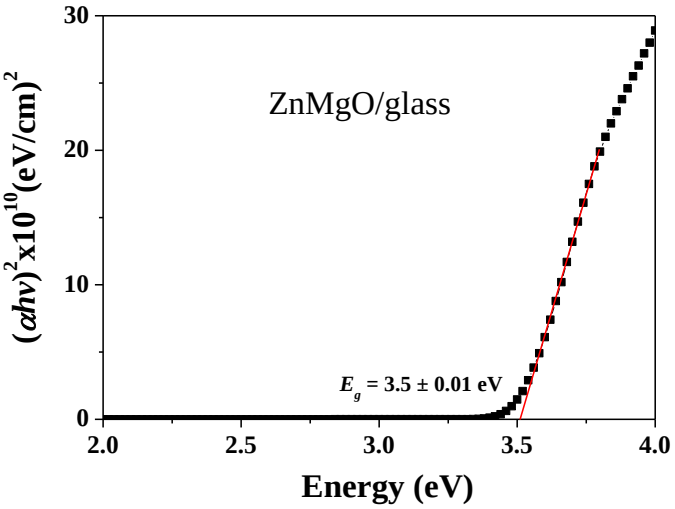

Figure 5.5: A typical optical absorption spectrum of the ZnMgO film deposited on a sapphire substrate deposited by sputtering technique.

As a result of Mg doping, all the sputtered ZnMgO films showed an increase in E_g values compared to that of pure ZnO. However, the magnitude of this increase was influenced by the variation of film thickness, and oxygen pressure [51, 52].

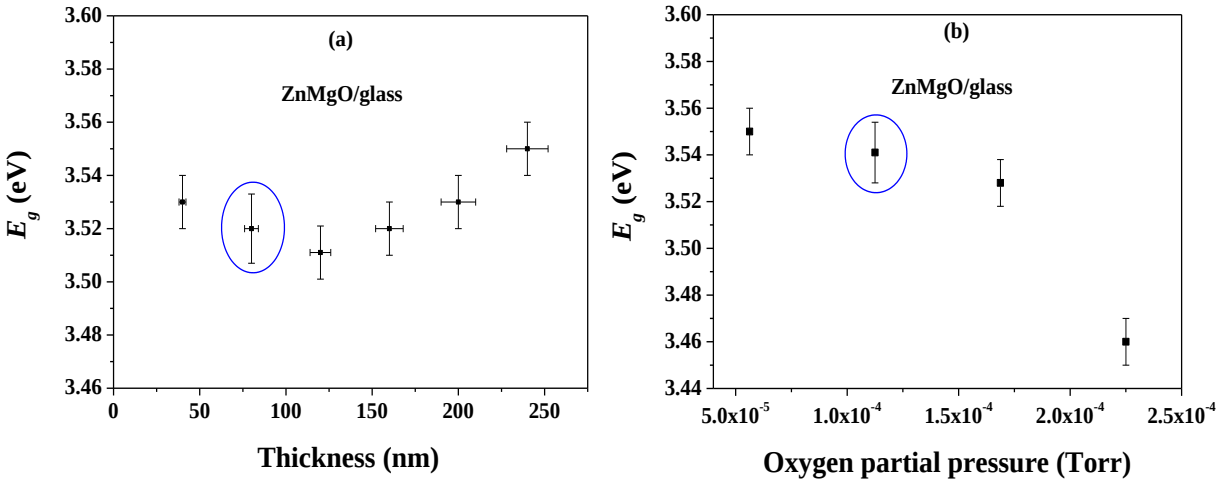

Figure 5.6: The band gap of sputtered ZnMgO films on glass substrate as a function of (a) thickness and (b) oxygen partial pressure. The two samples circled in blue are similar but with small different values of E_g; the sample in (a) was sputtered with ($Ar+O_2$), whereas the sample in (b) was sputtered with (N_2+O_2).

Figures 5.6 (a) and 5.6 (b) show the band gap of the ZnMgO films deposited on glass substrate as a function of thickness and oxygen partial pressure, respectively.

Increasing the deposition time results directly in an increase of film thickness. Thus, the change in the band gap is shown and studied as a function of film thickness, as in Figure 5.8 (a). Increasing the oxygen content, however, leads to a reduction in thickness if deposition time is held constant, as shown in Table (5.1).

Two samples were grown under nominally identical conditions; the E_g values of these samples are circled in blue in Figures 5.8 (a) and 5.8 (b). However, the small difference between the two values of E_g may be due to the ambient atmosphere effect, where the sample in the Figure 5.8 (a) was sputtered with ($Ar+O_2$), while the sample in the Figure 5.8 (b) was sputtered with (N_2+O_2).

It can be noted that as the thickness increases, the E_g decreases: first from 3.53 to 3.51 eV; and then increases to 3.55 eV. The initial reduction in the value of E_g with increasing thickness might be due to the high strain produced in relatively thin films. However, increasing E_g with increasing thickness may be ascribed to the compressive strain shifting the energy band gap to higher values [52].

The variation of E_g with oxygen partial pressure might be due to the Mg concentration that was found to be higher at low oxygen partial pressure, and *vice versa* [21, 23]. Thus, increasing the oxygen pressure leads to a reduction in the Mg concentration and, therefore, decreases the E_g value. In addition, the reduction in the value of E_g at high oxygen partial pressure could be due to the expansion of the lattice constant that increases with increasing oxygen pressure [16].

The E_g has been found to depend weakly on film thickness but strongly on oxygen pressure. This can be seen from the large variation of E_g with oxygen pressure, compared to that with film thickness.

5.4.1.3 Magnetic Properties

Magnetic loops of all the sputtered ZnMgO films grown on glass substrates were measured at 300 K. A typical hysteresis loop of one of these samples is shown in Figure 5.7. The magnetisation saturation and coercivity can be determined from this plot. Thus, the value of ($Hc \approx 0$ Oe) indicates that the ZnMgO belongs to d^0 materials.

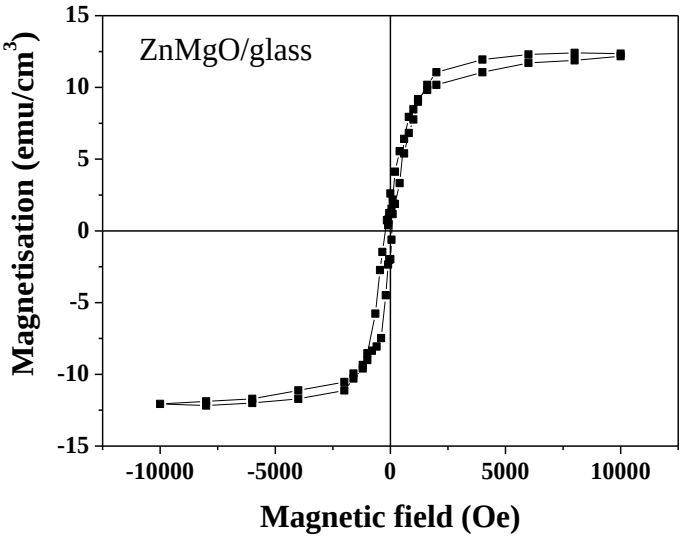

Figure 5.7: A typical hysteresis loop measured at 300 K of a ZnMgO film on a glass substrate grown by sputtering. The diamagnetic contribution from the glass substrate has been subtracted.

Variation of M_s, with thickness and oxygen pressure were observed. Figure 5.8 (a) shows the thickness-dependent data where there is an initial increase of the M_s with increasing film thickness, and then a decrease with increasing the thickness further.

The M_s increases initially with increasing thickness until reaching its maximum value of ~ 13 emu/cm^3 at the thickness of 120 nm. This behaviour may be attributed to the cation defects, such as magnesium vacancies and zinc vacancies, oxygen vacancies and strain effects since they are high in low thickness films [51, 52].

Beyond the film thickness of 120 nm, the concentration of cation defects and strain starts to decrease, resulting in decreasing the M_s to nearly zero for thick films; corresponding to that of the bulk material [54].

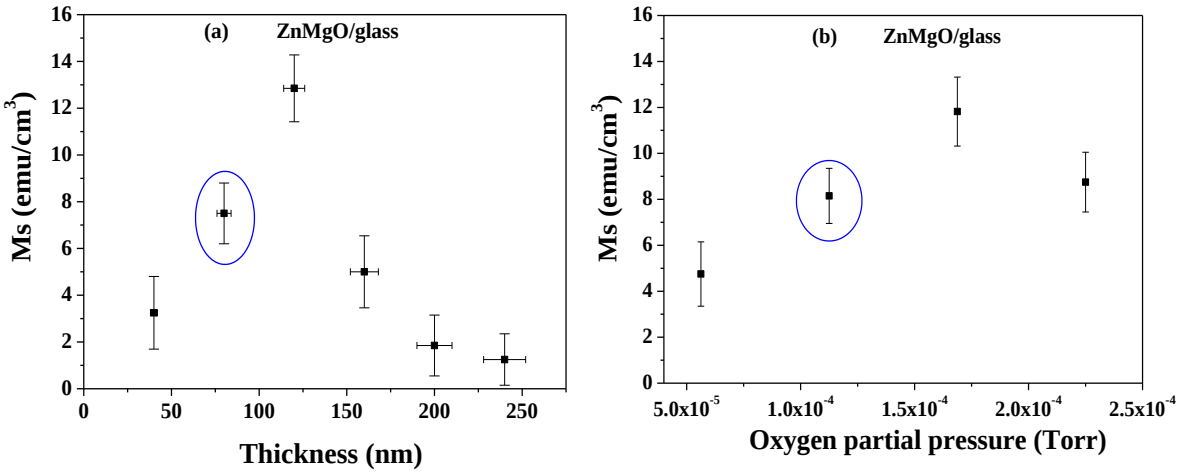

Figure 5.8: The magnetisation saturation of ZnMgO films deposited using sputtering on glass substrate as a function of (a) thickness and (b) oxygen partial pressure. The two samples circled in blue are nominally the same but with a small difference in M_s; the sample in (a) was sputtered with ($Ar+O_2$), whereas the sample in (b) was sputtered with (N_2+O_2).

Figure 5.8 (b) shows that increasing the oxygen pressure causes an increase in the M_s; this is possibly due to Mg and Zn vacancies but not due to the oxygen vacancies. However, at high oxygen pressure, all vacancies disappear; this leads to a decrease in the M_s [30, 42, 55].

Figures 5.8 (a) and 5.8 (b) show the M_s values for the two samples that were grown under the same nominal conditions. However, the small difference between the two values of M_s may be due to the sensitivity of the magnetisation to the ambient atmosphere, where the sample in Figure 5.8 (a) was sputtered with ($Ar+O_2$) while the sample in Figure 5.8 (b) was sputtered with (N_2+O_2) [30, 53].

The M_s was found to be influenced more by film thickness compared to oxygen pressure. The change of M_s due to film thickness is larger than that due to oxygen pressure; implying that stain plays a significant role in the magnetisation of thin films.

5.4.2 ZnMgO FILMS GROWN BY PLD

The ZnMgO films grown by PLD are divided into two groups (III and IV), as in Table (5.2). The third group contains four films deposited as a function of thickness, while the fourth group has five films deposited as a function of oxygen pressure.

The FIB and EDS analyses of a ZnMgO film grown on a Si substrate are used to demonstrate the structural data. The optical and magnetic properties of the ZnMgO films grown on glass, quartz and sapphire substrates are presented and discussed.

5.4.2.1 Structural Properties

From the surface analysis, ZnMgO films prepared by PLD were found to be deposited uniformly. Figure 5.9 presents a FIB cross section of the ZnMgO film grown on a Si substrate for 40 mins under an oxygen pressure of 15×10^{-3} Torr. The data show that the average thickness of the film is 221 nm.

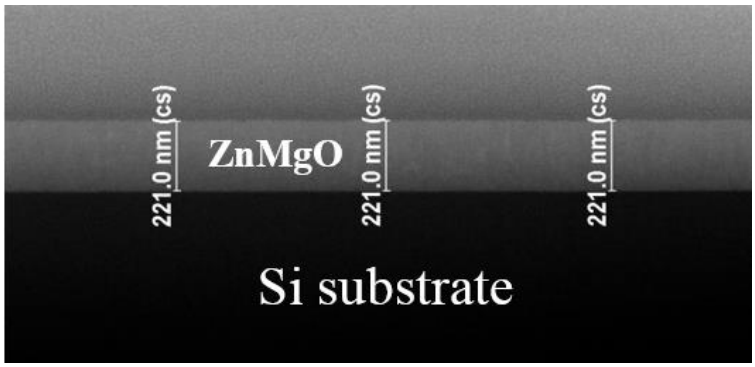

Figure 5.9: Cross-section measurement of ZnMgO film deposited by PLD on a Si substrate for 40 mins at an oxygen partial pressure of 15×10^{-3} Torr where the film thickness can be measured.

EDS measurements were also carried out on all the ZnMgO films grown by PLD. The analysis of the EDS data showed only the presence of Mg, Zn and O elements; this was a similar observation to that for the sputtered ZnMgO films.

The EDS spectrum of the ZnMgO film grown on a Si substrate for 40 mins under an oxygen partial pressure of 15×10^{-3} Torr is shown in Figure 5.10.

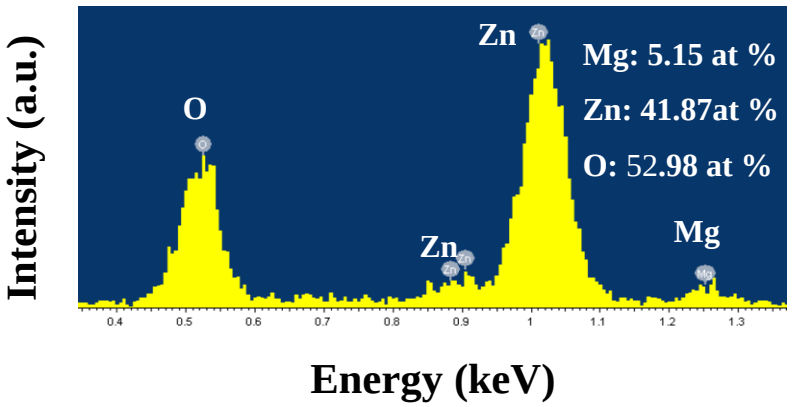

Figure 5.10: EDS spectrum of the ZnMgO film deposited by PLD on a Si substrate for 40 mins at an oxygen pressure of 15×10^{-3} Torr [54].

The ratio of Mg to Zn is 0.123; meaning that the substitution of Zn by Mg in PLD ZnMgO film was ~ 11%. This indicates that the Mg concentrations in the PLD films were larger than that in the ZnMgO target by a factor of greater than 2; similar results were previously found by Ohtomo *et al* [19].

The difference between the Mg concentration in the ZnMgO film from that of the target might be attributed to the vapour pressure of Zn which is much larger than that of Mg where the high energy laser is the responsible for evaporating the target material. In other words, Zn atoms can be easily desorbed from the substrate, leading to the condensation of Mg atoms on the substrate and therefore increasing the concentration of Mg in the ZnMgO film [19, 56]. Hence, the high Mg content in the PLD films may be the main reason behind the changes in the optical and magnetic data between the ZnMgO films deposited by PLD and those grown by sputtering.

5.4.2.2 Optical Properties

The optical absorption spectra were obtained for the ZnMgO films grown by PLD technique on glass, quartz and sapphire substrates. The E_g values were determined for both sets of films grown as a function of thickness and oxygen pressure, as shown in Figures 5.11 (a) and 5.11 (b), respectively.

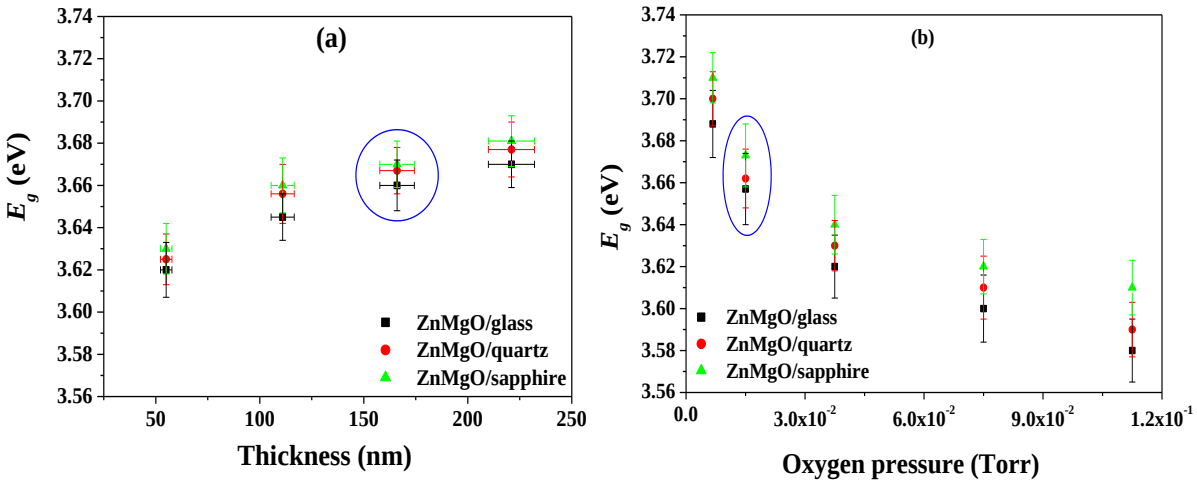

Figure 5.11: Optical band gap of ZnMgO films deposited by PLD on glass, quartz and sapphire substrates as a function of (a) thickness and (b) oxygen partial pressure.

The E_g values of the ZnMgO films were found to be more dependent on oxygen pressure than thickness. This can be clearly seen from the change in the magnitude of E_g due to the variation of oxygen pressure which was larger than the change in magnitude due to thickness.

As with the ZnMgO films grown using sputtering, increasing film thickness resulted in an increase of the E_g value as a result of the strain reduction in high thickness films [52, 54]. Increasing the oxygen pressure, on the other hand, resulted in a decrease in the E_g,; this might be due to the expansion of the lattice constant as a result of less Mg incorporation [16]. Nevertheless, the ZnMgO films deposited by PLD exhibited

larger E_g values compared to those of the sputtered films. This is attributed to the increased amount of Mg in the PLD films compared to the ones prepared by sputtering.

Since increasing the oxygen pressure led to a reduction in thickness, as seen in Figure 5.12, it can be deduced that the thick ZnMgO films (grown at low oxygen pressure) have larger E_g and *vice versa*. This is similar to changing the E_g as a function of thickness (Figure 5.11) except that the oxygen pressure has more influence on the values of E_g than film thickness.

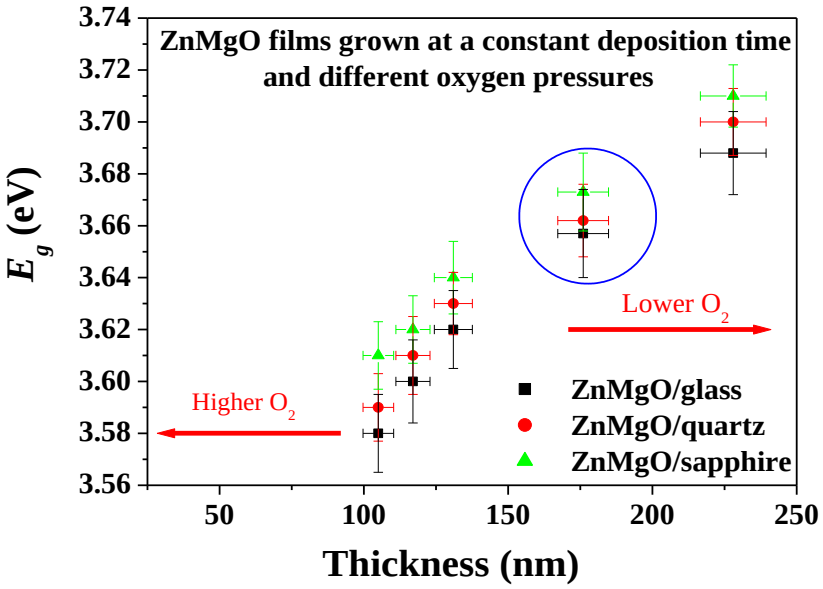

Figure 5.12: Optical band gap of ZnMgO films deposited using PLD on glass, quartz and sapphire substrates as a function of oxygen pressure (plotted as a function of thickness).

It can be seen that the E_g values also depended on the substrate type. The ZnMgO films grown on sapphire substrates under all conditions showed larger E_g values compared to the films grown on glass and quartz substrates. This could be due to the large mismatch between the film and glass and quartz substrates, resulting in a considerable strain and decreasing the band gap [48]. The films deposited under similar conditions show comparable E_g values; these are circled in blue.

5.4.2.3 Magnetic Properties

Magnetic loops for all the ZnMgO films were measured at room temperature. A typical hysteresis loop for ZnMgO grown using PLD on a sapphire substrate is shown in Figure 5.13, showing $H_c \approx 0$ Oe. The diamagnetic signal of the sapphire substrate has been subtracted.

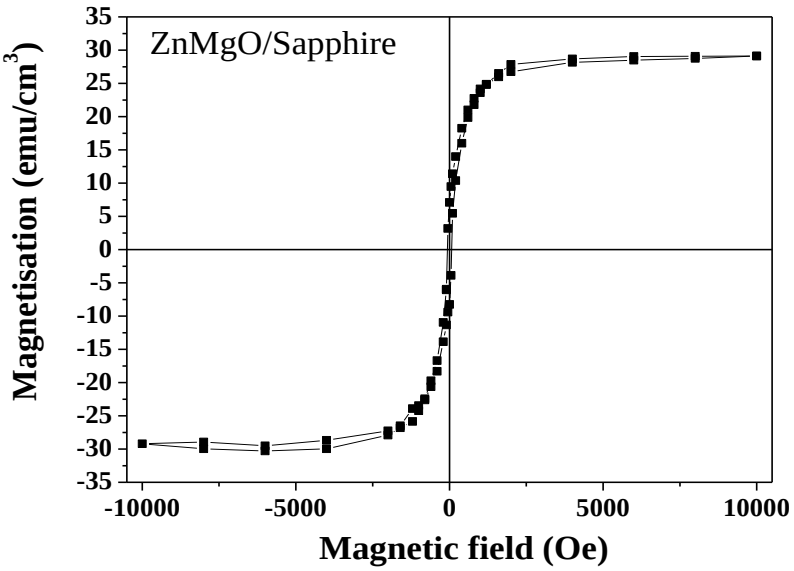

Figure 5.13: A typical hysteresis loop of a ZnMgO film on a sapphire substrate grown using PLD. The diamagnetic contribution of the sapphire substrate has been subtracted.

The variation of the M_s, with different film thicknesses and oxygen pressures was observed. The M_s data of the samples grown by PLD technique on glass, quartz and sapphire substrates as a function of thickness and oxygen pressure were obtained. Figure 5.14 (a) shows that increasing thickness resulted in decreasing the M_s; this might be due to the strain effect which is higher for thinner films, in addition to the oxygen vacancies which decrease with increasing thickness [51, 52].

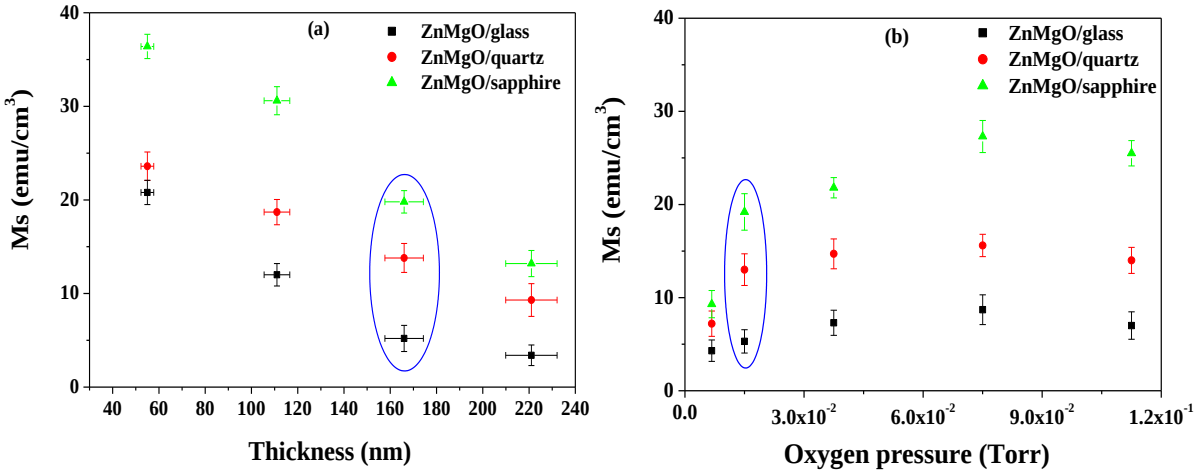

Figure 5.14: Variation of M_s with (a) thickness and (b) oxygen pressure for ZnMgO films grown on glass, quartz and sapphire substrates by PLD.

It can also be noted that the difference between the M_s values of different substrates was relatively large at low thicknesses and smaller at thicker ones; this is because the surface effect is higher for thinner films compared to the films with large thicknesses [54].

Figure 5.14 (b) shows the magnetic data of the ZnMgO films grown on different substrates as a function of oxygen pressure by PLD method. These films exhibit comparable behaviour to the films grown by sputtering as previously illustrated in Figure 5.8 (b). The M_s data for the films grown on sapphire substrates were higher compared to the films grown on quartz and glass substrates. This might indicate that the defects densities in the ZnMgO films deposited on sapphire substrates are higher than the concentration of defects in the ZnMgO films deposited on glass and quartz substrates [57].

The M_s of the ZnMgO films grown on quartz substrate was larger than that of films grown on glass substrate. This might be due to the reduction in the grain size of the films deposited on quartz substrates compared to the films deposited on glass,

leading to more strained films which in turn produce higher magnetisation [30, 58]. The films deposited under similar conditions; showing comparable M_s values; this is seen in Figures 5.14 (a) and 5.14 (b) where the films are circled in blue.

Increasing M_s with increasing O_2 is believed to be due to the effect of thickness rather than oxygen since increasing oxygen pressure reduces thickness [22, 54] and, as a result, the M_s increases, as shown in Figure 5.15.

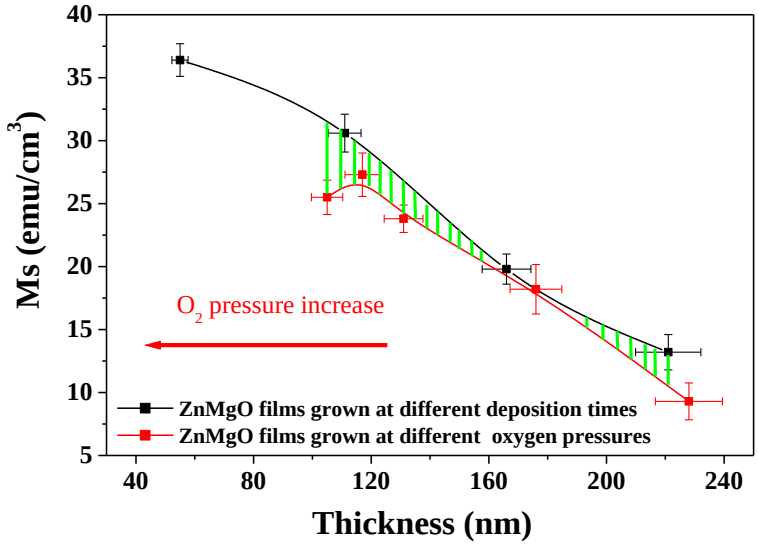

Figure 5.15: Variation of M_s of the PLD ZnMgO films on sapphire substrate as a function of thickness. The black line is the change of thickness with deposition time and the red line is the change of thickness with oxygen pressure. The lines are guides for the eye. The green vertical lines represent the difference between the oxygen pressure and thickness effects.

The oxygen pressure reduces the magnetisation by the amount shown in Figure 5.15 (the vertical green lines). Hence, this is not a large change compared to the change due to the variation in film thickness.

Changing the band gap may affect the magnetisation; this finding is illustrated in Figure 5.16. Hence, there is a correlation between increasing (decreasing) the E_g and decreasing (increasing) the M_s. This might be due to strain effect in the case of films deposited at different thicknesses, and to lattice constant for films grown at different oxygen pressures.

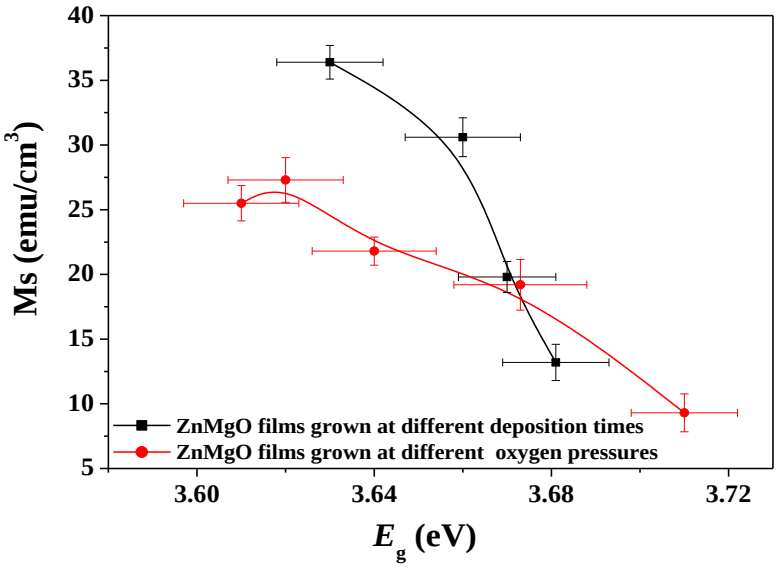

Figure 5.16: Variation of the band gap with the magnetisation saturation for ZnMgO films deposited on sapphire substrates by PLD at different thicknesses (black) and oxygen pressures (red), respectively. The lines are guides for the eye.

By comparing the optical and magnetic data of the ZnMgO films grown using sputtering and PLD, it can be concluded that the PLD ZnMgO films exhibit higher values of E_g and M_s compared to the sputtered ZnMgO films. This can be clearly seen from the larger values of the E_g and M_s for the ZnMgO films grown on glass substrates in Figures 5.17 (a) and 5.17 (b).

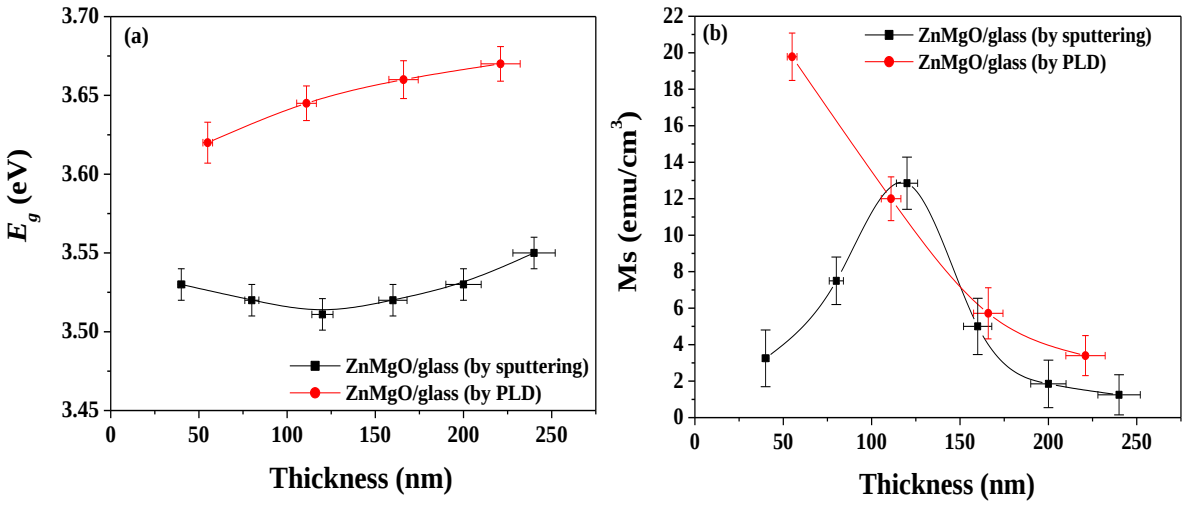

Figure 5.17: Variation of (a) the E_g and (b) M_s of the ZnMgO films deposited on glass substrates by sputtering (black) and PLD (red) techniques as a function of film thickness.

The different values of E_g for the ZnMgO films grown by sputtering and PLD are due to the increased Mg content in the films grown by PLD.

In terms of the magnetic data shown in Figure 5.17 (b), the sputtered and PLD ZnMgO films with thicknesses higher than 120 nm show almost the same behaviour of the M_s when film thickness increases. On the other hand, the M_s of the sputtered and PLD ZnMgO films of thicknesses lower than 120 nm behaved differently with thickness. Changing the M_s of the sputtered films with thickness in this way could be attributed to the cation defects of Mg and Zn vacancies; this behaviour has been found many times by Rao's group [4, 30, 38, 52, 53]. In the case of the PLD films, there is a clear thickness dependence where the magnetisation is high in film with low thickness (high strain) and *vice versa*. This behaviour has also been widely reported by many research groups [24, 25, 54, 59, 60]. These findings indicate that the early stages of thin film growth are highly sensitive to the growth method.

In general, the difference between the M_s values for the ZnMgO films grown by sputtering and PLD may depend on the types of defect produced in both techniques; oxygen vacancies are likely to be produced more in the ZnMgO films grown by PLD technique [16, 54].

5.5 SUMMARY AND CONCLUSIONS

ZnMgO thin films were prepared on Si, glass, quartz and sapphire substrates using sputtering and PLD techniques. Different growth conditions were varied, including deposition times (film thickness), oxygen pressure and substrate type. This is in order to find out whether controlling the band gap affects the magnetism or not.

Changing the oxygen pressure was found to show a stronger influence on the E_g of the ZnMgO films compared to the film thickness parameter. This might result from the effect of the oxygen on the lattice constant where increasing the oxygen pressure results in expanding the lattice constant and, therefore, decreases the band gap.

The E_g was found to be affected by the substrate type. The ZnMgO films deposited on sapphire substrates have higher band gap energies than the ZnMgO films deposited on glass and quartz substrates. This could be attributed to the amount of strain produced by different substrates where the glass and quartz substrates have larger strain than sapphire substrate; causing a decrease of the band gap value of ZnMgO films.

ZnMgO films grown by PLD exhibit larger E_g values in comparison with those grown by sputtering. This is attributed to the increased Mg content in the ZnMgO films deposited using PLD technique compared to the ZnMgO films grown using sputtering technique, enhancing the optical properties.

Regarding the magnetic data, the M_s of the ZnMgO films was found to depend more strongly on film thickness than oxygen content; this is possibly due to the relationship of strain and defects with thickness. There is a thickness dependence in terms of M_s but it is not due to surface magnetism; this is because the M_s values of all the ZnMgO films cannot be fitted by the expression: $M/d = M(bulk)+M(surface)/d$.

The ZnMgO films deposited on sapphire substrates were found to show the highest M_s compared to the films grown on other substrates. This indicates the importance of defects induced by different substrates that enhance the magnetisation. Consequently, it may be concluded that the ZnMgO films grown on sapphire substrates have more oxygen vacancies, in comparison with the ZnMgO films grown on quartz and glass substrates.

ZnMgO films grown using PLD also show larger M_s values in comparison with the films grown using sputtering. This might be attributed to the type of defects produced by each deposition method. The ZnMgO films deposited by the PLD technique are believed to have more oxygen vacancies, mainly enhancing the magnetisation.

The optical and magnetic data were found to show a correlation between E_g and M_s. Thus, large magnetisation values in ZnMgO thin films could be obtained by decreasing the band gap and *vice versa*. This might be ascribed to the significant role that the strain can play in controlling both properties.

No studies in the literature could be found on making nominally the same ZnMgO thin films using sputtering and PLD techniques. This study may provide important results in terms of the structural, optical and magnetic properties of ZnMgO thin films grown by sputtering and PLD techniques although further exploration may be needed.

5.6 REFERENCES

1. J. M. D. Coey, M. Venkatesan and C. B. Fitzgerald, Nature Materials **4**, 173-179 (2005).
2. T. Dietl, H. Ohno, F. Matsukura, J. Cibert and D. Ferrand, Science **287** (5455), 1019-1022 (2000).
3. J. K. Furdyna, Journal of Applied Physics **64** (4), R29-R64 (1988).
4. M. Kapilashrami, J. Xu, V. Ström, K. V. Rao and L. Belova, Applied Physics Letters **95** (3), 033104 (2009).
5. S. D. Sarma, American Scientist **89** (6), 516-523 (2001).
6. G. Xing, D. Wang, J. Yi, L. Yang, M. Gao, M. He, J. Yang, J. Ding, T. C. Sum and T. Wu, Applied Physics Letters **96** (11), 112511 (2010).
7. J. B. Yi, C. C. Lim, G. Z. Xing, H. M. Fan, L. H. Van, S. L. Huang, K. S. Yang, X. L. Huang, X. B. Qin, B. Y. Wang, T. Wu, L. Wang, H. T. Zhang, X. Y. Gao, T. Liu, A. T. S. Wee, Y. P. Feng and J. Ding, Physical Review Letters **104** (13), 137201 (2010).
8. P. Zhan, W. Wang, C. Liu, Y. Hu, Z. Li, Z. Zhang, P. Zhang, B. Wang and X. Cao, Journal of Applied Physics **111** (3), 033501 (2012).
9. V. Etacheri, R. Roshan and V. Kumar, ACS Applied Materials & Interfaces **4** (5), 2717-2725 (2012).
10. J. M. D. Coey, Solid State Sciences **7** (6), 660-667 (2005).
11. S. B. Singh, Y.-F. Wang, Y.-C. Shao, H.-Y. Lai, S.-H. Hsieh, M. V. Limaye, C.-H. Chuang, H.-C. Hsueh, H. Wang, J.-W. Chiou, H.-M. Tsai, C.-W. Pao, C.-H. Chen, H.-J. Lin, J.-F. Lee, C.-T. Wu, J.-J. Wu, W.-F. Pong, T. Ohigashi, N. Kosugi, J. Wang, J. Zhou, T. Regier and T.-K. Sham, Nanoscale **6** (15), 9166-9176 (2014).

12. M. S. Alam, U. Manzoor, M. Mujahid and A. S. Bhatti, Journal of Sensors **2016** (8296936), 1-5 (2016).

13. J. Singh, M. S. L. Hudson, S. K. Pandey, R. S. Tiwari and O. N. Srivastava, International Journal of Hydrogen Energy **37** (4), 3748-3754 (2012).

14. Y. Aykut, G. N. Parsons, B. Pourdeyhimi and S. A. Khan, Langmuir **29** (12), 4159-4166 (2013).

15. J. D. Hwang, J. S. Lin and S. B. Hwang, Journal of Physics D: Applied Physics **48** (40), 405103 (2015).

16. C. Y. Liu, H. Y. Xu, L. Wang, X. H. Li and Y. C. Liu, Journal of Applied Physics **106** (7), 073518 (2009).

17. W. Liu, B. Yao, Y. Li, B. Li, C. Zheng, B. Zhang, C. Shan, Z. Zhang, J. Zhang and D. Shen, Applied Surface Science **255** (13–14), 6745-6749 (2009).

18. A. A. Lotin, O. A. Novodvorsky, E. V. Khaydukov, V. N. Glebov, V. V. Rocheva, O. D. Khramova, V. Y. Panchenko, C. Wenzel, N. Trumpaicka and K. D. Chtcherbachev, Semiconductors **44** (2), 246-250 (2010).

19. A. Ohtomo, M. Kawasaki, T. Koida, K. Masubuchi, H. Koinuma, Y. Sakurai, Y. Yoshida, T. Yasuda and Y. Segawa, Applied Physics Letters **72** (19), 2466-2468 (1998).

20. S. S. Kim and B.-T. Lee, Thin Solid Films **446** (2), 307-312 (2004).

21. P. Misra, P. Bhattacharya, K. Mallik, S. Rajagopalan, L. M. Kukreja and K. C. Rustagi, Solid State Communications **117** (11), 673-677 (2001).

22. C. Brigouleix, P. Topart, E. Bruneton, F. Sabary, G. Nouhaut and G. Campet, Electrochimica Acta **46** (13), 1931-1936 (2001).

23. D. Wang, T. Narusawa, T. Kawaharamura, M. Furuta and C. Li, Journal of Vacuum Science & Technology B **29** (5), 051205 (2011).

24. T. Prasada Rao and M. C. Santhoshkumar, Applied Surface Science **255** (8), 4579-4584 (2009).

25. E. S. Shim, H. S. Kang, J. S. Kang, J. H. Kim and S. Y. Lee, Applied Surface Science **186** (1–4), 474-476 (2002).

26. S. W. Shin, I. Y. Kim, G. V. Kishor, Y. Y. Yoo, Y. B. Kim, J. Y. Heo, G.-S. Heo, P. S. Patil, J. H. Kim and J. Y. Lee, Journal of Alloys and Compounds **585**, 608-613 (2014).

27. J. Y. Cho, S. W. Shin, Y. B. Kwon, H.-K. Lee, K. U. Sim, H. S. Kim, J.-H. Moon and J. H. Kim, Thin Solid Films **519** (13), 4282-4285 (2011).

28. W. Yang, R. D. Vispute, S. Choopun, R. P. Sharma, T. Venkatesan and H. Shen, Applied Physics Letters **78** (18), 2787-2789 (2001).

29. S. G. Bahoosh, A. T. Apostolov, I. N. Apostolova, S. Trimper and J. M. Wesselinowa, Journal of Magnetism and Magnetic Materials **373**, 40-47 (2015).

30. S. K. Mahadeva, J. Fan, A. Biswas, K. S. Sreelatha, L. Belova and K. V. Rao, Nanomaterials **3** (3), 486-497 (2013).

31. L. Cao, L. Zhu, J. Jiang, R. Zhao, Z. Ye and B. Zhao, Solar Energy Materials and Solar Cells **95** (3), 894-898 (2011).

32. Y. Liu, Y. Li and H. Zeng, J. Nanomater. **2013** (196521), 1-9 (2013).

33. K. Mukes, X. Jun, K. V. Rao, B. Lyuba, C. Elin and F. Mats, Journal of Physics: Condensed Matter **22** (34), 345004 (2010).

34. H. Chen, J. Ding and S. Ma, Physica E: Low-dimensional Systems and Nanostructures **42** (5), 1487-1491 (2010).

35. S. Gautam, A. Thakur, A. Vij, S. Jung, I. J. Lee, H. J. Shin, H. K. Lee, J. Park, J. H. Song and K. H. Chae, AIP Conference Proceedings **1536** (1), 541-542 (2013).

36. S. Han, Y. K. Shao, Y. M. Lu, P. J. Cao, W. J. Liu, Y. X. Zeng, F. Jia and D. L. Zhu, Materials Research Bulletin **64**, 76-81 (2015).

37. P. S. Shewale, N. K. Lee, S. H. Lee and Y. S. Yu, Journal of Alloys and Compounds **640** (Supplement C), 525-533 (2015).

38. C. M. Araujo, M. Kapilashrami, X. Jun, O. D. Jayakumar, S. Nagar, Y. Wu, C. Århammar, B. Johansson, L. Belova, R. Ahuja, G. A. Gehring and K. V. Rao, Applied Physics Letters **96** (23), 232505 (2010).

39. Q. J. Wang, J. B. Wang, X. L. Zhong, Q. H. Tan, Z. Hu and Y. C. Zhou, Applied Physics Letters **100** (13), 132407 (2012).

40. A. Biswas, W. Shirong, S. Nagar, L. Belova and K. V. Rao, MRS Online Proceedings Library Archive **1292**, mrsf10-1292-k1212-1245 (1296 pages) (2011).

41. J. Li, Y. Jiang, G. Bai, T. Ma, D. Yang, Y. Du and M. Yan, Applied Physics A **115** (3), 997-1001 (2014).

42. Q. Wang, Q. Sun, G. Chen, Y. Kawazoe and P. Jena, Physical Review B **77** (20) (2008).

43. D. J. Rogers, F. H. Teherani, P. Bove, A. Lusson and M. Razeghi, presented at the SPIE OPTO, 2013 (unpublished).

44. Y. Yoshino, K. Inoue, M. Takeuchi, T. Makino, Y. Katayama and T. Hata, Vacuum **59** (2–3), 403-410 (2000).

45. Y. J. Zeng, Z. X. Jian, Z. Z. Ye, G. H. Gao, Y. F. Lu, B. H. Zhao, L. P. Zhu and S. H. Hu, Superlattices and Microstructures **43** (4), 278-284 (2008).

46. P. Gopal and N. A. Spaldin, Physical Review B **74** (9) (2006).

47. C. Song, F. Zeng, K. W. Geng, X. J. Liu, F. Pan, B. He and W. S. Yan, Physical Review B **76** (4) (2007).

48. J. Elanchezhiyan, K. P. Bhuvana, N. Gopalakrishnan and T. Balasubramanian, Journal of Alloys and Compounds **463** (1–2), 84-88 (2008).

49. G. Srinivasan and J. Kumar, Crystal Research and Technology **41** (9), 893-896 (2006).

50. R. Janisch, P. Gopal and N. A. Spaldin, Journal of Physics-Condensed Matter **17** (27), R657-R689 (2005).

51. S. K. Mahadeva, Z.-Y. Quan, J. C. Fan, H. B. Albargi, G. A. Gehring, A. Riazanova, L. Belova and K. V. Rao, MRS Online Proceedings Library Archive **1494**, 115-120 (2013).

52. S. K. Mahadeva, Z.-Y. Quan, J.-C. Fan, H. B. Albargi, G. A. Gehring, A. V. Riazanova, L. M. Belova and K. V. Rao, MRS Online Proceedings Library Archive **1577**, 1-6 (2013).

53. S. K. Mahadeva, J.-C. Fan, A. Biswas, G. M. Rao, K. S. Sreelatha, L. Belova and K. V. Rao, Materials Express **3** (4), 328-334 (2013).

54. H. Nguyen Hoa, S. Joe and B. Virginie, Journal of Physics: Condensed Matter **19** (3), 036219 (2007).

55. M. Ying, H. J. Blythe, W. Dizayee, S. M. Heald, F. M. Gerriu, A. M. Fox and G. A. Gehring, Applied Physics Letters **109** (7), 072403 (2016).

56. Ü. Özgür, Y. I. Alivov, C. Liu, A. Teke, M. A. Reshchikov, S. Doğan, V. Avrutin, S.-J. Cho and H. Morkoç, Journal of Applied Physics **98** (4), 041301 (2005).

57. R. Ghosh, D. Basak and S. Fujihara, Journal of Applied Physics **96** (5), 2689-2692 (2004).

58. G. A. Kumar, M. V. R. Reddy and R. Katta Narasimha, IOP Conference Series: Materials Science and Engineering **73** (1), 012133 (2015).

59. N. H. Hong, N. Poirot and J. Sakai, Physical Review B **77** (3), 033205 (2008).

60. X. J. Liu, C. Song, F. Zeng, F. Pan, B. He and W. S. Yan, Journal of Applied Physics **103** (9), 093911 (2008).

Chapter 6

Transition Metals-Doped In_2O_3

6.1 INTRODUCTION

Since Dietl *et al.* theoretically predicted room temperature ferromagnetism in Mn doped ZnO, dilute magnetic semiconductors (DMS) have attracted a great deal of interest for their potential applications in spintronic devices [1-3]. Dilute magnetic semiconductors are ferromagnetic semiconductors formed by incorporating a small percentage of magnetic atoms into the semiconductor host lattice [2-5].

The Curie temperature of DMS materials has been reported to be at or above room temperature. Thin films of ZnO, SnO_2, TiO_2 and In_2O_3 were successfully reported to be magnetic when doped with different transition metals [2, 3]. However, the origin of RTFM in TM-doped In_2O_3 thin films is still under debate and believed to either originate from TM magnetic substituted ions, secondary magnetic phases, ferromagnetic nano-clusters or oxygen vacancies [3-5].

This chapter investigates the structural, magnetic, optical and magneto-optical properties of TM (Fe and Mn)-doped In_2O_3 thin films grown by PLD technique. The Fe-doped In_2O_3 films were grown from three targets containing either FeO, Fe_3O_4 or Fe_2O_3 precursor. The amount of oxygen in these precursors is different; it is lowest in FeO and highest in Fe_2O_3. Thus, the aim of this study was to determine the importance of the oxygen amount in each precursor and its effect on the magnetic properties in particular. For this

purpose, the Fe-doped In_2O_3 films were deposited at base pressure and two higher oxygen pressures.

It was found that Fe-doped In_2O_3 films are sensitive to TM precursor. This was clearly shown by the Fe-doped In_2O_3 films grown under base pressure where metallic Fe existed. On the other hand, the Fe-doped In_2O_3 films grown at higher oxygen pressures from different iron precursors show no trace of metallic Fe; indicating that almost all Fe ions are substitutional in the In_2O_3 site.

In_2O_3 films were found to be sensitive to the type of TM. This was confirmed through the absence of metallic Mn in the Mn-doped In_2O_3 films that were deposited at the same base pressure used in the case of Fe-doped In_2O_3 films. The Mn-doped In_2O_3 films were grown from Mn_2O_3-doped In_2O_3 target as a function of oxygen pressure; at base pressure and two higher oxygen pressures.

In this study, RTFM was observed in all TM-doped In_2O_3 samples. The Fe-doped In_2O_3 film prepared from a FeO precursor at base pressure was found to show the largest magnetisation; this is attributed to the increased amount of metallic Fe which was found to be ~ 13%. Although the magnetisation was found to be dependent on the TM precursor, the change of oxygen pressure in the PLD chamber seemed to be more important. This is because the variation of magnetisation with changing the oxygen pressure was bigger than that due to TM precursor. The saturation magnetisation values, however, showed that due to grain boundaries (GBs) the Mn-doped In_2O_3 samples were more magnetic than Fe-doped In_2O_3 films. This reveals the importance of GBs in enhancing the magnetism of TM-doped In_2O_3 thin films.

6.2 LITERATURE REVIEW of In_2O_3 and (Fe, Mn)-Doped In_2O_3

In_2O_3 in its non-stoichiometric form is an *n*-type semiconductor material transparent in the visible range with a wide band gap of 3.75 eV in the ultra-violet (UV) region of the spectrum [3, 6]. This material, however, behaves as an insulator in its stoichiometric form, while in its oxygen deficient form, it appears to have *n*-type doping levels induced by oxygen vacancies [8].

Doping the In_2O_3 with TM can enhance the magnetic properties. For example, RTFM has been observed in different TM-doped In_2O_3 which can be ascribed to the solubility of the TM in the In_2O_3 matrix. Jayakumar *et al* found that the saturation magnetisation increased proportionally with increasing Fe concentration, *x*, from 0.05 to 0.2 in $(In_{1-x}Fe_x)_2O_3$ and then decreased beyond 0.2; indicating that the maximum solubility limit of Fe ions in In_2O_3 lattice is 20% [3, 9-13].

6.2.1 Electronic Structure of In_2O_3 and TM-doped In_2O_3

In_2O_3, can exist in three structures: two body-centered cubic (bcc-) structures *I* 2_13, *Ia*3 and a rhombohedral (rh-) structure *R*3*c* [14]. In this work, only the polymorph bcc-In_2O_3 (*Ia*3) known as the cubic bixbyite structure is considered because this is the structure that was seen in our films.

Pure In_2O_3 has a unit cell with a lattice constant, α, of 10.118Å. The grain size in polycrystalline In_2O_3 films is typically between 100 and 400 Å and is affected by the substrate temperature, oxygen pressure and doping concentration [15].

Each cubic unit cell in In_2O_3 contains 80 atoms in 16 formula units [16, 17]. The [001] direction of the unit cell of In_2O_3 can be visualized as the accumulation of three different layers: an oxygen atom layer (O-layer); indium atoms from *d* site only (D-layer); and indium atoms from both *b* and *d* sites (M-layer), as in Figure 6. 1 (a) [6].

The relative positioning of the vacant sites results in two types of cation sites (In^{+3}) and one anion site (O^{-2}); the indium ions occupy 8*b* and 24*d*, while oxygen ions are located on the 48*e* in Wyckoff notation, as shown in Figure 6. 1 (b) [6, 17-20].

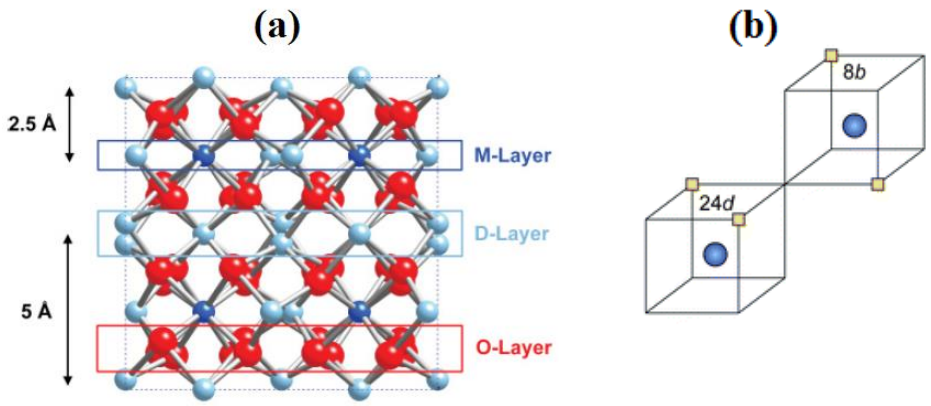

Figure 6.1: (a) The In_2O_3 unit cell of the bixbyite structure; the large red balls are the oxygen atoms, and the small blue and light blue balls represent In atoms at *d* and (*b* and *d*) sites, respectively [6]. (b) The configurations of oxygen vacancies around the two types of In sites 8*b* and 24*d* in the Wyckoff positions [20].

6.2.2 Properties of TM-doped In_2O_3

Many studies have been performed on powder, bulk and thin films of TM-doped In_2O_3. However, the obtained results are contradictory and have led to ambiguity in the interpretation of the origin of ferromagnetism in this material. Fe-doped In_2O_3 powder, for example, has been reported to be paramagnetic when sintered in air and ferromagnetic

when sintered in a vacuum. In Fe-doped In_2O_3 thin films grown by PLD techniques, defects may originate from several sources, such as oxygen vacancies, Fe dopants and interstitial In^{3+} [21-25].

As reported by Takahiro *et al.* and Kohiki *et al.* RTFM has been observed in Fe-doped In_2O_3 thin films as a result of the formation of Fe_2O_3 or Fe_3O_4 nanoclusters [13, 17, 26-28]. The presence of the Fe_3O_4 nanoparticles has been reported to enhance the RTFM; showing a considerable coercive value of ~ 400 Oe [29].

In_2O_3 and TM-doped In_2O_3 thin films can be prepared using PLD technique either under base pressure or oxygen pressure; and it is well-known that decreasing P_{O_2} during growth results in an increase of oxygen vacancies and *vice versa* [3, 23]. Oxygen vacancies are donor defects that generate free carriers (electrons) which can increase the exchange interactions between the magnetic impurities.

However, increasing the oxygen pressure has been found to cause oxidising of Fe^{2+} ions to Fe^{3+} ions [11]. Hence, at base pressure and low oxygen pressure, the change in oxygen vacancy concentration is more effective than other changes, whereas Fe^{3+} ions are dominant at higher oxygen pressures [3, 11, 24].

In terms of Mn-doped In_2O_3 thin films, it has been reported by a number of researchers that RTFM can be obtained for films prepared using PLD technique [30, 31]. The oxygen vacancies and grain boundaries were found to be responsible for the observed RTFM in Mn-doped In_2O_3 thin films [15, 30, 32, 33]

As with the magnetic properties, the optical and magneto-optical properties of TM-doped In_2O_3 have been widely reported to be sensitive to growth conditions such as TM concentration, substrate temperature and oxygen pressure [3, 5, 15, 23]. For example,

MCD signal for a Fe-doped In_2O_3 film prepared at base pressure was found to be considerable; whereas the MCD signal for the sample grown at high oxygen pressures was very small [3].

The large MCD spectrum mentioned above, was ascribed to the existence of a fraction of magnetic ions. Thus, an exchange splitting resulted in a difference in the band structure between spin-up and spin-down electrons. This in turn led to an imbalance in the density of states at the Fermi level, causing the MCD spectra.

In contrast, the small MCD signal indicated that the states near the Fermi level were localised and the density of states were independent of energy. As a result, spin splitting of these localised states did not affect the balance of the density of states at the Fermi level [3, 15].

Hence, from previous studies it can be concluded that the method of thin film fabrication and film growth conditions play an important function in determining the magnetic and optical properties of TM-doped In_2O_3 thin films [18, 34, 35].

6.3 SAMPLE PREPARATION

Three different PLD targets all with the same nominal composition of 5% Fe-doped In_2O_3 were prepared by the solid-state reaction technique in which high-purity In_2O_3 was mixed with either FeO, Fe_3O_4, or Fe_2O_3 powders. The powders were purchased from Alfa Aesar had purities of 99.999% for In_2O_3, 99.995% for FeO, 99.998% for Fe_3O_4, and 99.999% for Fe_2O_3. Thus, three targets were made; FeO-doped In_2O_3, Fe_3O_4-doped In_2O_3, and Fe_2O_3-doped In_2O_3. Nine Fe-doped In_2O_3 films were grown as a function of oxygen pressure, thus three films from each target, more details on this is given in Table 6.1.

Similarly, 5% Mn-doped In_2O_3 target were prepared from high-purity In_2O_3 (99.999%, Alfa Aesar) and Mn_2O_3 (99.999%, Alfa Aesar) powders. Three Mn-doped In_2O_3 films were deposited as a function of oxygen pressure.

All the twelve TM-doped In_2O_3 were deposited at three different oxygen pressures: a base pressure of 2×10^{-5} Torr; and two higher oxygen pressures of 2×10^{-4} and 2×10^{-3} Torr. All films were deposited at the same substrate temperature of 450 °C for a deposition time of 16 mins on double-sided polished, single-crystal *c*-cut Al_2O_3 sapphire substrates from PI-KEM Ltd. More details of the targets and films preparations can be found in **section 3.2** of **Chapter 3**. Table 6.1 gives a summary of the four TM precursors used in the TM-doped In_2O_3 targets in addition to the three different pressures in the PLD chamber, and the films thickness.

Table 6.1: Summary of the TM precursors used in the TM-doped In_2O_3 targets, and the content and growth conditions of the samples that were studied in this chapter.

Precursor	Samples		
	Content	Pressure (Torr)	Thickness (nm)
FeO	Fe-doped In_2O_3	5×10^{-5}	414
		5×10^{-4}	273
		5×10^{-3}	185
Fe_3O_4		5×10^{-5}	435
		5×10^{-4}	291
		5×10^{-3}	193
Fe_2O_3		5×10^{-5}	451
		5×10^{-4}	311
		5×10^{-3}	220
Mn_2O_3	Mn-doped In_2O_3	5×10^{-5}	443
		5×10^{-4}	315
		5×10^{-3}	203

6.4 EXPERIMENTAL RESULTS

The structural, magnetic, optical and magneto-optical properties of all the TM-doped In_2O_3 samples are shown and discussed in more detail below; Fe-doped In_2O_3 films are discussed first, followed by Mn-doped In_2O_3 films.

6.4.1 Fe-Doped In_2O_3

The structural characteristics of all Fe-doped In_2O_3 films were obtained using: XRD, XANES, and EXAFS. Some of the XRD measurements were carried out at the University of Sheffield and the others by Dr. Feng-Xian Jiang at Shanxi Normal University, Linfen, China.

The XANES and EXAFS measurements were taken by Dr. S.M. Heald at the Advanced Photon Source in the Argonne National Laboratory, USA. All the magnetic, optical and magneto-optical measurements were carried out at the University of Sheffield.

6.4.1.1 Structural Properties

The XRD for the Fe-doped In_2O_3 films grown at base and high oxygen pressures were measured using CuKα radiation (λ=1.5406 Å). The data show that the diffraction peaks indicate the well-known cubic bixbyite structure of pure In_2O_3.

The XRD patterns of all Fe-doped In_2O_3 thin films grown at base pressure are shown in Figure 6.2. The diffraction peaks at (222) and (400) indicate that Fe-doped In_2O_3 exhibit the same cubic structure of pure In_2O_3. The (322) diffraction peak is from the sapphire substrate.

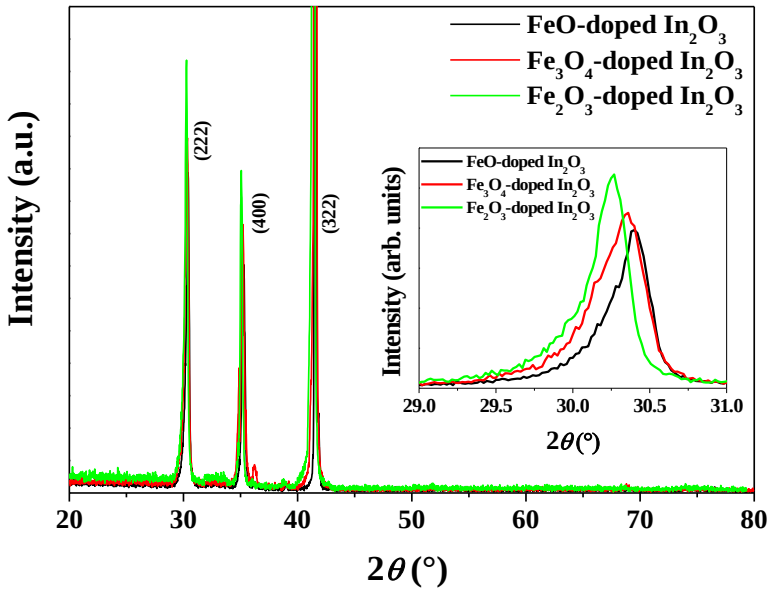

Figure 6.2: XRD data of the Fe-doped In_2O_3 thin films grown from different precursors at a base pressure of 2×10^{-5} Torr. The inset demonstrates the shifting of the (222) peak towards smaller angles with increasing O_2 content. Data taken by Dr. Feng-Xian Jiang.

There is a small peak, which is shown in red, ~ 36^{o} that indicates the presence of a secondary phase of FeO. No line of metallic Fe was detected within the detection limit of XRD [25, 31, 36].

The inset of the Figure 6.2 shows that increasing the oxygen content from the precursors results in shifting the (222) peaks towards smaller angles; implying an increase in the value of the $d_{(222)}$. The reason for such behaviour might be the reduction of the number of oxygen vacancies [3, 25].

For further investigation, *K*-edge XANES and EXAFS spectra were measured to show whether there is any existence of metallic Fe in addition to the FeO secondary phase that was detected by XRD, particularly in the Fe-doped In_2O_3 films grown at base pressure. Also these measurements were taken for the Fe-doped In_2O_3 films grown at higher oxygen pressure.

In the XANES spectra, as shown in Figures 6.3 (a) and 6.3 (b), the standard valence states of metallic Fe, Wüstite (FeO), Magnetite (Fe_3O_4) and Hematite (Fe_2O_3) are plotted alongside Fe-doped In_2O_3 films to be used as references.

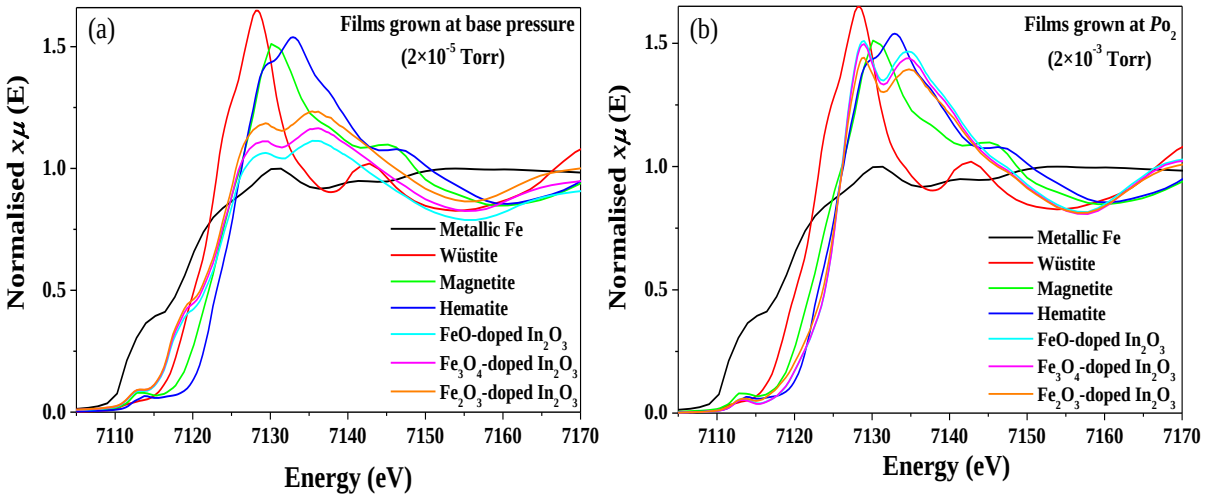

Figure 6.3: *K*-edge XANES spectra of reference compounds of metallic Fe, FeO, Fe_3O_4 and Fe_2O_3 and the Fe-doped In_2O_3 films grown from different precursors at: (a) a base pressure of 2×10^{-5} Torr; and (b) higher partial oxygen pressure of 2×10^{-3} Torr. Data taken by Dr. Steve Heald.

Figure 6.3 (a) displays the XANES data of all the Fe-doped In_2O_3 samples grown from the FeO, Fe_3O_4, and Fe_2O_3 precursors at base pressure of 2×10^{-5} Torr. All films have some features that correspond to metallic Fe that was estimated to be ~ 13%. Such results might be due to a large structural disorder caused by an increased number of oxygen vacancies originated at base pressure [37]. However, Figure 6.3 (b) shows that the XANES data of the Fe-doped In_2O_3 films deposited at a higher oxygen pressure of 2×10^{-3} Torr are located between the spectra of FeO and Fe_2O_3, indicating the substitution of the Fe ions for In^{3+} in the In_2O_3 lattice. Thus, the valence states contain a mixture of Fe^{2+} and Fe^{3+} ions [3, 15, 38].

The EXAFS spectra of the Fe-doped In_2O_3 films prepared at base pressure were compared with the spectra of hematite and Fe_2O_3-doped In_2O_3 (substitutional) sample (prepared by our former colleague Dr. Qi Feng) which is believed to be pure substitutional, as illustrated in red line in Figure 6.4 (a). The data illustrate a reduction in the intensity for $2 \le R \le 3$ Å, suggesting the presence of some Fe oxide secondary phase in addition to the metallic Fe clusters [39].

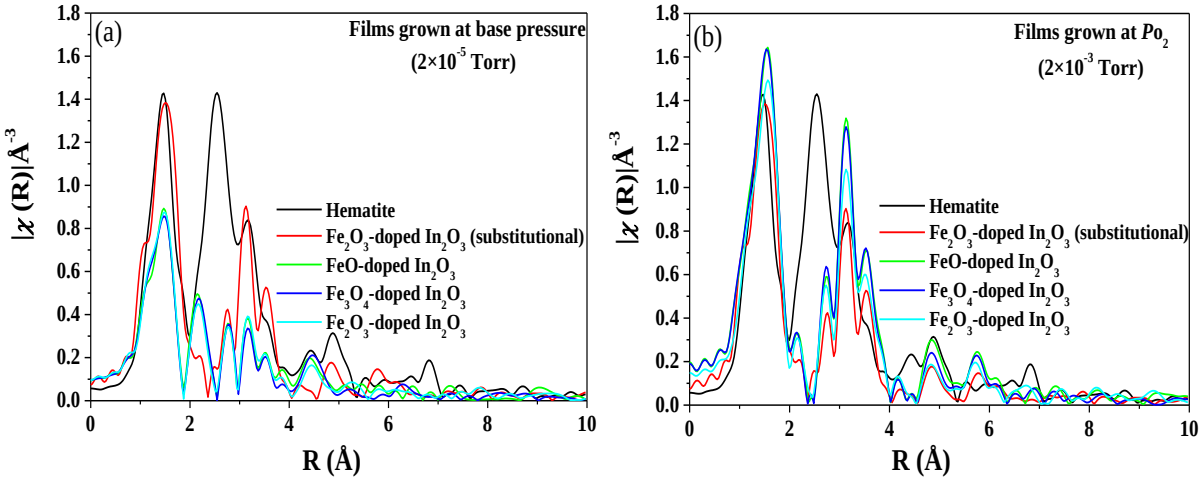

Figure 6.4: (a) EXAFS Fourier transform of Fe_2O_3 and substitutional Fe_2O_3-doped In_2O_3 deposited at base pressure as reference compounds and the Fe-doped In_2O_3 films grown from different precursors at; (a) base pressure of 2×10^{-5} Torr and (b) O_2 pressure of 2×10^{-3} Torr. Data taken by Dr. Steve Heald.

These results further support the XRD data that showed the existence of the FeO secondary phase. The present clusters might emerge from the relaxation of the oxygen environment surrounding the Fe ions which are mainly caused by the formation of oxygen vacancies [3, 39]. On the other hand, the EXAFS data of the films of Fe-doped In_2O_3 prepared at high oxygen pressure show no traces of metallic Fe and any secondary phases of Fe oxides, as in Figure 6.4 (b). This result is in agreement with the sample of $(In_{0.95}Fe_{0.05})_2O_3$ (substitutional) prepared by Dr. Feng. The EXAFS data confirm the

previous XANES data where the Fe exists in a mixture of the valence states of Fe^{2+} and Fe^{3+} ions [15, 38].

6.4.1.2 Magnetic Properties

The magnetic hysteresis loops at 5 and 300 K were taken for all Fe-doped In_2O_3 films that were deposited from different precursors at base pressure and two higher oxygen pressures. All films displayed room temperature ferromagnetism. A magnetic field of 10000 Oe was applied parallel to the plane of the film. The diamagnetic contribution from the sapphire substrate has been subtracted, as has the paramagnetic contribution that arises from the film. These two contributions were subtracted using the same method shown previously in **section (3.4.2.1)**.

Figures 6.5 (a) and 6.5 (b) respectively show the 5 and 300 K raw magnetic hysteresis loops of the Fe-doped In_2O_3 films grown from FeO, Fe_3O_4, and Fe_2O_3 precursors and deposited at a base pressure of 2×10^{-5} Torr. The 5 and 300 K raw magnetic hysteresis loops of the Fe-doped In_2O_3 films deposited at higher oxygen partial pressure of 2×10^{-3} Torr are respectively shown in Figures 6.5 (c) and 6.5 (d).

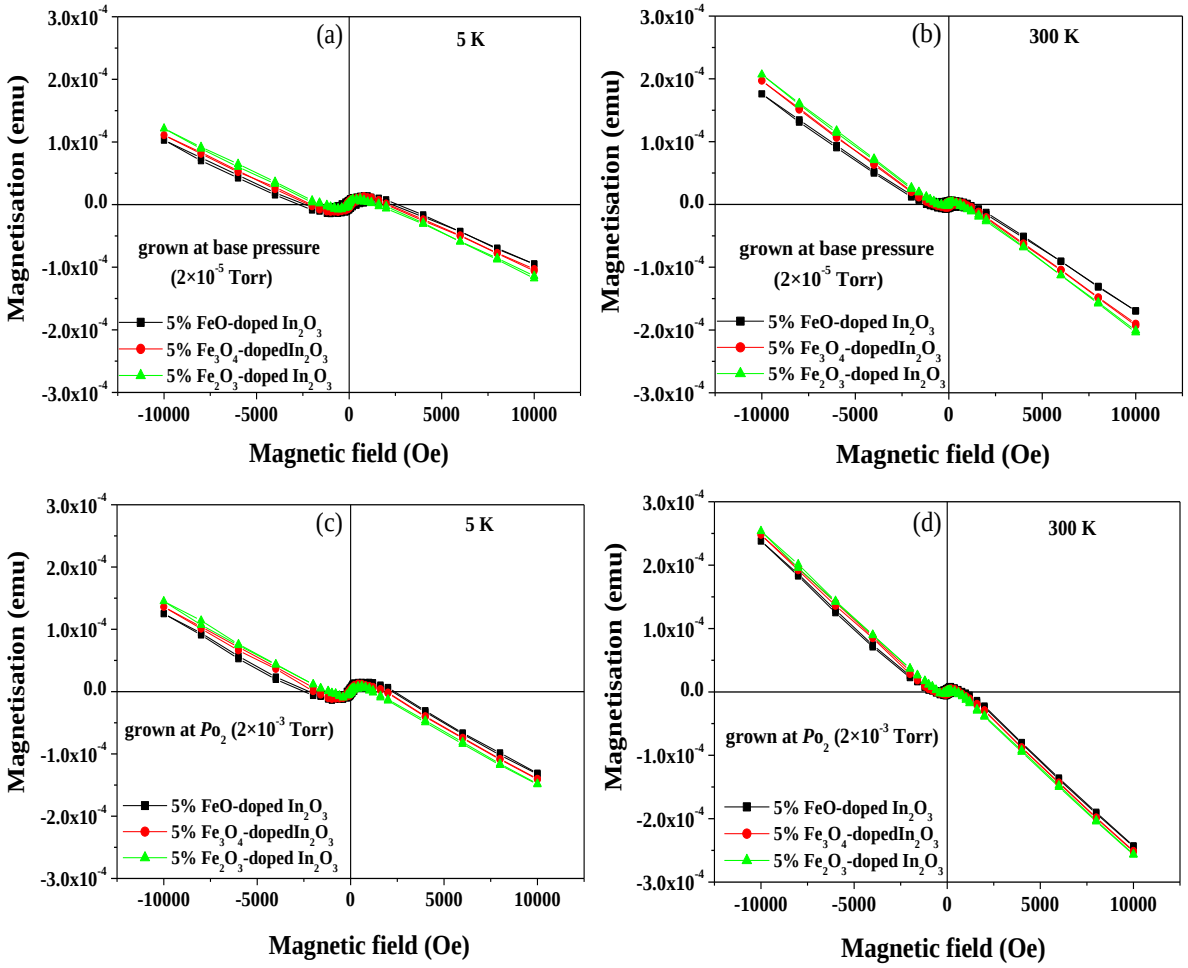

Figure 6.5: (a) and (b) are respectively the raw data of magnetic hysteresis loops measurements at 5 K and 300 K for the Fe-doped In_2O_3 films from different precursors at a base pressure of 2×10^{-5} Torr. (c) and (d) are respectively the raw data of hysteresis loops taken at 5 and 300 K for the Fe-doped In_2O_3 films from different precursors at the higher oxygen pressure of 2×10^{-3} Torr.

Since the magnetic susceptibility of sapphire substrate is temperature independent and the paramagnetic susceptibility of the film at 300 K is negligible, then the paramagnetic contribution of the film at 5 K can be estimated using the Curie-Weiss law as follows:

$$\chi(5K) - \chi(300K) = \frac{C}{5} - \frac{C}{300} \approx \frac{C}{5} \qquad (6.1)$$

where C is the Curie constant which can be calculated from the raw data of the Fe-doped In_2O_3 films measured at T = 5 K. When the Curie constant is calculated, then the expected magnetic susceptibility from the TM ions can be calculated using the expression:

$$\chi = \frac{Nxp_{eff}^2 \mu_B^2 \mu_0}{3k_B T} \tag{6.2}$$

where N is the number of In ions per unit volume, x is the concentration of Fe dopant, p_{eff} is the effective number of Bohr magneton, μ_B is the Bohr magneton, μ_0 is the magnetic permeability of free space, and k_B is Boltzmann's constant.

From the previous equations, the experimental p values of TM ions can be obtained and compared with the calculated values. The measured p values of the TM ions for the Fe-doped In_2O_3 films grown from FeO, Fe_3O_4, and Fe_2O_3 precursors, i.e. Fe^{2+} and Fe^{3+} ions, have been found to be 4.5± 0.3. Hence, these values indicate that the Fe ions in the Fe-doped In_2O_3 films are mostly Fe^{2+} since its calculated p = 4.9. This agrees quite well with the magneton number calculated using $p = 2[S(S+1)]^{1/2}$; this means that the orbital moment is fully quenched.

However, the smaller observed values of the effective magnetic moments obtained from the magnetic susceptibility clearly indicate that only a fraction of the Fe ions contribute to the observed ferromagnetism [47]. One or more of the following factors can effectively lower the value of the effective magnetic moment of an ion: the antiferromagnetic interaction that may occur between nearest neighbours; any cluster containing Fe; and the nature of the nanostructured material [42, 48, 49].

Figures 6.6 (a) and 6.6 (b) show the 5 and 300 K magnetic hysteresis loops of the Fe-doped In_2O_3 films deposited at base pressure of 2×10^{-5} Torr. Figures 6.6 (c) and 6.6 (d)

show the 5 and 300 K magnetic hysteresis loops of the Fe-doped In_2O_3 films deposited at a higher oxygen partial pressure of 2×10^{-3} Torr. The diamagnetic term has been subtracted.

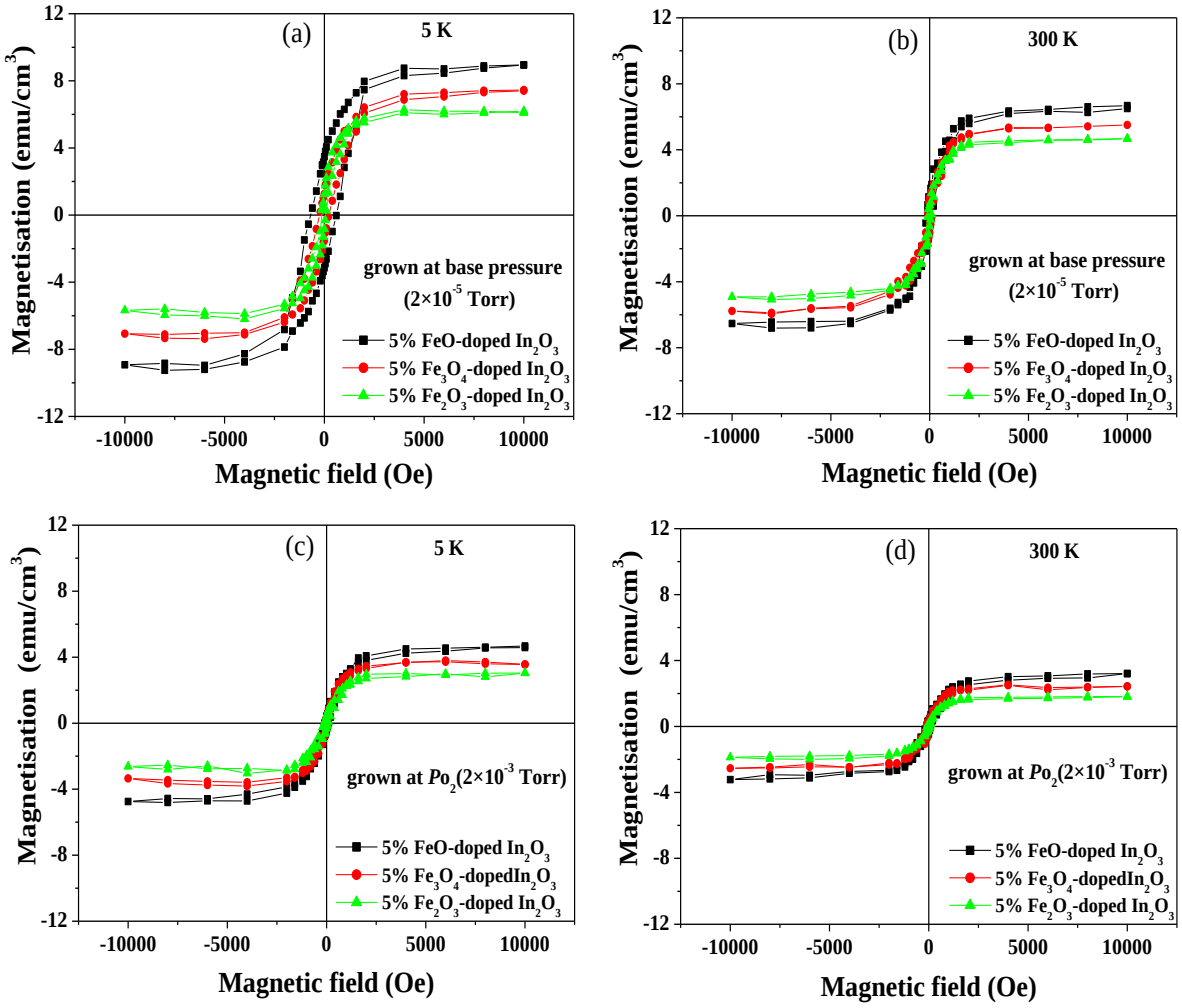

Figure 6.6: (a) and (b) are respectively the magnetic hysteresis loops measurements at 5 K and 300 K for the Fe-doped In_2O_3 films from different precursors at a base pressure of 2×10^{-5} Torr. (c) and (d) are respectively hysteresis loops taken at 5 and 300 K for the Fe-doped In_2O_3 films from different precursors at the higher oxygen pressure of 2×10^{-3} Torr. The diamagnetic term has been subtracted.

It was found that M_s and H_c are strongly temperature dependent. This observation indicates that, in addition to the ferromagnetic contribution, there might be a paramagnetic contribution [3, 31].

As seen in Figures 6.6 (a) and 6.6 (b), decreasing oxygen content from the target leads to a clear increase in the M_s value which can be ascribed to increasing oxygen vacancies that represent a crucial factor in enhancing the magnetism. In addition, the formation of Fe metallic cluster at base pressure might contribute to the observed increase in the M_s values [3, 39, 40].

In comparison, when the P_{O_2} was increased from base pressure to 2×10^{-3} Torr, the M_s values were found to decrease, this can be clearly seen from Figure 6.6 (c) compared to Figure 6.6 (a) for the measurements taken at 5 K, and Figure 6.6 (d) compared to Figure 6.6 (b) for the measurements taken at 300 K.

However, unlike the films grown at base pressure, the observed ferromagnetism of the films doped at the higher oxygen pressure cannot be due to the Fe clusters [3, 15, 25]. Instead, the origin of ferromagnetic behaviour might be attributed to the Fe ions at grain boundaries, and this strongly agrees with what has been previously reported in V-doped In_2O_3 thin film [39]. This is because increasing the oxygen content gives rise to an increase of the lattice constant, leading to incorporating more TM into the In_2O_3 host lattice. As a result, the average size of grains decreases and, therefore, increasing the number of grain boundaries [3, 39].

There is an agreement between the effect of increasing the oxygen pressure during the deposition, and increasing oxygen amount from the precursors through target preparation. However, increasing the oxygen pressure in the PLD chamber during growth process results in a considerable variation of magnetisation compared to the increase of the oxygen amount from target. This could be due to the large change in the oxygen vacancies that are rapidly decreased at high oxygen pressure and *vice versa* [3].

The coercive field values at RT range from 92 ± 10 to 135 ± 15 Oe, which may indicate the semiconducting behaviour as was observed by Jiang *et al*. and Feng *et al*. [3, 39]. The maximum value of H_c was found to be 670 ± 20 Oe for the FeO-doped In_2O_3 film prepared at the base pressure and measured at 5 K. This result indicates that the sample had an anisotropic behaviour of magnetisation along the easy in-plane direction. Such magnetic anisotropy possibly arises from the magnetostriction effect induced by the strain due to the fraction of the incorporated Fe ions into In sites [12].

Table 6.2 summarises the RT data of M_s and H_c extracted from the previous figures of 6.5 (a - d) for the Fe-doped In_2O_3 samples deposited at base pressure and oxygen partial pressure of 2×10^{-3} Torr.

Table 6.2: The variations of M_s and H_c measured at RT with changing the oxygen content through different precursors and during the deposition process of the $(In_{0.95}Fe_{0.05})O_3$ films.

Magnetic Property	**FeO-doped In_2O_3**		**Fe_3O_4-doped In_2O_3**		**Fe_2O_3-doped In_2O_3**	
	Oxygen pressure (Torr)					
	2×10^{-5}	2×10^{-3}	2×10^{-5}	2×10^{-3}	2×10^{-5}	2×10^{-3}
M_s (emu/cm^3)	6.8± 0.3	3.6± 0.3	6 ± 0.2	2.5 ± 0.2	4.2 ± 0.3	2.0 ± 0.2
H_c (Oe)	135 ± 15	118 ± 14	113 ± 14	97 ± 10	100 ± 12	92 ± 10

Temperature-dependent ZFC and FC magnetisations (M vs T) data were obtained for all Fe-doped In_2O_3 samples grown from FeO, Fe_3O_4, and Fe_2O_3 precursors and deposited at 2×10^{-5} Torr. A magnetic field of 100 Oe was applied parallel to the plane of

the samples. The diamagnetic contribution from the sapphire substrate has been subtracted from all ZFC and FC curves.

At higher temperatures, all Fe-doped In_2O_3 films showed a reversible magnetism as there is no sign of hysteresis. Decreasing the temperature, however, resulted in the FC curve of the Fe_3O_4-doped In_2O_3 and Fe_2O_3-doped In_2O_3 films to diverge from the ZFC curve at ~ 125 K, as shown in Figure 6.7 (a). On the other hand, FeO-doped In_2O_3 exhibited a large separation between FC and ZFC just around 220 K, as shown in Figure 6.7 (b). This result confirms the large coercive field of this sample shown by the hysteresis loop measured at 5 K, presented above in Figure 6.6 (a).

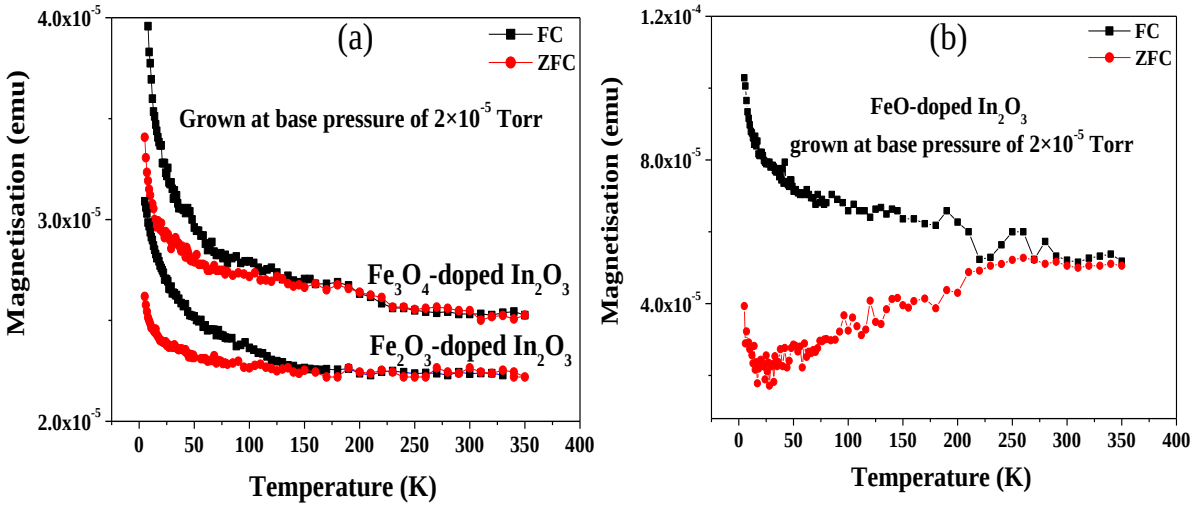

Figure 6.7: FC and ZFC magnetisation curves of the Fe-doped In_2O_3 from Fe_3O_4 and Fe_2O_3 precursors in (a) and from FeO precursor in (b) where all samples were grown at base pressure of 2×10^{-5} Torr.

The ZFC/FC magnetisations of the Fe-doped In_2O_3 films grown from Fe_3O_4 and Fe_2O_3 precursors indicate that all the sizes of magnetic clusters were too small to show blocking at RT. However, the blocking shown by the Fe-doped In_2O_3 grown from the FeO precursor was larger, indicating the existence of large Fe nanoparticles [12, 44]. This is in

agreement with the XANES and EXAFS data that showed a fraction of metallic Fe in all the Fe-doped In_2O_3 films deposited at base pressure.

Increasing the magnetisation steeply below 50 K by decreasing the temperature is a characteristic of DMS materials. Such behaviour might result from the Fe ions that are not contributing to the long-range ferromagnetic order [41, 43, 45]. Decreasing the temperature further reveals a paramagnetic contribution in addition to the observed weak ferromagnetic behaviour shown from the previous RT hysteresis loops.

From Figure 6.7 (b), the Fe nanoparticle size can be estimated from the measured blocking temperatures in the ZFC/FC curves using the Bean–Livingston formula, $KV=25k_BT_B$, where K is the anisotropy constant, V is the average volume of the particles, and k_B is Boltzmann's constant [44]. For metallic Fe particles, K is ~ 4.8×10^4 J/m. Thus, it was found that the average size of the Fe nanoparticles to be ~ 14.5 nm.

6.4.1.3 Optical Properties

The optical properties of the Fe-doped In_2O_3 films were investigated by carrying out transmission and reflection measurements at room temperature. From these measurements, absorption data were obtained to gain an insight into the electronic structure and, therefore, estimate the band gap of the Fe-doped In_2O_3 films.

Since the optical properties of this material are extremely sensitive to different target and thin film preparation parameters, the following results will show the effect of

oxygen amount, in particular. Figure 6.8 illustrates the absorption data around the band edge for all the Fe-doped In_2O_3 films grown at base and different oxygen pressures.

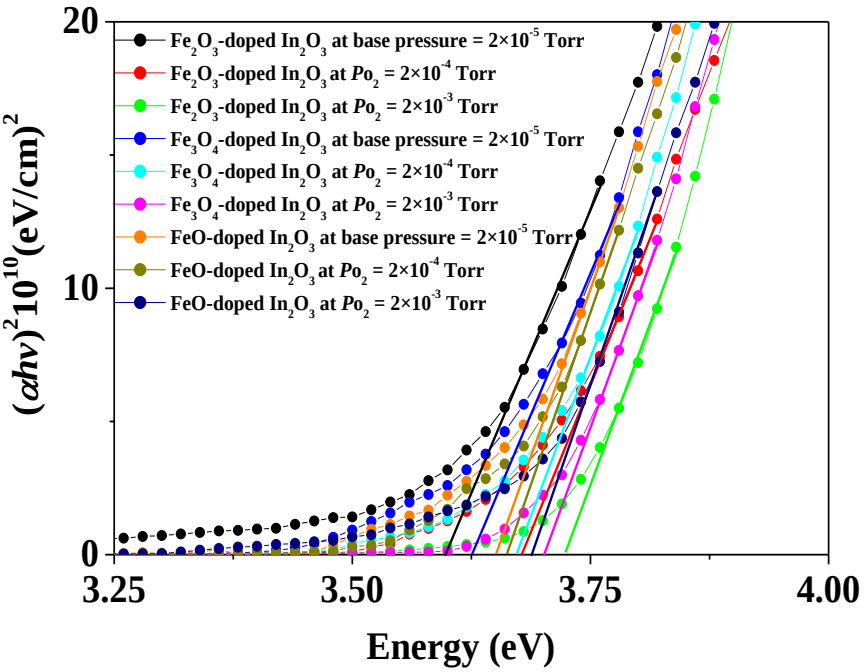

Figure 6.8: Absorption data of Fe-doped In_2O_3 samples grown from FeO, Fe_3O_4 and Fe_2O_3 precursors deposited at base pressure of 2×10^{-5} Torr and the two higher oxygen pressures of 2×10^{-4} Torr and 2×10^{-3}Torr.

It can be seen that the band gap decreases with the increasing amount of oxygen from the target for the films grown at base pressure with colours (black, blue and orange).

However, the band gap increased with the increase of the oxygen pressure during growth for the films of Fe_2O_3-doped In_2O_3 with colours (black, red and green), for the films of Fe_3O_4-doped In_2O_3 with colours (blue, cyan and pink), and for the films of FeO-doped In_2O_3 with colours (orange, dark yellow and navy). The band gap values are summarised in Table 6.3.

Table 6.3: Summary of the band gap values of Fe-doped In_2O_3 thin films deposited at base and higher oxygen pressures.

Sample	E_g **(eV)**		
	Base Pressure (2×10^{-5} Torr)	Oxygen Pressure (2×10^{-4} Torr)	Oxygen Pressure (2×10^{-3} Torr)
FeO-doped In_2O_3	3.65 ± 0.01	3.66 ± 0.01	3.69 ± 0.02
Fe_3O_4-doped In_2O_3	3.63 ± 0.02	3.67 ± 0.02	3.70 ± 0.01
Fe_2O_3-doped In_2O_3	3.60 ± 0.02	3.68 ± 0.02	3.72 ± 0.01

Two main factors might be responsible for these different observations of decreasing (increasing) the band gap with increasing (increasing) the oxygen content either from the precursors or during the growth: the first is due to the Burstein-Moss effect; and the other is because of the change in the size of the unit cell [25, 50].

According to the Burstein-Moss effect, increasing charge carriers plays an important role in shifting the band gap to higher energy. Thus, the samples deposited at base pressure showed an increase in the value of the band gap with decreasing oxygen content from the precursors. This can be ascribed to increasing the charge carriers as a result of an increase in oxygen vacancies [3, 51].

In contrast, increasing the value of the band gap with increasing oxygen pressure during the deposition process may be attributed to oxidising the large Fe^{2+} ions to smaller Fe^{3+} ions; such a reduction in the ionic radius gives rise to a contraction in the lattice resulting in an increase in the band gap [3, 25, 33, 40, 50].

6.4.1.4 Magneto-Optical Properties

The MCD spectra for all Fe-doped In_2O_3 samples were measured in the energy range between 1.7 and 4 eV at RT in Faraday geometry by applying a magnetic field of 18000 Oe, as displayed in Figures 6.9 (a) and 6.9 (b). The diamagnetic signal from the sapphire substrate has been subtracted.

MCD spectra magnitude decreased as the oxygen content increased. These results are consistent with the values of the magnetisation saturation obtained from the magnetic hysteresis loops measured by the SQUID.

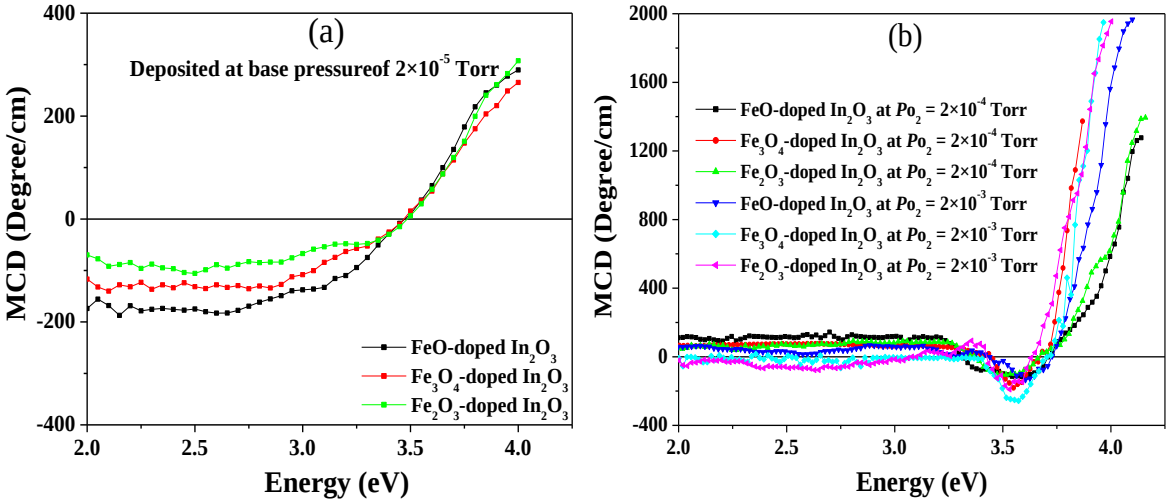

Figure 6.9: MCD spectral shapes of the Fe-doped In_2O_3 samples deposited from different precursors at: (a) base pressure and (b) two higher oxygen pressures, respectively.

For the samples deposited at base pressure, there is a considerable negative MCD in the energy range from 2 to just below 3.5 eV; above that a positive spectral shape can be seen, as in Figure 6.9 (a). This result indicates that the negative features were due to the presence of metallic Fe nanoparticles. Such a finding shows that metals contribute very strongly to the MCD. This is consistent with what has been reported by Jiang *et al*. [40].

In Figure 6.9 (b), most of the samples grown at higher oxygen pressure showed weak positive MCD spectral shapes in the region below 3.5 eV, perhaps due to weak spin-orbit coupling arising from the electrons at the grain boundaries [39]. The negative features below 3.5 eV are characteristic of the films grown at base pressure; arising from spin split conduction band [3, 52].

Above 3.5 eV, there are clear peaks which are characteristic of the band structure of the In_2O_3 as a host material. This could be due to defect states near the energy gap of In_2O_3 (~ 3.75 eV), as a result of the spin polarised 3*d* electrons at around this energy.

Adding more oxygen to the films might then prevent the formation of any metallic clusters, consequently allowing Fe ions to be more easily substituted for the In ions in the In_2O_3 matrix. As a result, there is an exchange interaction between the *d* orbital magnetic moments of the dopant, and the charge carriers of the *s* and *p* orbitals of the host material [3, 25, 28, 53].

6.4.2 Mn-Doped In_2O_3

Three Mn-doped In_2O_3 thin films were grown from Mn_2O_3 precursor and deposited as a function of oxygen pressure. The aim of this study was to investigate the doping of In_2O_3 with a TM other than Fe to avoid the formation of metallic clusters for films grown at base pressure. Hence, the three Mn-doped In_2O_3 films were deposited under the same conditions as the Fe-doped In_2O_3.

The results of the Mn doped In_2O_3 thin films were compared with Fe-doped In_2O_3 films; the Mn-doped In_2O_3 films were not found to have any traces of secondary phases. This finding was confirmed using different measurements as presented below.

6.4.2.1 Structural Properties

As depicted in Figure 6.10, the obtained XRD data reveal that all the films showed high crystallinity, as well as the bixbyite cubic structure found for pure In_2O_3. The results also show that the dominant peaks were (222) and (400), suggesting that the films were well oriented along the *c*-axis and ruling out the possibility of forming any secondary phases or impurities at the limit of the XRD.

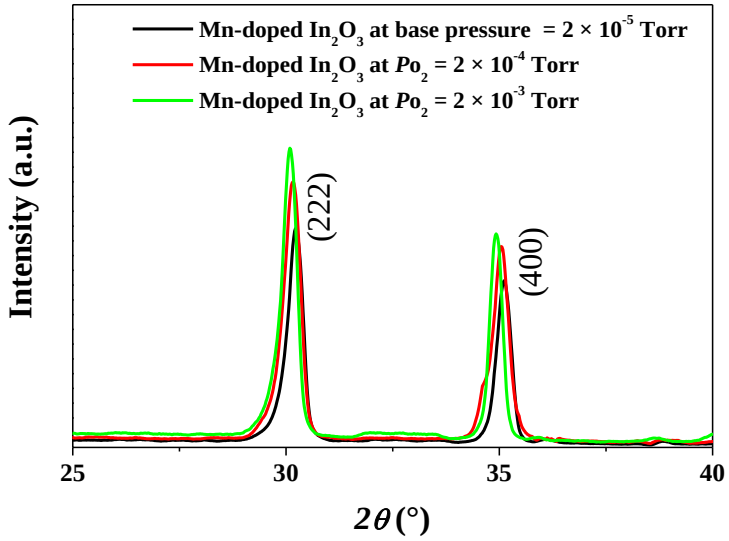

Figure 6.10: XRD data from Mn-doped In_2O_3 films grown at different oxygen pressures.

The value of 2θ was found to shift towards smaller angles as the oxygen pressure increased, indicating increasing incorporation of Mn ions into the In_2O_3 lattice [15, 31, 55]. This is because incorporating TM into the In_2O_3 lattice, in general, results in a reduction in the ionic radii.

The *K*-edge XANES spectra measurements for all films were taken to further investigate the potential formation of metallic Mn and any oxide secondary phases. Figure 6.11 (a) shows the XANES spectra of different manganese oxides, as references, and the Mn doped In_2O_3 films.

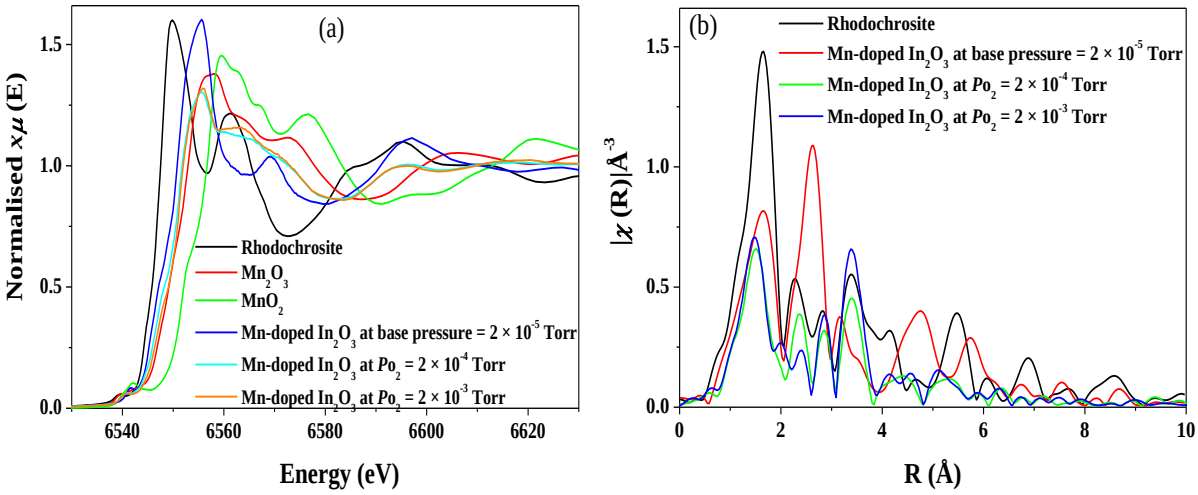

Figure 6.11: (a) *K*-edge XANES spectra of $(In_{0.95}Mn_{0.05})_2O_3$ grown at different oxygen pressures with some manganese oxide references, and (b) Fourier transform EXAFS data from the same samples with the reference of Rhodochrosite. Data taken by Dr. Steve Heald.

The XANES spectra indicate that there was no metallic Mn but there might have been a small percentage of Mn oxides in the case of the film deposited at base pressure. Clearly, the absorption edge for all films was located between Rhodochrosite ($MnCO_3$) and Mn_2O_3, suggesting that the sample deposited at base pressure probably had many Mn^{2+} ions, whereas the films deposited at higher oxygen pressures seemed to have a mixture of Mn^{2+} and Mn^{3+} ions.

Figure 6.11 (b) shows the Fourier transforms of the EXAFS spectra to investigate more the structural environment around the Mn atoms. It can be noticed that the sample

deposited at base pressure shifted to larger R as expected for the 2+ valence; this confirms the previous *K*-edge XANES result.

The intensities of all samples were observed to be larger in some areas compared to the pure substitutional model, indicating a possible minority of oxide impurity phases. Thus, the data were found to be better fitted with the Rhodochrosite model [15, 56, 57].

6.4.2.2 Magnetic Properties

The M-H hysteresis loops for all samples were measured at 5 and 300 K in a magnetic field of 10000 Oe applied parallel to the plane of the Mn-doped In_2O_3 films, as shown in Figures 6.12 (a) and 6.12 (b). The substrate diamagnetic effect has been subtracted.

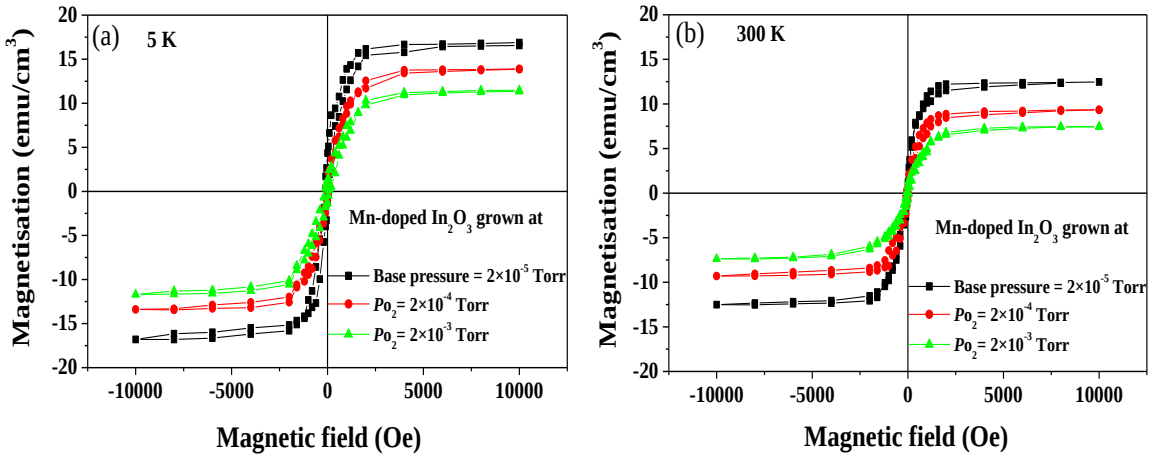

Figure 6.12: (a) and (b) M-H hysteresis loops of Mn-doped In_2O_3 thin films grown at different oxygen pressures measured at low and room temperatures, respectively. The diamagnetic contribution from the substrate has been subtracted.

Pronounced hysteresis loops are noticeable for all samples at both temperatures, indicating ferromagnetic behaviour at room temperature. The dependence of the saturation

magnetisation on the temperature suggests the existence of a paramagnetic contribution added to the ferromagnetic component.

M_s was found to decrease with increasing oxygen pressure owing to the reduction of oxygen vacancies. Nonetheless, increasing the oxygen pressure causes the oxidation of the Mn^{2+} ions to Mn^{3+} ions, which are less magnetic, and this might explain the decrease in the saturation magnetisation [25, 58]. The values of M_s and H_c for all Mn-doped In_2O_3 samples are summarised in Table 6.4.

Table 6.4: A summary of the M_s and H_c data from Mn-doped In_2O_3 thin films at different oxygen pressures.

P_{O_2} (Torr)	M_s (emu cm^{-3})		H_c (Oe)		$\frac{Ms(5)}{Ms(300)}$	$\frac{Hc(5)}{Hc(300)}$
	5 K	300 K	5 K	300 K		
2×10^{-5}	16.4 ± 0.2	12.5 ± 0.3	150 ± 18	110 ± 14	1.31 ± 0.05	1.69 ± 0.04
2×10^{-4}	14.3 ± 0.2	10.2 ± 0.1	130 ± 16	97 ± 12	1.40 ± 0.07	1.36 ± 0.06
2×10^{-3}	11.3 ± 0.1	7.3 ± 0.3	100 ± 14	89 ± 12	1.54 ± 0.03	1.24 ± 0.08

The coercive field values were found to decrease with increasing oxygen pressure, excluding an extrinsic origin such as Mn clusters or MnO impurity, in forming the ferromagnetism. The values of $M_s(5)/M_s(300)$ and $H_c(5)/H_c(300)$ reveal that the magnetisation was strongly influenced by changing the oxygen content; this is in agreement with what has been reported for semiconducting oxide films [15, 25].

6.4.2.3 Optical and Magneto-Optical Properties

The optical absorption and MCD data at RT for all samples are presented in Figures 6.13 (a) and 6.13 (b), respectively. The absorption of the film grown at base pressure was large at low energies compared to other films grown at higher oxygen pressures, indicating a poorer quality for the base pressure-grown film and showing a smaller band gap of 3.68 ± 0.02 eV than the widely reported value of 3.75 eV.

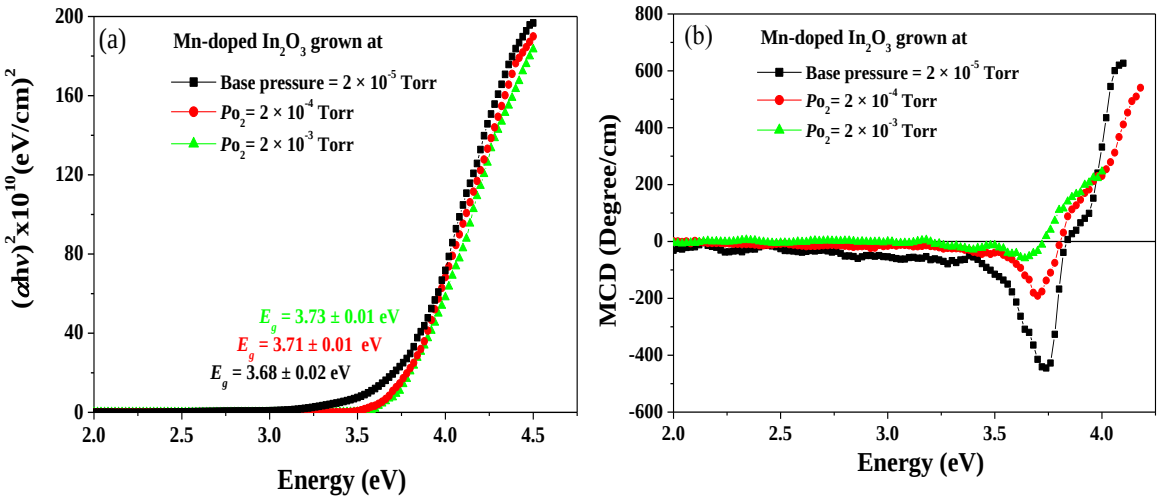

Figure 6.13: (a) and (b) Absorption and MCD spectra of $(In_{0.95}Mn_{0.05})_2O_3$ samples grown at different oxygen pressures, respectively.

Increasing the oxygen pressure for the other films, however, results in the band gap shifting to higher energy. This could be ascribed to the crystallinity and surface quality that improve with increasing oxygen pressure [15, 54].

The MCD measurements were taken for all samples in a magnetic field of 18000 Oe and the diamagnetic effect of the sapphire substrate has been subtracted. Figure 6.13 (b) shows clear MCD signals from all films that emerge from about 2.5 eV and continue to be more pronounced at the band edge of about 3.75 eV.

The MCD spectral shapes near 2.5 eV might be attributed to the transitions to the donor states either caused by oxygen vacancies or oxidising Mn^{2+} to Mn^{3+} ions for films deposited at base and higher oxygen pressures, respectively [21, 28].

The MCD features around 3.75 eV are ascribed to the carriers at the band edge of In_2O_3. The MCD values differ according to oxygen content in each sample as they decrease with increasing the oxygen pressure. Hence, the MCD spectrum of the film deposited at base pressure displays the highest MCD value, mainly attributed to the oxygen vacancies [21, 53].

6.5 SUMMARY AND CONCLUSIONS

Oxygen content was found to influence different properties of (Fe, Mn)-doped In_2O_3 thin films. For Fe-doped In_2O_3, the oxygen content can either be varied from the precursor or during the deposition process and give more or less the same results. This contradicts the results that have been recently found for ZnCoO where different precursors, grown under different oxygen pressures, gave different magnetic properties [52]. Such a finding reveals the importance of target preparation in controlling and studying various properties of TM-doped In_2O_3 films as a function of oxygen content. The structural, magnetic, optical and magneto-optical properties were systematically investigated and found to be oxygen pressure dependent.

The results of the XRD measurements of 5% Fe-doped In_2O_3 thin films prepared at base pressure from FeO, Fe_3O_4 and Fe_2O_3 precursors revealed the existence of a FeO secondary phase. This was also confirmed by EXAFS data which, in addition, showed the

presence of FeO as well as metallic Fe for the Fe-doped In_2O_3 samples grown at base pressure. This observation might be ascribed to the loss of oxygen, as the reduction of oxygen pressure during the growth has been found to result in the formation of Fe metallic clusters [40] as well as the creation of more oxygen vacancies [3, 15].

The magnetic data show that all samples had RT ferromagnetism. Films grown at lower oxygen pressure were more magnetic, perhaps as a result of the effect of oxygen vacancies in addition to Fe metallic clusters. Such a result is in agreement with the results found from the XRD and EXAFS measurements. Further support was provided by ZFC/FC measurements revealing stronger ferromagnetism for films prepared at base pressure compared to films made at higher oxygen pressure, more specifically, the FeO-doped In_2O_3 film showing the effect of large nanoparticles.

The optical data are consistent with other data as the band edge was found to increase by reducing the oxygen from the target when films were grown at base pressure. This was found to be due to the increase in charge carriers resulting from the increase in the oxygen vacancies. However, when films were deposited under oxygen flow, the band gap was observed to increase with increasing oxygen pressure and *vice versa* as a result of lattice contraction due to oxidising Fe^{2+} to Fe^{3+} ions.

In the case of the films at base pressure, the observed MCD signals are mainly ascribed to the presence of the metallic Fe. On the other hand, the MCD signals of the films doped at higher pressure are believed to be due to the weak interaction between spin-orbit states of the electrons at the grain boundaries.

In terms of the Mn-doped In_2O_3, all samples were found to display ferromagnetism at RT where the magnetisation is strongly affected by varying the oxygen

content. The substitution of the Mn ions for In ions in the In_2O_3 lattice is most likely obtained by Mn^{3+} ions according to the EXAFS data.

The magneto-optical results support the magnetic data where the MCD signals decrease when the oxygen pressure increases. In addition, positive features of the MCD spectra, shown in the energy range of 2.5 to 3.7 eV, provide evidence to confirm the formation of donor states that lie within the Fermi level and close to the conduction band. Such states were found to originate via the oxygen vacancies and Mn^{3+} ions for the films grown at lower and higher O_2 pressure, respectively.

It can be concluded that the TM-doped In_2O_3 thin films are extremely sensitive to growth conditions. For instance, the oxygen pressure/content plays an important role in determining the concentration of oxygen vacancies. In addition, studying the TM-doped In_2O_3 as a function of oxygen pressure has revealed that the formation of metallic TM depends on the type of transition metal. Hence, iron was found to produce metallic Fe when prepared at base pressure, whereas manganese was not.

6.6 REFERENCES

1. T. Dietl, H. Ohno, F. Matsukura, J. Cibert and D. Ferrand, Science **287** (5455), 1019-1022 (2000).
2. A. M. H. R. Hakimi, F. Schoofs, R. Bali, N. A. Stelmashenko, M. G. Blamire, S. Langridge, S. A. Cavill, G. van der Laan and S. S. Dhesi, Physical Review B **82** (14), 144429 (2010).
3. F.-X. Jiang, X.-H. Xu, J. Zhang, X.-C. Fan, H.-S. Wu, M. Alshammari, Q. Feng, H. J. Blythe, D. S. Score, K. Addison, M. Al-Qahtani and G. A. Gehring, Journal of Applied Physics **109** (5), 053907 (2011).
4. O. M. Berengue, C. A. Amorim, H. Kamimura, A. J. Chiquito and E. R. Leite, Journal of Applied Physics **111** (1), 013713 (2012).
5. S. Kaleemulla, A. S. Reddy, S. Uthanna and P. S. Reddy, Journal of Alloys and Compounds **479** (1–2), 589-593 (2009).
6. D. R. Hagleitner, M. Menhart, P. Jacobson, S. Blomberg, K. Schulte, E. Lundgren, M. Kubicek, J. Fleig, F. Kubel, C. Puls, A. Limbeck, H. Hutter, L. A. Boatner, M. Schmid and U. Diebold, Physical Review B **85** (11), 115441 (2012).
7. S. Kaleemulla, A. S. Readdy, S. Uthanna and P. S. Reddy, Optoelectronics and Advanced Materials, Rapid Communications **2** (12), 782-787 (2008).
8. P. D. C. King, T. D. Veal, D. J. Payne, A. Bourlange, R. G. Egdell and C. F. McConville, Physical Review Letters **101** (11), 116808 (2008).
9. H. R. Fallah, M. Ghasemi, A. Hassanzadeh and H. Steki, Materials Research Bulletin **42** (3), 487-496 (2007).

10. H. W. Ho, B. C. Zhao, B. Xia, S. L. Huang, J. G. Tao, A. C. H. Huan and L. Wang, Journal of Physics-Condensed Matter **20** (47) 475204 (2008).

11. F. X. Jiang, X. H. Xu, J. Zhang, H. S. Wu and G. A. Gehring, Applied Surface Science **255** (6), 3655-3658 (2009).

12. H. Kim, M. Osofsky, M. M. Miller, S. B. Qadri, R. C. Y. Auyeung and A. Piqué, Applied Physics Letters **100** (3), 032404 (2012).

13. J. He, S. Xu, Y. K. Yoo, Q. Xue, H.-C. Lee, S. Cheng, X.-D. Xiang, G. F. Dionne and I. Takeuchi, Applied Physics Letters **86** (5), 052503 (2005).

14. A. Walsh, J. L. F. Da Silva, S. H. Wei, C. Korber, A. Klein, L. F. J. Piper, A. DeMasi, K. E. Smith, G. Panaccione, P. Torelli, D. J. Payne, A. Bourlange and R. G. Egdell, Physical Review Letters **100** (16) (2008).

15. Q. Feng, H. J. Blythe, F.-X. Jiang, X.-H. Xu, S. M. Heald, A. M. Fox and G. A. Gehring, APL Mater. **1** (2), 022107 (2013).

16. C. Fahed, S. B. Qadri, H. Kim, A. Piqué, M. Miller, N. A. Mahadik, M. V. Rao and M. Osofsky, physica status solidi (c) **7** (9), 2298-2301 (2010).

17. S. Kohiki, M. Sasaki, Y. Murakawa, K. Hori, K. Okada, H. Shimooka, T. Tajiri, H. Deguchi, S. Matsushima, M. Oku, T. Shishido, M. Arai, M. Mitome and Y. Bando, Thin Solid Films **505** (1–2), 122-125 (2006).

18. S. J. Hu, S. S. Yan, X. L. Lin, X. X. Yao, Y. X. Chen, G. L. Liu and L. M. Mei, Applied Physics Letters **91** (26) 262514 (2007).

19. O. Warschkow, D. E. Ellis, G. B. Gonzalez and T. O. Mason, Journal of the American Ceramic Society **86** (10), 1700-1706 (2003).

20. A. Walsh and C. R. A. Catlow, Journal of Materials Chemistry **20** (46), 10438-10444 (2010).

21. L.-M. Tang, L.-L. Wang, D. Wang, J.-Z. Liu and K.-Q. Chen, Journal of Applied Physics **107** (8), 083704 (2010).

22. A. Klein, Applied Physics Letters **77** (13), 2009-2011 (2000).

23. C. Körber, V. Krishnakumar, A. Klein, G. Panaccione, P. Torelli, A. Walsh, J. L. F. Da Silva, S. H. Wei, R. G. Egdell and D. J. Payne, Physical Review B **81** (16), 165207 (2010).

24. M. S. Alshammary, *Optical and Magneto-Optical Properties of Doped Oxides*. PhD thesis, University of Sheffield, 2011.

25. X.-H. Xu, F.-X. Jiang, J. Zhang, X.-C. Fan, H.-S. Wu and G. A. Gehring, Applied Physics Letters **94** (21), 212510 (2009).

26. Y. K. Yoo, Q. Xue, H.-C. Lee, S. Cheng, X.-D. Xiang, G. F. Dionne, S. Xu, J. He, Y. S. Chu, S. D. Preite, S. E. Lofland and I. Takeuchi, Applied Physics Letters **86** (4), 042506 (2005).

27. O. Takahiro, K. Toshio, T. Hidekazu, K. Tomoji, O. Masaoki, O. Koichi and K. Shigemi, Japanese Journal of Applied Physics **45** (9L), L957 (2006).

28. A. M. H. R. Hakimi, M. G. Blamire, S. M. Heald, M. S. Alshammari, M. S. Alqahtani, D. S. Score, H. J. Blythe, A. M. Fox and G. A. Gehring, Physical Review B **84** (8), 085201 (2011).

29. M. S. Alshammari, M. S. Alqahtani, H. B. Albargi, S. A. Alfihed, Y. A. Alshetwi, A. A. Alghihab, A. M. Alsamrah, N. M. Alshammari, M. A. Aldosari, A. Alyamani, A. M. H. R. Hakimi, S. M. Heald, H. J. Blythe, M. G. Blamire, A. M. Fox and G. A. Gehring, Physical Review B **90** (14), 144433 (2014).

30. Y. An, S. Wang, L. Duan, J. Liu and Z. Wu, Applied Physics Letters **102** (21), 212411 (2013).

31. F.-X. Jiang, X.-H. Xu, J. Zhang, X.-C. Fan, H.-S. Wu and G. A. Gehring, Applied Physics Letters **96** (5), 052503 (2010).

32. G. Peleckis, X. L. Wang and S. X. Dou, Journal of Magnetism and Magnetic Materials **301** (2), 308-311 (2006).

33. S. Wang, Y. An, L. Duan, H. Liu, J. Liu and Z. Wu, Journal of Vacuum Science & Technology A **31** (6), 061515 (2013).

34. B. David and G. Emmanuel, Journal of Physics: Condensed Matter **19** (23), 236224 (2007).

35. D. Beena, K. J. Lethy, R. Vinodkumar, V. P. M. Pillai, V. Ganesan, D. M. Phase and S. K. Sudheer, Applied Surface Science **255** (20), 8334-8342 (2009).

36. Y.-P. Sun, X.-q. Li, J. Cao, W.-x. Zhang and H. P. Wang, Advances in Colloid and Interface Science **120** (1), 47-56 (2006).

37. A. Chen, K. Zhu, H. Zhong, Q. Shao and G. Ge, Solar Energy Materials and Solar Cells **120**, 157-162 (2014).

38. Y. An, S. Wang, D. Feng, Z. Wu and J. Liu, Applied Physics A **115** (3), 823-828 (2014).

39. Q. Feng, H. J. Blythe, A. M. Fox, Q. Xiu-Fang, X. Xiao-Hong, S. M. Heald and G. A. Gehring, EPL (Europhysics Letters) **103** (6), 67007 (2013).

40. F.-X. Jiang, Q. Feng, Z.-Y. Quan, R.-R. Ma, S. M. Heald, G. A. Gehring and X.-H. Xu, Materials Research Bulletin **48** (9), 3178-3182 (2013).

41. O. D. Jayakumar, I. K. Gopalakrishnan, S. K. Kulshreshtha, A. Gupta, K. V. Rao, D. V. Louzguine-Luzgin, A. Inoue, P.-A. Glans, J.-H. Guo, K. Samanta, M. K. Singh and R. S. Katiyar, Applied Physics Letters **91** (5), 052504 (2007).

42. D. Karmakar, S. K. Mandal, R. M. Kadam, P. L. Paulose, A. K. Rajarajan, T. K. Nath, A. K. Das, I. Dasgupta and G. P. Das, Physical Review B **75** (14), 144404 (2007).

43. A. Singhal, S. N. Achary, J. Manjanna, O. D. Jayakumar, R. M. Kadam and A. K. Tyagi, The Journal of Physical Chemistry C **113** (9), 3600-3606 (2009).

44. Z. Quan, W. Liu, X. Li, X. Xu, K. Addison, D. S. Score and G. A. Gehring, Materials Letters **65** (19–20), 2982-2984 (2011).

45. F.-X. Jiang, S.-B. Xi, R.-R. Ma, X.-F. Qin, X.-C. Fan, M.-G. Zhang, J.-Q. Zhou and X.-H. Xu, Chinese Physics Letters **30** (4), 047501 (2013).

46. B. Tandon, G. S. Shanker and A. Nag, The Journal of Physical Chemistry Letters **5** (13), 2306-2311 (2014).

47. V. K. Sharma, M. Najim, A. K. Srivastava and G. D. Varma, Journal of Magnetism and Magnetic Materials **324** (5), 683-689 (2012).

48. G. Peleckis, X. L. Wang and S. X. Dou, Applied Physics Letters **88** (13), 132507 (2006).

49. S. Yin, M. X. Xu, L. Yang, J. F. Liu, H. Rosner, H. Hahn, H. Gleiter, D. Schild, S. Doyle, T. Liu, T. D. Hu, E. Takayama-Muromachi and J. Z. Jiang, Physical Review B **73** (22) (2006).

50. T. Zhou, L. Wei, Y. Xie, Q. Li, G. Hu, Y. Chen, S. Yan, G. Liu, L. Mei and J. Jiao, Nanoscale Research Letters **7** (1), 1-7 (2012).

51. J. Stankiewicz, F. Villuendas and J. Bartolomé, Physical Review B **75** (23), 235308 (2007).

52. M. Ying, H. J. Blythe, W. Dizayee, S. M. Heald, F. M. Gerriu, A. Mark Fox and G. A. Gehring, Applied Physics Letters **109** (7), 072403 (2016).

53. H. Weng, J. Dong, T. Fukumura, M. Kawasaki and Y. Kawazoe, Physical Review B **73** (12), 121201 (2006).

54. M. J. Ying, W. Dizayee, Z. X. Mei, X. L. Du, A. M. Fox and G. A. Gehring, Journal of Physics D-Applied Physics **48** (25) (2015).

55. A. C. Mofor, F. Reuss, A. El-Shaer, R. Kling, E. Schlenker, A. Bakin, H. Ahlers, U. Siegner, S. Sievers, M. Albrecht, W. Schoch, W. Limmer, J. Eisenmenger, T. Mueller, A. Huebel, G. Denninger, P. Ziemann and A. Waag, Applied Physics A **88** (1), 161-166 (2007).

56. Y. K. An, Y. Ren, D. Y. Yang, Z. H. Wu and J. W. Liu, Journal of Physical Chemistry C **119** (8), 4414-4421 (2015).

57. H. Steve, S. A. Marzook, S. Alfehaid, M. Alotaibi, F. Qi and A. M. H. R. Hakimi, Journal of Physics: Conference Series **430** (1), 012081 (2013).

58. J. M. D. Coey, A. P. Douvalis, C. B. Fitzgerald and M. Venkatesan, Applied Physics Letters **84** (8), 1332-1334 (2004).

Chapter 7

Conclusion and Future Work

This chapter provides conclusions and summarises the important outcomes obtained from studying various properties of different magnetic materials. These will be presented in the first part of this chapter. The second part shows a brief plan for extending the work that has been done so far on TM-doped In_2O_3.

7.1 Conclusions from the Work Undertaken

The work described in this thesis relates to three different oxide materials: multiferroic GMO; d^0 ZnMgO; and TM-doped In_2O_3. The investigations into the magnetic properties of these materials have revealed that such properties are affected by different parameters. The strain of the thin films, for example, has been found to be the common and effective factor influencing GMO and ZnMgO magnetism. The TM-doped In_2O_3 thin films, however, have also been found to be oxygen pressure dependent.

GMO thin films grown on LSAT (100) and (111) substrates showed different magnetic properties. This is attributed to different strains introduced by different substrate orientations. The strain induced by the substrate has been found to be larger when GMO films are grown on LSAT (100) substrate, compared to LSAT (111) and STO (100) substrates [1]. As a result, the Mn-Mn exchange interactions are affected, causing an enhancement of the canting of the Mn magnetic moments. The magnetic anisotropy was found to be enhanced more along the easy plane of the *b* axis due to the compressive strain

caused by the LSAT (100) substrate. In addition, such substrate gives rise to an increased transition temperature to 30 K compared to 23 K for bulk GMO [2-4].

For GMO grown on LSAT (111) substrate, there is a suppression of the canted phase which can be induced by a magnetic field of 2500 Oe. The Curie constant has also been found to be smaller for the films grown on LSAT (111) substrate, compared to GMO on LSAT (100) substrate and nanoparticles GMO [2, 5].

LSAT (100) and (111) substrates were found to be better than STO (100) substrate. This is because these types of substrates make it possible to measure the optical properties in the energy range greater than 3.25 eV, in contrast to STO (100) substrate.

The MCD measurements reveal that, due to the compressive strain of the in-plane direction for GMO grown on LSAT (100) substrate, a considerable feature of the MCD spectrum is shown ~ 2 eV; this is attributed to the Mn-Mn inter-site transitions. On the other hand, the MCD of the GMO grown on LSAT (111) substrate is suppressed; this result is consistent with the magnetic data obtained using the SQUID magnetometer. The MCD results also illustrate another feature ~ 3 eV; this is attributed to the transition of charge-transfer between O (2*p*) and Mn (3*d*) states.

In GMO thin films, the strain can be induced via external pressure [2, 4, 5]. Thus, different degrees of distortions can be introduced to the GMO thin films when grown epitaxially on different substrates. For this purpose, LSAT (100) substrate was found to be better than LSAT (111) and STO (100) substrates. This can be clearly seen through the enhancement that LSAT (100) substrate made to the magnetic properties of the GMO thin films.

The optical and magnetic properties of **ZnMgO** thin films have been shown to be sensitive to different growth conditions, such as deposition time (film thickness), oxygen pressure, substrate type and deposition method [6, 7, 11, 13].

It was found that the band gap was mostly affected by changing the oxygen pressure. This might be attributed to the incorporation of Mg content as well as changing lattice constant. Increasing the oxygen pressure has been found to reduce the Mg content and increase the lattice constant. A as a result, the band gap has been found to be larger at low oxygen pressure and *vice versa* [6].

However, no measurable effect on the value of the band gap was observed due to the variation of film thickness, although the band gap was found to increase weakly with increasing film thickness. This could be attributed to the high strain that exists in thin films. In other words, the strain generated in thin films is higher compared to that in thick films, leading to an expansion of the lattice constant and, therefore, a decreased band gap [8-10].

The band gap values for ZnMgO films grown on glass, quartz and sapphire substrates were found to show the same trend. However, the band gap values for the ZnMgO films grown on sapphire substrates were larger compared to the films grown on glass and quartz substrates. This may be due to the compressive strain produced by sapphire substrate which in turns leads to an increase in the value of the band gap of ZnMgO films [12].

The deposition technique was also found to influence the band gap values of ZnMgO films; this is likely attributed to the Mg content. According to the EDS analyses, the ZnMgO films grown by PLD had a greater Mg content than the films deposited by sputtering. This interprets the observed higher band gap values of the PLD films compared to the sputtered films.

The magnetic properties of ZnMgO films were found to depend strongly on thickness. For instance, RT ferromagnetic behaviour was displayed for films of small thicknesses where the strain and defects play a significant role. This indicates that defects are mostly located on the film surface and/or at the interface between the film and the substrate [7]. Increasing film thickness, however, results in a transition from ferromagnetism to paramagnetism, eventually reaching diamagnetism. Similar observations were reported by Prof. Rao's group in different oxide thin films [11-14].

In comparison, magnetisation has been found to be weakly dependent on oxygen pressure. This is because increasing oxygen pressure results in a rapid reduction of the number of defects that give rise to magnetisation. However, oxygen pressure is inversely proportional to film thickness, i.e. increasing oxygen pressure results in a reduction in film thickness and *vice versa*. Consequently, increasing oxygen pressure (decreasing thickness) was found to decrease (increase) magnetisation. This represents an interesting finding which agrees with the view discussed above that magnetisation changes as a function of film thickness [7, 14].

The growth of ZnMgO films on different substrates of glass, quartz and sapphire, was found to affect the magnetisation. The ZnMgO films grown on sapphire substrates exhibited the highest magnetisation and band gap compared to the films grown on glass and quartz substrates. This may be caused by the strain and defects induced by different substrates [13].

In addition, ZnMgO films deposited by PLD technique showed higher magnetisation in comparison to the ZnMgO films grown by sputtering techniques. This could be ascribed to the types of defects produced by the two methods. Thus, it is believed

that more oxygen vacancies exist in the PLD films in comparison to the sputtered films. This is because oxygen vacancies are the most important type of defect enhancing magnetisation [7].

TM-doped In_2O_3 were widely studied using different techniques and the results showed that changing oxygen pressure can affect different properties.

Fe-doped In_2O_3 films were deposited from three different targets prepared from three different precursors: FeO, Fe_3O_4 and Fe_2O_3. Increasing the amounts of oxygen from the targets was found to result in a reduction in magnetisation. Similarly, Fe-doped In_2O_3 films deposited under different oxygen pressures showed a decrease in magnetisation with increasing oxygen pressure, and *vice versa*. This contrasts with what has been previously found in ZnCoO films in which different precursors tended to give different magnetic properties. This may depend on the type of defects; the ZnCoO films grown from Co precursor were found to have Zn vacancies which are believed to be responsible for RT magnetisation [15].

The Fe-doped In_2O_3 films deposited under base pressure showed some traces of defect phases such as FeO and metallic Fe clusters; these were detected using XRD and EXAFS measurements. These defects were found to be a crucial issue compared to the films in which all the TM ions were substituted for In ions. Such defects are believed to be due to the loss of oxygen during growth [16]. As a result, more Fe metallic clusters are formed, in addition to the formation of more oxygen vacancies. These two factors are probably responsible for the observed ferromagnetism of the Fe-doped In_2O_3 thin films.

The Fe-doped In_2O_3 films deposited under oxygen pressure were found to be substitutional and, therefore, different properties were observed. In these films, the grain boundaries (GBs) have been found to play an important role in determining different properties [17].

The optical data showed that, for Fe-doped In_2O_3 films deposited at base pressure the band gap increased when reducing the amount of oxygen from the target. This is ascribed to the Burstein-Moss effect. However, for the films grown under oxygen pressure, the band gap increased proportionally with increasing the oxygen pressure; this is a result of oxidising the Fe^{2+} ions to Fe^{3+} ions, resulting in a contraction of the lattice.

The magnetic and MCD data are in agreement for both sets of films. The observed magnetisation of Fe-doped In_2O_3 films deposited at base pressure is ascribed to the presence of Fe metallic clusters and secondary phase of FeO; these were confirmed by XRD and EXAFS measurements. The magnetisation of Fe-doped In_2O_3 films grown at high oxygen pressures is due to the weak interaction between spin-orbit states of the electrons at the grain boundaries.

Mn-doped In_2O_3 samples were grown under different oxygen pressures to see whether the formation of metallic clusters, such as those in the case of Fe-doped In_2O_3 films, can be avoided. Mn-doped In_2O_3 thin films were successfully grown and different measurements revealed no forms of metallic clusters. All the magnetic, optical and MCD data show that Mn-doped In_2O_3 films are highly oxygen dependent [18, 19].

In conclusion, TM-doped In_2O_3 thin films are extremely sensitive to growth conditions. The manifestation of ferromagnetism is dependent on the existence of clusters as well as the oxygen pressure.

7.2 Future Work

Based on the work on TM-doped In_2O_3 thin films carried out at the University of Sheffield, it has been observed that the structural, optical, magnetic and magneto-optical properties of 5% TM-doped In_2O_3 thin films deposited by PLD technique are very sensitive to growth conditions, such as the type of TM and oxygen pressure. The literature reports that the properties of TM-doped In_2O_3 thin films are influenced by several other growth conditions: substrate temperature, annealing temperature, powder grinding, grain size, the energy of the laser beam and the gas used for the laser in PLD as well as the deposition method [15-21].

It would be interesting to investigate the effect of a number of the previous growth parameters on TM-doped In_2O_3 thin films. The deposition of TM- In_2O_3 thin films at different substrate temperature has been found to improve both the optical and magnetic properties. Thus, it would be worthwhile to use the TM (Fe and Mn)- In_2O_3 targets to prepare thin films at different substrate temperatures of 300, 350, 400, 450, 500, 550 and 600 °C. In addition, study of the annealing temperature's effect on TM (Fe and Mn)- In_2O_3 thin films is required to determine the importance of this parameter on the oxygen vacancies and its role in enhancing the ferromagnetism of TM- In_2O_3 films [21].

Growth of different TM (V, Cr, Co and Ni)-doped In_2O_3 films is also needed to further investigate the magnetic sensitivity to different transition metals in TM-doped In_2O_3 [17, 18].

Both PLD and sputtering techniques for thin film growth are also suggested to explore the similarities and differences among the properties of TM-doped In_2O_3 thin films grown with different deposition methods [22].

The magnetism of TM-doped In_2O_3 thin films has been suggested to originate from grains and grain boundaries. Thus, the structural properties of TM-doped In_2O_3 thin films should be investigated to provide an insight into their influence on the optical and magnetic properties. In this regard, several techniques could be used including, XRD, SEM, and AFM to determine grain size, roughness and surface morphology [22, 23]. The grain size of TM-doped In_2O_3 has been found to increase with substrate temperature [18, 22].

Optical and magnetic measurements are also needed; these can be made using a Jasco V-570 spectrophotometer and SQUID magnetometer, respectively.

The above suggested projects aim to achieve a better understanding of the origin of ferromagnetism in diluted magnetic semiconductors (DMS). It should also be remembered that great care needs to be taken when preparing TM-doped In_2O_3 targets and thin films to obtain reproducible and high quality films.

7.3 REFERENCES

1. M. S. Alqahtani, M. S. Alshammari, H. J. Blythe, A. M. Fox, G. A. Gehring, N. Andreev, V. Chichkov and M. Ya, Journal of Physics: Conference Series **391** (1), 012083 (2012).
2. J. Baier, D. Meier, K. Berggold, J. Hemberger, A. Balbashov, J. A. Mydosh and T. Lorenz, Physical Review B **73** (10), 100402 (2006).
3. T. Kimura, G. Lawes, T. Goto, Y. Tokura and A. P. Ramirez, Physical Review B **71** (22), 224425 (2005).
4. K. Noda, S. Nakamura, J. Nagayama and H. Kuwahara, Journal of Applied Physics**. 97,** (10), 103 (2005).
5. M. S. Al Qahtani, M. S. Alshammari, H. J. Blythe, A. M. Fox, G. A. Gehring, N. Andreev, V. Chichkov and Y. Mukovskii, International Conference on Strongly Correlated Electron Systems (Sces 2011) **391**, 012083 (2012).
6. S. K. Mahadeva, Z.-Y. Quan, J. C. Fan, H. B. Albargi, G. A. Gehring, A. Riazanova, L. Belova and K. V. Rao, MRS Online Proceedings Library Archive **1494**, 115-120 (2013).
7. H. Nguyen Hoa, S. Joe and B. Virginie, Journal of Physics: Condensed Matter **19** (3), 036219 (2007).
8. A. Ohtomo, M. Kawasaki, T. Koida, K. Masubuchi, H. Koinuma, Y. Sakurai, Y. Yoshida, T. Yasuda and Y. Segawa, Applied Physics Letters **72** (19), 2466-2468 (1998).

9. T. Prasada Rao and M. C. Santhoshkumar, Applied Surface Science **255** (8), 4579-4584 (2009).

10. W. Yang, R. D. Vispute, S. Choopun, R. P. Sharma, T. Venkatesan and H. Shen, Applied Physics Letters **78** (18), 2787-2789 (2001).

11. C. M. Araujo, M. Kapilashrami, X. Jun, O. D. Jayakumar, S. Nagar, Y. Wu, C. Århammar, B. Johansson, L. Belova, R. Ahuja, G. A. Gehring and K. V. Rao, Applied Physics Letters **96** (23), 232505 (2010).

12. A. Biswas, W. Shirong, S. Nagar, L. Belova and K. V. Rao, MRS Online Proceedings Library Archive **1292**, mrsf10-1292-k1212-1245 (1296 pages) (2011).

13. M. Kapilashrami, J. Xu, V. Ström, K. V. Rao and L. Belova, Applied Physics Letters **95** (3), 033104 (2009).

14. S. K. Mahadeva, J. Fan, A. Biswas, K. S. Sreelatha, L. Belova and K. V. Rao, Nanomaterials **3** (3), 486-497 (2013).

15. M. Ying, H. J. Blythe, W. Dizayee, S. M. Heald, F. M. Gerriu, A. Mark Fox and G. A. Gehring, Applied Physics Letters **109** (7), 072403 (2016).

16. F.-X. Jiang, Q. Feng, Z.-Y. Quan, R.-R. Ma, S. M. Heald, G. A. Gehring and X.-H. Xu, Materials Research Bulletin **48** (9), 3178-3182 (2013).

17. Q. Feng, H. J. Blythe, F.-X. Jiang, X.-H. Xu, S. M. Heald, A. M. Fox and G. A. Gehring, APL Materials. **1** (2), 022107 (2013).

18. Q. Feng, H. J. Harry, A. M. Fox, Q. Xiu-Fang, X. Xiao-Hong, M. H. Steve and G. A. Gillian, Europhysics Letters **103** (6), 67007 (2013).

19. F.-X. Jiang, X.-H. Xu, J. Zhang, X.-C. Fan, H.-S. Wu, M. Alshammari, Q. Feng, H. J. Blythe, D. S. Score, K. Addison, M. Al-Qahtani and G. A. Gehring, Journal of Applied Physics **109** (5), 053907 (2011).

20. M. S. Alshammari, M. S. Alqahtani, H. B. Albargi, S.A. Alfihed, Y.A. Alshetwi, A. A. Alghihab, A. M. Alsamrah, N. M. Alshammari, M. A. Aldosari, A. Alyamani, A. M. R. Hakimi, S. M. Heald, H. J. Blythe, M. G. Blamire, A. M. Fox, G. A. Gehring. Physical Review **B 90** 144433 (2014).

21. X.-H. Xu, F.-X. Jiang, J. Zhang, X.-C. Fan, H.-S. Wu and G. A. Gehring, Applied Physics Letters **94** (21), 212510 (2009).

22. R. Kumar, G. Kumar, O. Al-Dossary, and A. Umar, Materials Express **5** (1), 3-23 (2015).

23. M. S. Alqahtani, N. M. A. Hadia and S. H. Mohamed, Optik - International Journal for Light and Electron Optics **145** (Supplement C), 377-386 (2017).

“This is not the end. It is not even the beginning of the end. But it is, perhaps, the end of the beginning.”

– Winston Churchill –